JOENSUUN YLIOPISTO
UNIVERSITY OF JOENSUU
Department of Computer Science

Alexandra Oborina

OFDM and MIMO Modelling in a System Simulator with Advanced Link to System Interface

Supervisors:

Martti Moisio
MSc (physics)
martti.moisio@nokia.com
Nokia Research Center, Helsinki

Simo Juvaste
Senior Lecturer, PhD
simo.juvaste@cs.joensuu.fi
University of Joensuu

Helsinki, October 2005

University of Joensuu	Abstract of the Master's Thesis
Author	**Subject of the Thesis**
Alexandra Oborina	OFDM and MIMO Modelling in a System Simulator with Advanced Link to System Interface
Department	**Pages** 111
Computer Science	**Date** October, 2005
Supervisors	
Martti Moisio	Simo Juvaste

Wideband 4G wireless system is one of potential new wireless access technologies that will have to support data rates up to approximately 100 Mbit/s for mobile access and up to approximately 1 Gbit/s for nomadic/local wireless access according to the International Telecommunications Union–Radio vision. Support of high data rate requires 4G wireless to operate through wide bandwidth and multiple antenna systems. Therefore, the most promising techniques such as MIMO and OFDM should be applied to 4G to meet the requirements.

The thesis gives an overview of fundamentals of cellular radio system and radio channel. A special emphasis is put on new techniques such as OFDM and MIMO that can increase diversity and/or improve capacity on wideband channels.

4G system level performance of OFDM and MIMO technologies is evaluated through link and system level simulators which interacts with each other by means of link–to–system level (L2S) interface. L2S interface is a critical component needed for an accurate performance estimation. The thesis introduces two advanced L2S interface approaches called the Exponential Effective SINR Mapping (EESM) and the Mutual Information Effective SINR Mapping (MI–ESM) and compares them with existing L2S interface approach called the Actual Value Interface (AVI). The thesis also proposes initial Effective SINR Mapping for MIMO system and suggests improvement of the AVI approach.

The thesis analyzes these L2S interface approaches from information measure point–of–view and through simulation results. The thesis demonstrates essential differences between various L2S interfaces in accuracies of performance estimation effecting to the final data throughput, delay of data packets and CPU time.

Keywords:
System simulator, Link simulator, L2S interface, OFDM, SISO, MIMO, effective SINR mapping, EESM, MI–ESM

Contents

List of Figures

List of Tables

Abbreviations

AM	Amplitude Modulation, 7
AVI	Actual Value Interface, 63
AWGN	Additive White Gaussian Noise, 26
BER	Bit Error Rate, 34
BICM	Bit Interleaved Coded Modulation, 54
BS	Base Station, 4
BSS	Base Station Subsystem, 9
CDF	Cumulative Density Function, 101
CDMA	Code Division Multiple Access, 8
DFT	Discrete Fourier Transform, 21
DFT	Inverse Discrete Fourier Transform, 21
EESM	Exponential Effective SNR Mapping, 52
ESM	Effective SNR Mapping, 50
FDD	Frequency Division Duplex, 8
FDMA	Frequency Division Multiple Access, 8
FER	Frame Error Rate, 49
FFT	Fast Fourier Transform, 43
FH	Frequency Hopping, 17
FM	Frequency Modulation, 7
FT	Fourier Transform, 19
GSM	Global System for Mobile communications, 9
IFT	Inverse Fourier Transform, 20
IM	Interference Management, 17
ITU-R	International Telecommunications Union-Radio, 1
L2S	Link to System, 49
LA	Link Adaptation, 17
LOS	Line of Sight component, 16

LUT Look Up Table, 50

MCS Modulation Coding Scheme, 52
MI–ESM Mutual Information Effective SNR Mapping, 54
MIMO multiple–input–multiple–output, 33
MS Mobile Station, 4
MSE Mean Square Error, 69

NLOS Non Line of Sight component, 37

OFDM Orthogonal Frequency Division Multiplexing, 43

PC Power Control, 17
PDF Probability Density Function, 14
PER Packet Error Rate, 49
PM Phase Modulation, 7
PSD Power Spectral Density, 23

QoS Quality of Service, 17

RRM Radio Resource Management, 17

SINR Signal to Interferer and Noise Ratio, 49
SISO single–input–single–output, 38
SLS System Level Simulator, 58

TDD Time Division Duplex, 8
TDMA Time Division Multiple Access, 8
TU Typical Urban, 30

WSS Wide Sense Stationary, 22

Preface

This master thesis has been done in the NWT laboratory of Nokia Research Center.

First of all, I would like to send my appreciation to my supervisor in Nokia Research Center Mr. Martti Moisio, who has brought valuable input, fruitful discussion and encouragement to the work covered in this thesis. His guidance in an open and friendly atmosphere has been done from the beginning of my writing. I would like to express my gratitude to Mr. Jussi Ojala and Mr. Antti Sorri for their competent advices, assistence and really necessarily comments. Also I wish to thanks Mr. Antti Sevon for his advices in programming. I need to thanks Mr. Samuli Visuri for providing me with link level results.

I would like also to thanks Dr. Simo Juvaste and Prof. Jussi Parkkinen who have given me the possibility to work in NRC and who have reviewed the thesis and have provided me with valuable comments.

This work would not have been possible without the support of my family, specially my husband Yaroslav, and my friends.

Chapter 1

Introduction

Nowadays the wireless communication field is growing rapidly. The need for data rate, multimedia support and other wireless services is increasing day by day. A large number of researches around the world are going to develop potential new wireless access technologies that will support high enough data rate and will provide high enough performance with a lower cost. According to the International Telecommunications Union–Radio (ITU-R) vision for future development of mobile and wireless communications new radio access systems will have to offer a considerably improved performance. The new radio access interfaces will have to support data rates up to approximately 100 Mbit/s for mobile access and up to approximately 1 Gbit/s for nomadic/local wireless access (ITU-Radio, 2003). A large EU research project named WINNER is working towards adaptation of communication systems to growing user needs. Its major target is the development and the implementation of new radio access system called in this thesis "4G wireless" that will meet requirements suggested by the ITU-R vision.

4G wireless is expected to produce a more reliable communication link in the presence of multipath fading and interference, higher efficiency, higher throughput and, hence, wider bandwidth. Therefore, the most promising techniques such as Multiple-Input-Multiple-Output (MIMO) system and Orthogonal Frequency Division Multiplexing (OFDM) modulation technique (that can be compounded with MIMO system) should be applied to 4G.

The analysis of the changes in 4G system performance with varying system parameters such as traffic, channel model and coding scheme is dramatically complex. For the sake of simplicity 4G cellular system performance is studied with link and system level simulators. The objective of the system level simulator is to explore the behavior of the whole network. On the system level all relevant radio resource management operations carried out by the network are simulated. The simulated area is covered by predefined number of cells where each cell is served by a base station (BS). Moving mobile stations (MS) are uniformly spread in the network. Small- and large–scale variations in received signal strength and interference of the transmission between base station and mobile station caused by the mobility are taken into account. Link level simulator is commonly used to analyze only physical layer performance. On the link level a continuous transmission between BS and MS involving different specific characteristics, such as coding modulation scheme,

spatial pre- and post-processing, parameter estimation and small–scale fading, is simulated. One objective of the link level simulator is to produce results for the system simulator related to a certain signal quality level.

Currently, the link and the system level simulators interact with each other by means of link–to–system interface. The link level simulator produces a set of mapping tables for estimating the link quality in terms of bit error rate. At each step the system level simulator computes the channel quality measures for all resource elements and maps these values onto a certain bit error rate using mapping tables. Further, after receiving all bits of a packet, the mapping from bit error rate to packet error rate is realized.

Since MIMO and OFDM techniques are applied to 4G system simulator the number of resource elements to measure a channel quality is quite large, and multidimensional mapping onto packet error rate is difficult. Therefore, the objective of link–to–system interface is in accurate compression into small number of quality value parameters. Such compression can be done from instantaneous channel state – that is instantaneous quality measures of all resource elements – to one or two scalar values that are later used for mapping. In 4G system level simulator channel quality is measured by means of signal to interferer and noise ratio (SINR). In this thesis advanced link–to–system interface approach called the Effective SINR Mapping (ESM) is presented and analyzed. The ESM maps an instantaneous channel state carried out by set of SINRs across OFDM channel onto an instantaneous scalar value, an effective signal to noise ratio. In this thesis two variants of the ESM approach are illustrated, and our model of the ESM approach for MIMO system is proposed. Comparison of the advanced link–to–system mapping functions with the actual value interface (AVI) mapping function is performed from information measure point–of–view and using 4G system simulations. One possible improvement of the AVI approach is suggested. The essential differences between various ESM approaches, the AVI approach and its improved version are presented. Accuracy of performance estimation, efficiency and CPU time as quality of service measures are examined.

This thesis is organized as follows. Chapter 2 provides a brief review of the cellular radio system basics, essential principles of radio propagation and description of basic algorithms in radio resource management. For analyzing 4G system performance the knowledge of radio channel behavior is necessary. In chapter 3 we give the statistical description of radio channel model and present some channel model examples. Since MIMO system is applied to 4G wireless communication to offer more capacity and reliability of communication link, we need to study it carefully. In chapter 4 we present the fundamentals of MIMO system, describe the MIMO channel model and analyze the theoretical upper limit of the data rate by means of MIMO channel capacity. In chapter 5 OFDM modulation technique that can be combined with MIMO system is introduced. Chapter 6 presents basic principles of the ESM approach, provides two different forms of effective mapping functions and gives the description of possible ESM function realization in MIMO case. In chapter 7 general configuration of 4G system simulator is specified, and implementation of 4G system performance is described. Also, in this chapter the key issue for accurate estimation of system performance – modeling of radio propagation – is

demonstrated. The simulations running with 4G SLS and obtained results are illuminated and discussed in chapter 8 where key figures related to the evaluation of the ESM approach and the AVI approach are illustrated. Finally, chapter 9 concludes the thesis.

Chapter 2

Fundamentals of Cellular Radio System

In this chapter we briefly introduce the basic principles of cellular system, its structure and its functionality. The knowledge of these fundamentals is required passim in the thesis.

2.1 Basic Concepts of Radio Channel

Transmitting a radio signal over the air needs at least three components: transmitter, radio channel and receiver (Figure 2.1). In communication systems both mobile station (MS) and base station (BS) can act both as transmitter and as receiver.

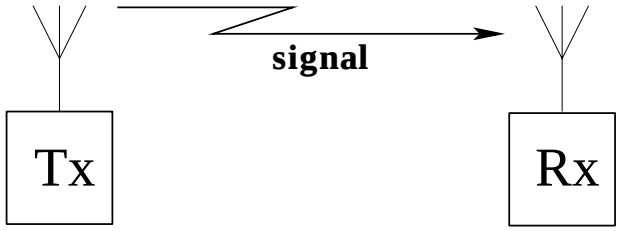

Figure 2.1: Transmission over channel.

Transmission happens in the following way. Firstly, transmitter generates a pure sinusoidal carrier signal. Then the carrier is modulated for carrying the information and is transmitted over the channel. At the receiver all modifications of the received signal are detected and demodulated.

2.1.1 Basic Characteristics of Radio Signal

The core element of the radio communication is radio (carrier) signal as it carries the information.

Physically, radio signal is a form of electromagnetic energy propagating at the speed of light (Calhoun, 1988). Radio signal has three main characteristics that can be changed over time, and, therefore, can be used to carry information:

1. *Amplitude.* The magnitude or height of the wave crests and troughs.

2. *Phase.* The angle of inflection of the wave at one moment in time.

3. *Frequency.* The number of cycles (crest-to-crest event) occurred in one second.

In mobile radio systems the transmitted signals and the channels are typically *narrowband bandpass signals and channels* or bandpass signals and channels. Signal is called *narrowband signal* if its bandwidth (band of frequencies occupied by the signal) is small relative to the carrier frequency. Signal is called *bandpass signal* if it occupies non–zero carrier frequency.

In this section we introduce three representations of the real-valued bandpass signal, each of them fully describes the signal. According to mathematical point of view bandpass signal is described by main characteristics as follows (Ziemer and Tranter, 2002, p. 19)

$$s(t) = a(t)\cos(2\pi f_c t + \phi(t)). \tag{2.1.1}$$

Here, $s(t)$ is a bandpass signal, $a(t)$ is an amplitude envelope, f_c is a carrier frequency, $\phi(t)$ is a phase. In Figure 2.2 bandpass signal $s(t)$ with amplitude $a(t) = a$ and carrier frequency f_c with zero phase are represented.

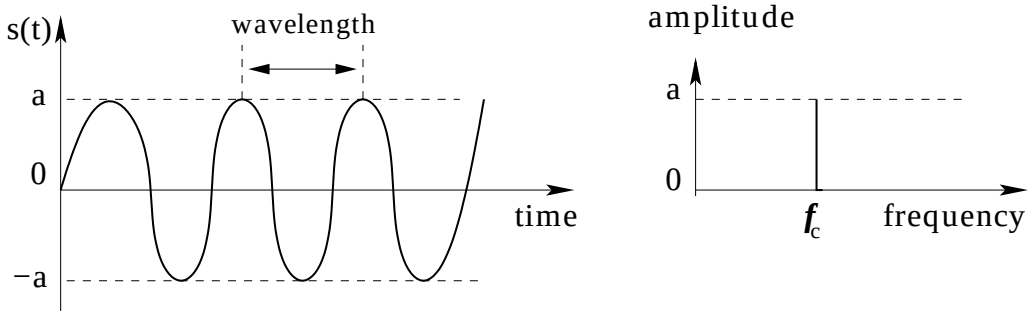

Figure 2.2: Radio wave.

Amplitude and phase are often viewed with the *polar diagram*, where signal is described relative to the carrier. In the polar form signal is represented as a phase and a magnitude. Usually bandpass signal is observed in a rectangular forms "I" (In-Phase electronic form) and "Q" (Quadrature magnetic form). In Figure 2.3 polar diagram and its rectangular "I – Q" representation are visualized.

Using trigonometry bandpass signal $s(t)$ given by (2.1.1) can be transformed to In-Phase – Quadrature form (Ziemer and Tranter, 2002, p. 81)

$$\begin{aligned} s(t) = {} & s_I(t)\cos 2\pi f_c t - s_Q(t)\sin 2\pi f_c t \\ & s_I(t) = a(t)\cos\phi(t), \quad s_Q(t) = a(t)\sin\phi(t) \end{aligned}$$

where $s_I(t)$ is In-Phase component and $s_Q(t)$ is Quadrature component of a bandpass signal $s(t)$. Since the band of frequencies of $s_I(t)$ and $s_Q(t)$ is concentrated at low frequencies around zero frequency, these components are also called *lowpass signals.*

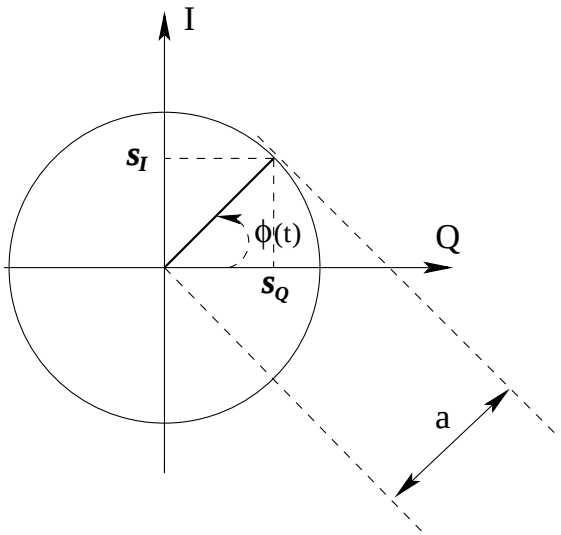

Figure 2.3: Polar diagram of the wave.

On that ground we can define *complex envelope* of a bandpass signal (Ziemer and Tranter, 2002, p. 79)

$$s_z(t) = s_I(t) + is_Q(t) \overset{(*)}{=} |s_z(t)|e^{i\phi(t)} \tag{2.1.2}$$

where $(*)$ means "phasor" form of the complex envelope $s_z(t)$ with complex modulus $|s_z(t)|$ that is equal to a signal amplitude $a(t)$

$$|s_z(t)| = \sqrt{s_I(t)^2 + s_Q(t)^2} = a(t). \tag{2.1.3}$$

So, the third and the commonly used representation of bandpass signal $s(t)$ by means of its complex envelope $s_z(t)$ is (Ziemer and Tranter, 2002, p. 81)

$$s(t) = \mathfrak{Re}[s_z(t)e^{i2\pi f_c t}]. \tag{2.1.4}$$

The signal represented by (2.1.4) is an alternative mathematical description of equation (2.1.1) since

$$\begin{aligned} s(t) &\overset{(2.1.4)}{=} \mathfrak{Re}[s_z(t)e^{i2\pi f_c t}] \\ &\overset{(2.1.2)}{=} \mathfrak{Re}[|s_z(t)|e^{i\phi(t)}e^{i2\pi f_c t}] \\ &\overset{(2.1.3)}{=} \mathfrak{Re}[a(t)e^{i(2\pi f_c t+\phi(t))}] \\ &= a(t)\cos(2\pi f_c t + \phi(t)). \end{aligned}$$

The exponential signal representation (2.1.4) is convenient to use since the amplitude envelope $a(t)$, the phase $\phi(t)$ and the carrier frequency f_c are easy to distinguish.

As a conclusion of this section we need to highlight two significant things about the carrier. First, the bandpass signal is described by any one of represented three forms. Second, the bandpass signal has a progress in time. Here, we need to emphasize that the signal amplitude is also depend on time (it is called the attenuation factor), for example, when the transmitter or the receiver moves. Deeper consideration and examination the nature of a signal is neglected since it is out the scope of this thesis.

2.1.2 Modulation

From section 2.1.1 we know that there are only three characteristics of a bandpass signal that can be changed over time: amplitude, phase and frequency. The process, or result of the process, of varying these characteristic of a bandpass signal in order to add information to it is called *modulation*; the bandpass signal is called *modulated* signal and the added information (or message signal) is called *modulating* signal. Depending on carrier's characteristic to be change, the modulation techniques are amplitude (AM), frequency (FM) or phase (PM) modulations. Figure 2.4 shows all three different modulations.

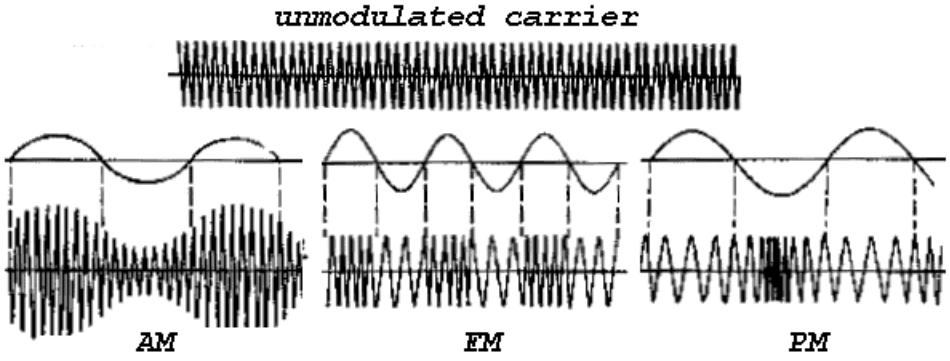

Figure 2.4: Three kind of modulations: AM, FM, PM.

Let us consider proper changes of a bandpass signal $s(t)$ described by the equation (2.1.1) with amplitude envelope $a(t) = a_c$ and zero phase

$$s(t) = a_c \cos(2\pi f_c t)$$

if these three different kinds of modulation are applied separately. Note, the modulations can be also combined and applied to the bandpass signal simultaneously, i.e. in Quadrature Amplitude Modulation amplitude and phase modulations are hold at once.

In AM the amplitude of bandpass signal is varied in accordance to amplitude of the modulating information signal $m(t)$. Thus, the AM signal can be represented as (Rappaport, 2002, p. 257)

$$s_{AM}(t) = a_c(1 + m(t)) \cos(2\pi f_c t).$$

FM and PM are forms of more general case of modulation called *angular modulation*. In angular modulation bandpass signal is modified so that the angle of the carrier is varied according to the amplitude of the modulating signal. At the same time the amplitude of the bandpass signal is kept constant, i.e., angular modulated bandpass signal is a constant envelope signal.

In FM, the most popular modulation used in communication systems, the instantaneous frequency of the bandpass signal is varied linearly with the modulating signal $m(t)$ as shown in (Rappaport, 2002, p. 265)

$$s_{FM}(t) = a_c \cos\left(2\pi f_c t + 2\pi k_f \int_{-\infty}^{t} m(\eta)d\eta\right)$$

where k_f is the frequency deviation constant.

In PM the angular of the bandpass signal is varied linearly with the modulating signal $m(t)$ as shown in (Rappaport, 2002, p. 265)

$$s_{PM}(t) = a_c \cos(2\pi f_c t + k_\theta m(t))$$

where k_θ is the phase deviation constant.

2.1.3 Multiple Access and Duplexing Techniques

In cellular system multiple access and duplexing are technologies for shared network.

The objective of multiple access is to provide different users carrying different kind of information with unique access to the shared resources (i.e. frequency, time, code or space) and their efficient use. The purpose of duplexing techniques is to share the same physical medium in two way communication and to distinguish transmission from MS to BS (uplink) with transmission from BS to MS (downlink). Note, different duplexing techniques can be combined with different multiple access. Also different multiple access can be applied in uplink and in downlink independently.

This section covers three basic multiple access methods: *Frequency Division Multiple Access* (FDMA), *Time Division Multiple Access* (TDMA) and *Code Division Multiple Access* (CDMA).

FDMA splits the frequency band into smaller fixed carrier frequencies. Then each separated frequency is assigned to some user basis.

TDMA divides the users in time so that they can share the same frequency. But only one user may use the shared channel in fixed time.

In CDMA systems, all users occupies the same carrier frequency and they are allowed to transmit simultaneously. Before the transmission each user additionally modulate the carrier by a very large bandwidth signal called the spreading signal that is a user specific code. Thus, the users are differed from each other in the code that is shared only between the user and BS.

So, the users are separated in frequency domain using FDMA and in time domain using TDMA. They are separated in encoding sequence using CDMA.

Not only users but also uplink and downlink transmission can be separated in different domains. In duplex communication division into uplink and downlink transmission can be realized in frequency domain known as *Frequency Division Duplex* (FDD) or in time domain known as *Time Division Duplex* (TDD).

FDD distinguishes uplink and downlink through frequency domain separation into two distinct sets of frequencies for uplink and downlink. Guard frequency interval splits up the sets for avoiding interference between uplink and downlink. Thus, uplink and downlink transmissions are carried out simultaneously but on different frequencies.

In TDD system the time domain instead of frequency domain is divided into two distinct sets of time slots for uplink and downlink. Here, the downlink and uplink occurs on the same frequency. And division in time domain is realized using fast switching: during one time step uplink signal is transmitted through the channel, during the next time step downlink signal is transmitted. But the time steps should be separated with guard time interval for avoiding interference between uplink and downlink and for equipment switching between receiving and transmitting mode.

For example, in GSM frequency domain is separated into 200 kHz carrier frequencies. Besides that, frequency domain is divided into up- and downlink by 45 MHz guard interval for distinguishing uplink transmission with downlink transmission. Each carrier frequency is then time divided into TDMA frames. TDMA frames are subdivided into eight slots (Romero et al., 2002).

Illustration of FDMA, FDD and TDMA techniques are represented in Figure 2.5.

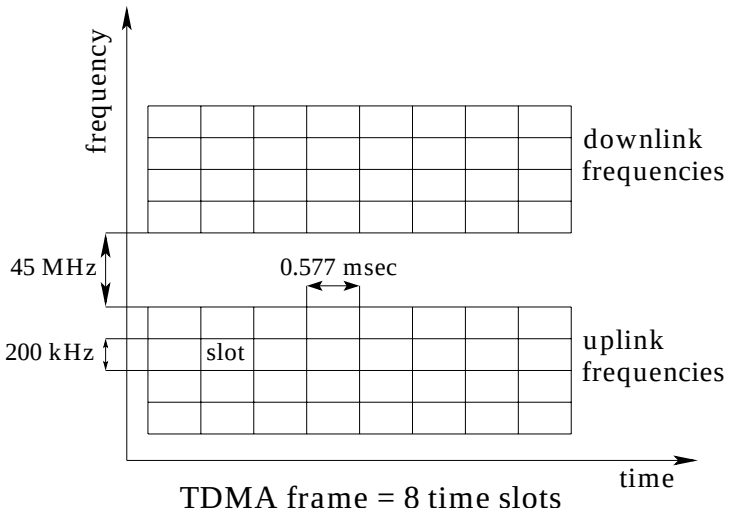

Figure 2.5: TDMA and FDMA with FDD techniques in GSM.

2.2 Structure of Cellular Network

The cellular networks, which main components are MSs, BSs and Base Station Subsystem (BSS), should solve two basic tasks: locating and monitoring of MSs and connecting MSs to the best possible available BS. There are different configurations of cellular network. Here, we introduce only macrocellular network configuration that is our main interest.

The macrocellular network can be represented as uniform grid, which cells have hexagonal shape. Figure 2.6 shows such a cell. In reality the cells are not hexagons, but have deformed and overlapped shapes. In each cell BS is located in the center. MSs that are distributed in the same cell are tracked by this BS. MSs communicate only with BS and are not allowed to communicate with each other or with MSs in the other cells. Hence, communication between MSs is indirect, and it is done through the BSs. The BSS has the controlling functions in the macrocellular network, and it realizes communication with other networks.

Furthermore, macrocellular network is characterized by the maximum number of supportable users per unit area and the cell coverage area. The cell coverage area A of a hexagon can be calculated with the cell radius ρ_0 as

$$A = \frac{3\sqrt{3}}{2}\rho_0^2. \tag{2.2.5}$$

So, if the total bandwidth B is used in each cell with coverage area A and frequency bandwidth B_u is required for each MS, then the maximum number of supportable users K is

$$K = \frac{B}{B_u A} \overset{(2.2.5)}{=} \frac{B}{B_u \rho_0^2 \frac{3\sqrt{3}}{2}}. \tag{2.2.6}$$

Thus, the number of supportable users is inversely proportional to the square of a cell radius and to the bandwidth required by each user.

If needs for network services increase, the maximum number of supportable users becomes insufficient to meet the requirements (Rappaport, 2002). At this point, the cellular design techniques should be applied to provide necessary number of supportable users. The commonly used techniques in practice are based on changes of cell radius or bandwidth required by each user. Smaller cells are possible to use in other cellular configuration (microcells, picocells). Smaller bandwidth B_u is possible to achieve with the help of FDMA described in the previous section.

2.2.1 Clustering

In the previous section we calculated the number of supportable users when the total frequency band B is reused in each cell in the network. But in practice, if mobile stations utilize the same frequency in neighbor cells, then mutual disturbance is too high. Instead of using the total bandwidth, each cell uses only the part of it. Hence, there is a set of cells that utilizes the total bandwidth B. Such set is called *cluster* and the solution for the network is called *clustering*.

The number of cells in each cluster, i.e. cluster size N, is limited by the formula (Stueberg, 2001, p. 17)

$$N = i^2 + ij + j^2 \quad \forall i \geq j \quad i, j \in \mathbb{Z}_*.$$

Usually cluster size $N = 1, 3, 4, 7, 9, 12 \ldots$

The frequency bandwidth valid for each cell inside the cluster is B/N and is denoted by *cell bandwidth*.

Using clustering the maximum number of supportable users per unit area given in (2.2.6) will decrease

$$K = \frac{B}{B_u A N} \overset{(2.2.5)}{=} \frac{B}{B_u \rho_0^2 N \frac{3\sqrt{3}}{2}}.$$

The maximum possible value of K is achieved with the minimum possible cell size N. But the cell size is lower bounded by mutual disturbances discussed above. In macrocellular network, where the total frequency is reused, the mean distance between the cells utilized the same frequency is called *mean reuse distance*. The number of supportable users K and mean reuse distance have the main influence to the network capacity.

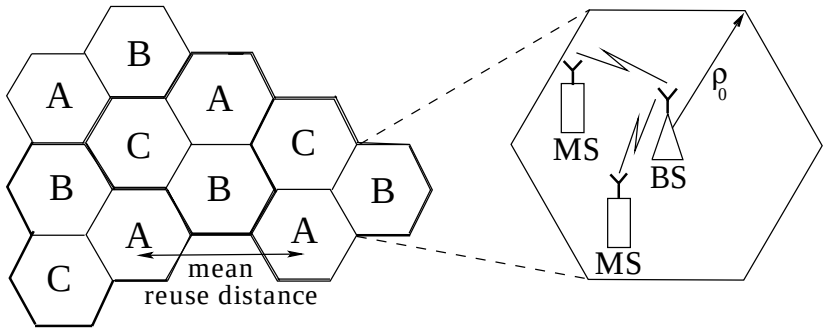

Figure 2.6: Macrocellular network.

In Figure 2.6 macrocellular network using clusters with 3 cells is depicted. The cells with the same letter inside utilizes the same set of frequencies.

2.2.2 Interference in the Network

Frequency reuse in macrocellular system with clustering introduces two kinds of interference, *co–channel* and *adjacent channel interference*, which limit the network capacity.

Co–channel interference arises due to utilization of the same frequency in different cells. Transmission signals from the cells with the same frequency are completely overlapped since they behave as the waves. Figure 2.7 presents the co–channel interference. In practice, only the first surrounding layer of the same frequency cells is taken into consideration, the rest co–channel interference is considered as negligible.

Adjacent channel interference arises when adjacent cells utilize spectrally adjacent set of frequencies. Inaccurate receiver filters, which allow neighboring frequencies to get into the passband, impact on adjacent channel interference (Rappaport, 2002). Careful filtering and channel assignment can help in minimizing adjacent channel interference.

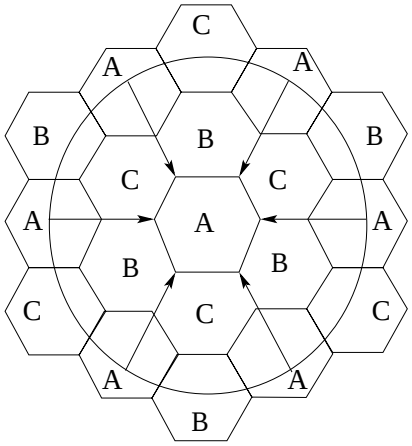

Figure 2.7: Co–channel interference in the macrocellular network with cluster size $N = 3$.

2.3 Radio Propagation

The properties of a radio channel have a strong relations with surrounding environment and the occupied frequency. Usually three basic mechanisms in surrounding environment affect the radio signal propagation. They are *reflection*, *scattering* and *diffraction* (Figure 2.8):

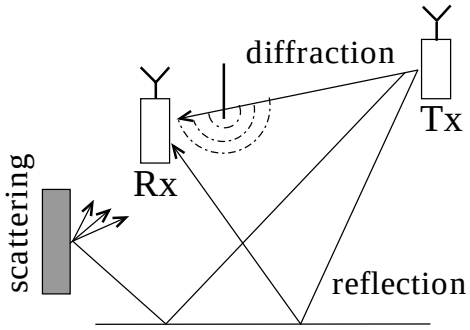

Figure 2.8: Three basic propagation mechanisms: reflection, scattering and diffraction.

- *Reflection* happens when a propagating wave is incident upon a smooth surface with great dimension compared to the wavelength (Sklar, 1997).
- *Scattering* happens when a propagation wave is incident upon either large rough surface or any surface whose dimension are on the order of a wavelength or less, causing the wave energy to be scattered in all directions (Sklar, 1997).
- *Diffraction* happens according to Huygens principle, when there is an obstacle with a great dimension compared to the wavelength between transmitter and receiver and secondary waves to be formed behind the obstacle (Sklar, 1997).

Each of these mechanisms impacts on signal propagation depending on particular surrounding environment. As a result, the transmitted signal is exposed to the attenuation, random fluctuation, variation and interference. Commonly, the signal variations can be characterized by two types of fading effects: *large–scale fading* and *small–scale fading*. In some literature they are also called slow fading and fast fading, respectively.

Large–scale fading represents, first, the mean signal attenuation or path loss due to spherical signal distribution and, second, the variance about the mean caused by the presence of obstacles between BS and MS. Small–scale fading results on the rapid signal level variations caused by many different propagation paths.

From mathematical point of view received signal $r(t)$ is usually described as transmitted signal $s(t)$ convoluted with the the channel impulse response $h_c(t)$ (Sklar, 1997)

$$r(t) = s(t) \star h_c(t) \tag{2.3.7}$$

in the case of noiseless condition.

But the received signal can be also expressed in terms of two independent component random variables (Sklar, 1997)

$$r(t) = m(t) \cdot r_0(t) \tag{2.3.8}$$

where $m(t)$ is the large–scale fading component, and $r_0(t)$ is the small–scale fading component.

2.3.1 Large–Scale Fading: Path Loss, Shadowing

Path Loss

A transmitted signal power is attenuated along the propagation path. When the distance between MS and BS is increasing, the signal power is decreasing. This power attenuation is called *path loss*.

Let us first consider propagation that takes place over idealized *free space*. Idealized free space is defined as follows (Sklar, 1997). There is no obstacles between BS and MS that might reflect or absorb radio frequency energy; atmosphere is being uniform; non-absorbing medium and the ground is located far away from the transmitted signal. Moreover, received antenna is assumed to be isotropic (received signal is caught in all directions) and the signal is transmitted without any direction.

Under such conditions the received power $P_r(\mathrm{W}/m^2)$ is attenuated by a *free space propagation loss factor* L_s (Rappaport, 2002, p. 107):

$$\begin{aligned} P_r(d)(W/m^2) &= G_r G_t \frac{P_t}{L_s} \\ &= G_r G_t \frac{P_t}{\left(\frac{4\pi d}{\lambda}\right)^2} \end{aligned} \tag{2.3.9}$$

where the transmitted power is denoted by T_r and G_t, G_r are the linear directivity gains of the transmitting and the receiving antenna, respectively.

In equation (2.3.9) path loss factor L_s is proportional to the square of the distance d between transmitter and receiver and to the square of the wavelength λ of the propagating signal.

The free space propagation path loss can also be expressed in decibels (Rappaport, 2002, p. 108) as

$$L_s(\text{dB}) = -10 \log_{10} G_r G_t \left(\frac{\lambda}{4\pi d}\right)^2$$

where $L_s(\lambda)$ dependence comes from antenna properties rather than propagation.

Usually the surround environment affects the propagation loss. So, the path loss factor is always higher (Sklar, 1997)

$$L_s(\text{dB}) = L_s(d_0)(\text{dB}) + 10n \log_{10} \frac{d}{d_0} \tag{2.3.10}$$

where a reference distance d_0 corresponds to a point located in the far field of the antenna and n is a path loss exponent. Ordinarily, d_0 is 1 km for macrocells. As we have seen in free space equation (2.3.9), the path loss exponent n is equal to 2. For typical urban area macrocellular environment n varies between 3 and 4. In buildings it ranges from 4 to 6. The path loss exponent strongly depends on a cell size and the surrounding environment.

Shadowing

Empirical studies show (Sklar, 1997) that the path loss $L_p(d)$ in decibels can be modeled accurately as a random variable having a log–normal distribution about the mean distant–dependent value $\overline{L_p}(d)$ (in decibels)

$$\begin{aligned} L_p(d)(\text{dB}) &= \overline{L_p}(d)(\text{dB}) + X_\sigma(\text{dB}) \\ &= L_s(d_0)(\text{dB}) + 10n \log_{10} \frac{d}{d_0} + X_\sigma(\text{dB}) \end{aligned} \tag{2.3.11}$$

where X_σ denotes a zero–mean Gaussian random variable in decibels with standard deviation σ also in decibels.

The path loss represented by the model (2.3.11) is referred to *shadowing*.

From the previous subsection we learned that the signal strength is attenuated when the distance between transmitter and receiver increases. But the channel also suffers from the obstacles that are located along the propagation path. These obstacles, like buildings, forests or hills, create radio shadows. This environmental attenuation effect is represented in shadowing.

Shadowing causes a variation in the received signal power local mean. The mean value $\overline{m}$ in dB follows the normal probability density function (PDF) (Romero et al., 2002, p. 153)

$$p(m) = \frac{1}{\sqrt{2\pi\sigma^2}} \exp\{\frac{-(m-\overline{m})^2}{2\sigma^2}\} \tag{2.3.12}$$

where σ is the standard deviation in decibels. Thus, if we want to construct reliable statistical model of large–scale fading in any arbitrary location, we need to take into

consideration the reference distance d_0, the path loss exponent n and the standard deviation σ of X_σ.

Shadow fading process described by log–normal distribution function is not enough for analyzing diversity. The correlation properties of large–scale fading are also should be taken into account. Thus, the following autocorrelation model can be proposed (Gudmundson, 1991)

$$R(d) = e^{-\frac{d}{d_{cor}} \ln 2} \tag{2.3.13}$$

where d is a distance between adjacent correlated fading values, in other words between adjacent locations, and d_{cor} is decorrelation parameter length depending on surrounding environment.

2.3.2 Small–Scale Fading: Multipath Propagation, Doppler Effect

Multipath Propagation

In surrounding environment the transmitted signal can be reflected and diffracted from the obstacles between MS and BS. As a result, received signal is made up of a number of replicas of the signal with random amplitude and phase (Romero et al., 2002).

This propagation effect of producing many different propagation paths between transmitter and receiver is known as *multipath* propagation. The multipath propagation is shown in Figure 2.9.

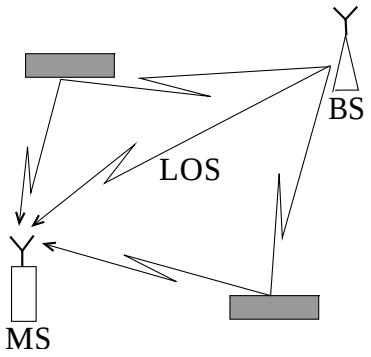

Figure 2.9: Multipath propagation.

Multipath propagation causes several problems such as the *delay spread* of the received signal and *Rayleigh fading* or random phase shift that causes rapid fluctuations in signal power. Small–scale fading is also caused by frequency shift called *Doppler effect* due to the motion of the mobile station.

Delay Spread

Because of multipath propagation the transmitted signal travels different paths that have different lengths and, consequently, have different path loss or are atten-

uated differently. Therefore, the signal follows the different paths that reach the receiver antenna and effect in slightly different times. As received signal is a vector sum of all received paths due to superposition principles of the waves, then multipath propagation causes the spread out of the signal in time. It might lead to the inter–symbol interference and might limit the maximum transmitted symbol rate.

Rayleigh Fading

Due to multipath propagation the interference of different paths with varying phase yields large amplitude fluctuations. As an example of multipath effect, let us imagine the following situation. The signal follows two paths: the direct path and the reflected path. The reflected path reaches the received antenna out of the phase with the direct path. Thus, direct signal and reflected signal cancel each other and received signal level drops. In this case multipath propagation causes the total attenuation of the received signal power.

Multipath propagation causes the signal amplitude random fluctuations. It is empirically proved that the magnitude of received complex envelope $\alpha(t) = |s_z(t)|$ (the definition of envelope is given in (2.1.2)), as a random variable, has a Rayleigh distribution, expressed as (Stueberg, 2001, p. 50)

$$p_\alpha(x) = \frac{x}{\sigma^2} \exp\{-\frac{x^2}{2\sigma^2}\} \quad \forall x \geq 0 \tag{2.3.14}$$

where σ^2 is the mean power.

In the case of presence significant unfaded component or line–of–sight (LOS) direct path, the magnitude has a Rician distribution. Rician distribution can be found for example in (Stueberg, 2001).

Doppler Effect

Because of multipath propagation and movement of the mobile station, the Doppler effect arises that causes difference between received signal frequency and transmitted signal frequency. This difference is called *Doppler shift*. The frequency shift measured in Hertz in time t heavily depends on mobile speed ϑ and on the angel θ_n of n^{th} incoming wave (Stueberg, 2001, p. 42):

$$f_{D,n}(\text{Hz}) = f_m \cos\theta_n \tag{2.3.15}$$

where $f_m = \vartheta/\lambda_c$ and λ_c is the wavelength of the arriving signal. So, due to the Doppler shift the original carrier frequency f_c is shifted by $f_{D,n}$, and it becomes $f_c + f_{D,n}$. In Figure 2.10 a typical incoming wave incident on a mobile station is shown.

Since

$$|f_{D,n}| = |f_m \cos\theta_n| \leq |f_m|,$$

the Doppler shift frequency is upper limited by f_m. Therefore, f_m is called the maximum Doppler frequency occurring when $\theta_n = 0$.

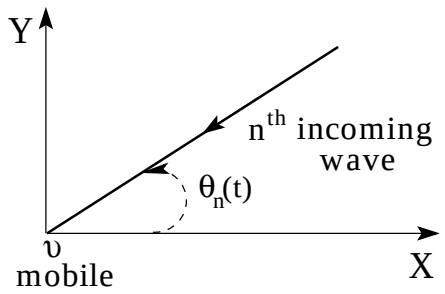

Figure 2.10: Doppler effect (Stueberg, 2001, p. 42).

2.4 Radio Resource Management

Radio Resource Management (RRM) is offered to improve network performance. The main RRM problem is the best resources (power, channels, spectrum) location in the network with certain quality of service (QoS) for the largest number of users.

One of the primary tasks for RRM is Interference Management (IM). From chapter 2.2.1 we know that network capacity directly depends on signal interference. So, Interference Management is meant to improve instantaneous signal quality and to reduce the negative affects of radio propagation such as interference and small–scale fading.

In this chapter we focus on three RRM (IM) algorithms: *power control* (PC), *link adaptation* (LA) and *frequency hopping* (FH).

Power Control

Power Control (PC) is a technique for regulating the transmission power. Power control is needed to maintain the signal strength and the signal quality within certain range.

In chapter 2.2 we discussed that the macrocellular network with clustering utilizes the same set of frequencies in different cells. Therefore, for reducing co–channel interference, low transmitted power is preferred. This regulation of transmitted power is done by PC algorithms.

So, the objective of Power Control is the reduction of overall interference level in the network and, additionally, on uplink to save the MSs batteries.

Link Adaptation

Radio link conditions are continuously varied due to system load, MSs movement, signal interference, transmission power and negative effects of surrounding environment. Selection of correct modulation and coding scheme can balance a lot these variations. This selection mechanism is known as Link Adaptation (LA).

More specifically, LA is used to select dynamically the optimum modulation and coding scheme based on channel quality estimates.

Frequency Hopping

Frequency hopping (FH) can be described as the change of the carrier frequency

between MS and BS. Different FH techniques allow to change the carrier frequency both after every transmitted burst and after every transmitted bit.

FH is used for reducing interference and small–scale fading in the receiver due to frequency selective characterization of a radio channel. The channel response of frequency–selective channel varies a lot in different frequency. Hence, the interference can be averaged changing the frequency using FH.

Chapter 3

Channel Models

The knowledge of radio channel behavior in the surrounding environment is essential for the design of the communication systems. In simulations the model of radio channel has to provide the required information necessary for studying such systems. Besides that, the channel models should be easy to implement and should fit the measurements conducted in various environments as well as possible.

In this chapter we attempt to explain the basics in channel models. Since the interest of this thesis lies on accurate estimation link performance and the combination link level results with system level, the nature of radio propagation should be studied in details.

First, we give the necessary mathematical background, after that we introduce statistical multipath channel model and then represent some channel model examples.

3.1 Mathematical Background

Our discussion in chapter 2.1.1 of the bandpass signal illustrates the time nature of the signal. But the radio signal has also equivalent representation in frequency domain. In this chapter we demonstrate how the Fourier Transformation leads to frequency domain signal structure, and we present the most useful theorem involving the Fourier Transform.

Furthermore, for analyzing complex received signal and for constructing reliable channel model, statistical approach is used. In this chapter we give the basic definitions and characteristics of random processes required for modeling radio propagation.

3.1.1 Fourier Transform

The *Fourier Transform* (FT) of a continuous and aperiodic function $f(x)$ is used to separate or decompose the function $f(x)$ into sinusoids of different frequency, which sum up the original function $f(x)$ in time domain. The FT distinguishes the sinusoid waves of different frequency and their respective amplitudes.

The FT applied to the function $f(x)$ is defined as (Ziemer and Tranter, 2002, p.

$$\mathcal{F}(\xi) = \int_{-\infty}^{\infty} f(x) e^{-i2\pi\xi x} dx \quad \xi \in \mathbb{R}. \tag{3.1.1}$$

The application of the same transform to $\mathcal{F}(\xi)$ yields

$$f(w) = \int_{-\infty}^{\infty} \mathcal{F}(\xi) e^{-i2\pi w\xi} d\xi \quad w \in \mathbb{R}.$$

If $f(x) = f(-x)$, that is $f(x)$ is an even function of x, then $f(w) = f(x)$. If $f(x) = -f(-x)$, that is $f(x)$ is an odd function of x, then $f(w) = f(-x)$. When $f(x)$ is neither even nor odd, it can often be split into even or odd parts. For avoiding this procedure the *Inverse Fourier Transform* (IFT) is defined as (Ziemer and Tranter, 2002, p. 36)

$$f(x) = \widehat{\mathcal{F}}(x) = \int_{-\infty}^{\infty} \mathcal{F}(\xi) e^{i2\pi\xi x} d\xi \quad x \in \mathbb{R}. \tag{3.1.2}$$

The IFT rebuilds the original function from its FT.

The most essential for us result in the Fourier theory is represented in the following theorem (Bracewell, 1999, pp. 108-112).

Theorem 3.1.1 (The convolution theorem)

$$\mathcal{F}\{f(x) \star g(x)\} = \mathcal{F}\{f(x)\} \cdot \mathcal{F}\{g(x)\}$$

where $\star$ denotes the convolution, $\cdot$ denotes the scalar product.

Proof.

$$\begin{aligned}
\mathcal{F}\{f(x) \star g(x)\} &= \mathcal{F}\left\{\int_{-\infty}^{\infty} f(\tau) g(x-\tau) d\tau\right\} \\
&\overset{(3.1.1)}{=} \int_{-\infty}^{\infty} \left\{\int_{-\infty}^{\infty} f(\tau) g(x-\tau) d\tau\right\} e^{-i2\pi\xi x} dx \\
&= \int_{-\infty}^{\infty} \int_{-\infty}^{\infty} f(\tau) g(x-\tau) e^{-i2\pi\xi x} d\tau dx \\
&\overset{(*)}{=} \int_{-\infty}^{\infty} \int_{-\infty}^{\infty} f(\tau) g(x-\tau) e^{-i2\pi\xi x} dx d\tau \\
&= \int_{-\infty}^{\infty} f(\tau) \int_{-\infty}^{\infty} g(x-\tau) e^{-i2\pi\xi x} dx d\tau \\
&= \int_{-\infty}^{\infty} f(\tau) \left\{\int_{-\infty}^{\infty} g(x-\tau) e^{-i2\pi\xi(x-\tau)} dx\right\} e^{-i2\pi\xi\tau} d\tau \\
&= \int_{-\infty}^{\infty} f(\tau) e^{-i2\pi\xi\tau} d\tau \cdot \mathcal{F}\{g(x)\} \\
&= \mathcal{F}\{f(x)\} \cdot \mathcal{F}\{g(x)\}
\end{aligned}$$

The Fubini theorem is applied in $(*)$ transition. $\square$

The main contribution of the convolution theorem 3.1.1 is the substitution of the convolution to the multiplication. Thus, the convolution of functions can be replaced by the FT of each function separately and then multiplying them point wise. Additional applying the IFT to the scalar product, allow to return back to the original domain. The difference in computational complexity is essential: the convolution of vectors with length n takes $\mathcal{O}(n^2)$ multiplications, whereas using the convolution theorem 3.1.1 the convolution operation takes only $\mathcal{O}(n \log n)$.

3.1.2 Discrete Fourier Transform

In the previous section we described the FT applied to continuous and aperiodic function of one variable $f(x)$. Now we want to present the discrete representation of the FT and the IFT since it is always used in numerical calculations.

The *Discrete Fourier Transform* (DFT) is a discrete version of the discrete–time Fourier Transform. The DFT unlike the FT is applied to a discrete complex valued sequence $f(x)$ with length N

$$f(0),\ f(1),\ \ldots,\ f(N-1)$$

that is a cycle extended with period N, $f(x) = f(x+N)$ for all x.

The DFT applied to this sequence is a sequence itself. It is defined as (Ziemer and Tranter, 2002, p. 83)

$$\mathcal{F}(\xi) = \frac{1}{N} \sum_{x=0}^{N-1} f(x) e^{-i2\pi\xi x/N} \quad 0 \leq \xi \leq N-1. \tag{3.1.3}$$

The important property of the DFT that it is also a cyclic with period N, $\mathcal{F}(\xi) = \mathcal{F}(\xi + N)$ for all ξ.

The inverse transform called the *inverse DFT* (IDFT) is defined as (Ziemer and Tranter, 2002, p. 83)

$$f(x) = \sum_{\xi=0}^{N-1} \mathcal{F}(\xi) e^{i2\pi\xi x/N} \quad 0 \leq x \leq N-1. \tag{3.1.4}$$

The IDFT rebuilds the original sequence from its DFT.

The DFT of N length sequence in discrete time domain is used to transform it into N length sequence in discrete frequency domain.

3.1.3 Random Processes

The definitions presented here and in the following sections of chapter 3.1 are mostly based on (Shanmugan and Breipohl, 1988). They are slightly reformed to suit this thesis.

Definition 3.1.1 *Let us $\mathcal{S}$ denote a sample space of a random experiment. Let t denote a random variable such that $t \in \mathcal{E} \subset \mathbb{R}$. A map $X : \mathcal{E} \times \mathcal{S} \longrightarrow \mathbb{R}$ is called a real–valued random process if $X(t)$ is a measurable function on $\mathcal{E} \times \mathcal{S}$. A map $Z : \mathcal{E} \times \mathcal{S} \longrightarrow \mathbb{C}$ is called a complex–valued random process if $Z(t) = X(t) + iY(t)$ is a measurable function on $\mathcal{E} \times \mathcal{S}$ where $X(t)$, $Y(t)$ are real–valued random processes.*

A random process $X(t)$ is described by the following first and second order characteristics.

The *mean* $\mu_X(t)$ of the random process $X(t)$ is

$$\mu_X(t) = E\{X(t)\}.$$

Using linearity of the expectation operator $E\{\cdot\}$, i.e.

$$E\{\alpha x + \beta y\} = \alpha E\{x\} + \beta E\{y\},$$

where $\alpha, \beta \in \mathbb{R}$ and x, y – random variables, the *expected value* $E\{Z(t)\}$ of a complex–valued random process $Z(t)$ is

$$E\{Z(t)\} = E\{X(t)\} + iE\{Y(t)\}.$$

The *autocorrelation* $R_X(t_1, t_2)$ of the random process $X(t)$ is

$$R_X(t_1, t_2) = E\{X^*(t_1)X(t_2)\}$$

where superscript * stands for conjugation.

The autocorrelation measures correlation between samples of the random process taken at different times.

The *autocovariance* $C_X(t_1, t_2)$ of the random process $X(t)$ is

$$C_X(t_1, t_2) = R_X(t_1, t_2) - \mu_X^*(t_1)\mu_X(t_2).$$

A pair of random processes $X(t)$ and $Y(t)$ are jointly characterized by the *cross-correlation* $R_{XY}(t_1, t_2)$ and the *crosscovariance* $C_{XY}(t_1, t_2)$.

$$\begin{aligned} R_{XY}(t_1, t_2) &= E\{X^*(t_1)Y(t_2)\} \\ C_{XY}(t_1, t_2) &= R_{XY}(t_1, t_2) - \mu_X^*(t_1)\mu_Y(t_2) \end{aligned}$$

Definition 3.1.2 *A random process $X(t)$ is called wide sense stationary (WSS) if its mean value is constant, $\mu_X(t) = E\{X(t)\} = \mu_X$, and for all $t_1, t_2, \tau = t_2 - t_1 \in \mathbb{R}$ hold*

$$R_X(t_1, t_2) = R_X(\tau).$$

Thus, WSS process is fully described by constant mean and autocorrelation function that depends only on time difference.

The autocovariance $C_X(t_1, t_2)$ of WSS process $X(t)$ can be retrieved from definition 3.1.2 directly

$$\begin{aligned} C_X(t_1, t_2) &= R_X(t_1, t_2) - \mu_X^*(t_1)\mu_X(t_2) \\ &= R_X(\tau) - \mu_X^*\mu_X \\ &= R_X(\tau) - |\mu_X|^2 \\ &= C_X(\tau) \end{aligned}$$

where τ is defined as time difference.

3.1.4 Power Spectral Density and White Noise

In the previous section we studied the random processes in time domain. Another approach is to analyze the random processes in the Fourier space, i.e. in frequency domain. The spectral properties of the random processes can be studied by means of the *Power Spectral Density function* (PSD) as a function of frequency. The PSD function is defined only for WSS processes and is called *spectrum* of the random process.

Definition 3.1.3 *Let $X(t)$ be a random WSS process in time domain, and $R_X(\tau)$ its autocorrelation function. The Fourier Transform of $R_X(\tau)$ is called the PSD function $S_X(f)$ in frequency domain*

$$S_X(f) = \mathcal{F}\{R_X(\tau)\} = \int_{-\infty}^{\infty} R_X(\tau) e^{-i2\pi f\tau} d\tau.$$

The application of the IFT to the PSD function $S_X(f)$ yields back the autocorrelation function

$$R_X(\tau) = \widehat{\mathcal{F}}\{S_X(f)\} = \int_{-\infty}^{\infty} S_X(f) e^{i2\pi f\tau} df.$$

The objective of using the PSD function is to characterize stochastic random process in terms of its power. Thus, integrating the PSD function in frequency domain, we obtain an expected (average) power of the random process $X(t)$

$$E\{X(t)^2\} = R_X(t_1, t_1) \overset{WSS}{=} R_X(0) \overset{(3.1.2)}{=} \int_{-\infty}^{\infty} S_X(f) df.$$

So, both functions, the PSD and autocorrelation, are characteristics of stochastic processes. In frequency domain the PSD as the FT of the autocorrelation characterizes stochastic processes, in time domain autocorrelation as the IFFT of the PSD characterizes stochastic processes.

Definition 3.1.4 *A random WSS process $W(t)$ is called a white noise if its autocorrelation function is*

$$R_W(\tau) = \sigma_W^2 \delta(\tau)$$

where $\sigma_W^2 = const$ is an intensity of white noise, $\delta(\tau)$ is Dirac's delta function.

The definition 3.1.4 shows that the autocorrelation of white noise is zero except at the origin whose value represents the variance of the random process $W(t)$.

The white noise is also characterized by its flat PSD function since

$$S_W(f) \overset{(3.1.1)}{=} \int_{-\infty}^{\infty} \sigma_W^2 \delta(\tau) e^{-i2\pi f\tau} d\tau = \sigma_W^2.$$

3.2 Channel Modeling: Impulse Response and Transfer Function

Typical multipath fading channel in wireless communication is modeled as a *linear time–variant system.*

For understanding the nature of channel model we need to look through the following notions. The *system* can be described as a black box or an object that generates the output depending on the input and some initial conditions. The *linear system* $\mathcal{L}$ is a subset of all systems. The linear system holds two properties (Ziemer and Tranter, 2002, p. 53): homogeneous

$$\mathcal{L}(\alpha x) = \alpha \mathcal{L}(x)$$

and additivity

$$\mathcal{L}(x_1 + x_2) = \mathcal{L}(x_1) + \mathcal{L}(x_2)$$

where $\alpha \in \mathbb{R}$ and x, x_1, x_2 are some inputs.

The system is referred to be *time–variant* if its output changes in time. The output of a linear time–variant system is uniquely determined by convolution of the input with the *impulse response* $h(\tau; t)$ defined as the system response to the unit impulse $\delta(t - \tau)$ (Ziemer and Tranter, 2002, pp. 53-54).

The impulse response can be measured by applying WSS white noise with zero mean and by cross-correlating the output with a delayed replica (Bracewell, 1999).

Presented properties of linear system help us to prove that the multipath channel can be modeled as linear time–variant system. In chapter 2.1.1 we learned that transmitted signal $x(t)$ is expressed by means of its complex envelope $x_z(t)$

$$x(t) \overset{(2.1.4)}{=} \mathfrak{Re}[x_z(t)e^{i2\pi f_c t}]. \tag{3.2.5}$$

In chapter 2.3 we showed that due to multipath fading propagation received complex envelope $y_z(t)$ is described as a vector sum of L different paths where each l^{th} path, $1 \leq l \leq L$, is attenuated by path loss $\alpha_l(t)$ and arrives with time delay $\tau_l(t)$

$$y_z(t) = \sum_{l=1}^{L} \alpha_l(t) x_z(t - \tau_l(t)).$$

Let us now consider the general case of multipath fading. Suppose MS moves with a velocity v. Then the Doppler shift $f_{D,l}$ in frequency (2.3.15) arises on each l^{th} path, and the received bandpass signal is written as (Stueberg, 2001, p. 42)

$$\begin{aligned} y(t) &\overset{(3.2.5)}{=} \mathfrak{Re}\left[\sum_{l=1}^{L} \alpha_l(t) x_z(t - \tau_l(t)) e^{i2\pi(f_c + f_{D,l})(t - \tau_l(t))}\right] \\ &= \mathfrak{Re}\left[e^{i2\pi f_c t} \sum_{l=1}^{L} \alpha_l(t) x_z(t - \tau_l(t)) e^{-i2\pi[(f_c + f_{D,l})\tau_l(t) - f_{D,l} t]}\right]. \end{aligned}$$

Hence, the complex envelope of received signal $y(t)$ is given by

$$\begin{aligned} y_z(t) &= \sum_{l=1}^{L} \alpha_l(t) e^{-i2\pi[(f_c+f_{D,l})\tau_l(t)-f_{D,l}t]} x_z(t-\tau_l(t)) \\ &= \int_{-\infty}^{\infty} h(\tau;t) x_z(t-\tau) d\tau \\ &= h(\tau;t) \star x_z(t) \end{aligned} \tag{3.2.6}$$

where $h(\tau;t)$ is the channel impulse response at time t applied to instant $t-\tau$ in time domain

$$h(\tau;t) = \sum_{l=1}^{L} \alpha_l(t) e^{-i\phi_l(t)} \sigma(\tau-\tau_l(t)) \tag{3.2.7}$$

with the phase of each path

$$\phi_l(t) = 2\pi[(f_c + f_{D,l})\tau_l(t) - f_{D,l}t].$$

We need to emphasize that the impulse response experiences two kinds of behavior: time–spreading behavior due to multipath propagation and time–variant behavior due to motion. Delay time τ and transmission time t characterize these two different time behaviors.

In simulations $\alpha_l(t)$ and $\tau_l(t)$ are modeled as stochastic processes, therefore, with a large number of paths L the central limit theorem can be applied to model the time–variant impulse response of the channel as a complex Gaussian random process. If the impulse response is modeled as a zero mean complex Gaussian random process, then its envelope is Rayleigh distributed as shown in appendix A. That is why the channel is said to be a *Rayleigh fading channel*. More detailed description is given in (Rappaport, 2002).

With equation (3.2.6) we showed that the channel can be modeled as a linear time–variant system since we expressed $y_z(t)$ by convolution of the complex envelope of the channel input $x_z(t)$ with the impulse response $h(\tau;t)$ in time domain.

Presented channel model (3.2.6) reflects the time dispersion and frequency–selective fading due to multipath propagation. The radio channel is called non–frequency–selective, *flat*, if complex channel gain is constant for different paths and bandwidth of transmitted signal is smaller than channel bandwidth (Rappaport, 2002). The radio channel is called *frequency–selective* otherwise. The impulse response (3.2.7) refers to frequency–selective fading channel while flat fading channel impulse response has simpler structure (Stueberg, 2001, p. 43)

$$h(\tau;t) = \sum_{l=1}^{L} \alpha_l(t) e^{-i\phi_l(t)} \sigma(\tau-\hat{\tau}) = h(t)\sigma(\tau-\hat{\tau}) \tag{3.2.8}$$

where different path delays are small compared to duration of modulated symbol. So, all of them are approximately equal to $\hat{\tau}$.

In frequency domain channel is characterized by its frequency response $H(f;t)$ defined as the FT of the impulse response $h(\tau;t)$ (Ziemer and Tranter, 2002, p. 55)

$$H(f;t) \overset{(3.1.1)}{=} \int_{-\infty}^{\infty} h(\tau;t)e^{-i2\pi f\tau}d\tau$$
$$\overset{(*)}{=} \sum_{l=1}^{L} \alpha_l(t)e^{-i(\phi_l+2\pi f)\tau_l(t)}. \tag{3.2.9}$$

Here, $(*)$ transition is possible due to sifting property of Dirac's delta function

$$\int f(x)\delta(x-x_0)dx = f(x_0).$$

If within the set of frequencies $|H(f;t)|$ is constant or change is not significant, the channel is said to be flat and frequency–selective, otherwise.

By means of the frequency response characterization of the radio channel and the convolution theorem 3.1.1 we can represent channel model (3.2.6) in frequency domain. Let us $Y_z(f)$, $X_z(f)$ and $H(f;t)$ denote the FT of the complex envelopes $y_z(t)$, $x_z(t)$ and the impulse response $h(\tau;t)$, respectively. Hence, in frequency domain convolution is replaced by multiplication, and channel model is written as (Ziemer and Tranter, 2002, p. 54)

$$Y_z(f) = H(f;t) \cdot X_z(f). \tag{3.2.10}$$

Both, the channel model in time domain (3.2.6) and the channel model in frequency domain (3.2.10), describe only the distortion that the transmitted signal gets due to multipath fading propagation. But generally, in radio channel the transmitted signal is also corrupted by thermal noise as depicted in Figure 3.1. Thus, the received complex envelope $y_z(t)$ is defined as (Stueberg, 2001, p. 228)

$$y_z(t) = \int_{-\infty}^{\infty} h(\tau;t)x_z(t-\tau)d\tau + n(t) \tag{3.2.11}$$

where n(t) is zero–mean additive white Gaussian noise (AWGN) with PSD of $\frac{N_0}{2}$.

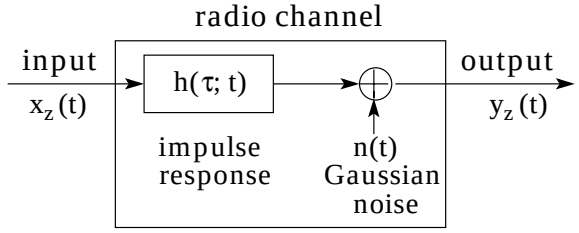

Figure 3.1: Radio channel model.

We need to introduce one special case of general channel model (3.2.11) called *AWGN channel*. If the channel impulse response is time–invariant constant expressed as a constant complex channel gain h

$$h(\tau;t) = h\sigma(\tau), \tag{3.2.12}$$

then channel experiences only AWGN without any fading. Substituting this channel impulse response to the general channel model we obtain

$$\begin{aligned} y_z(t) &\overset{(3.2.12)}{=} \int_{-\infty}^{\infty} h\sigma(\tau)x_z(t-\tau)d\tau + n(t) \\ &\overset{(*)}{=} hx_z(t) + n(t). \end{aligned} \tag{3.2.13}$$

Thus, we can defined the AWGN channel model as the addition of white Gaussian noise to the transmitted signal. Here, $(*)$ transition is possible due to sifting property of Dirac's delta function.

3.3 Tap Model

Usually statistical approach is used to construct a channel model that fits the measurements and to generalize the model over some typical environment. For statistical analyzes of channel characteristics the measurements are conducted in different propagation environments where the unit pulse is transmitted through the channel.

From chapter 2.3 we know that the propagation environment effects the transmitted signal. So, to estimate the received signal level both types of fading, the large–scale fading and the small–scale fading, of radio channel have to be taken into account.

In section 2.3.1 we demonstrated that the large–scale fading is the slow variation of the mean signal power over time that depends on MS and BS positions and on the presence of obstacles in the propagation path. As a slow process the large–scale fading is modeled by log–normal distribution (2.3.12) that describes random shadow fading process.

In section 2.3.2 we showed that the small–scale fading reflects three different reactions: rapid fluctuations in signal strength, time dispersion caused by multipath propagation and random frequency modulation due to Doppler frequency shifts of different paths. In this chapter we focus only on small–scale fading model directly connected to the channel model (3.2.6) and the channel impulse response (3.2.7). In this chapter we present how the frequency–selective multipath channel can be modeled by a number of uncorrelated flat multipath channels.

The small–scale fading of a radio channel is statistically analyzed by the *root mean square (RMS) delay spread* and *maximum excess delay*, first, and then the channel is modeled using tapped delay line model or *tap model*. These parameters describe frequency–selective nature of the channel.

The RMS delay spread is the most important single parameter that measures the extent of time dispersion introduced by multipath propagation, i.e. it is a measure of multipath delay spread. The RMS delay spread is calculated as the square root of the second central moment of the normalized power delay profile (Rappaport, 2002,

p. 199).[1]

$$\begin{aligned}\tau_{rms} &= \sqrt{\overline{\tau^2} - \overline{\tau}^2} \\ \overline{\tau^2} &= \frac{\sum_{k=1}^{m} P_k \tau_k^2}{\sum_{k=1}^{m} P_k} \\ \overline{\tau} &= \frac{\sum_{k=1}^{m} P_k \tau_k}{\sum_{k=1}^{m} P_k}\end{aligned}$$

The coherence bandwidth B_c of the channel, that is defined as range of frequencies over which the channel response is unchanged or flat, is inversely proportional to RMS delay (an exact relationship between RMS delay profile and the coherence bandwidth does not exist, it must be derived from signal analysis using Fourier techniques). The coherence bandwidth represents a frequency range over which the frequency components have a strong potential for amplitude correlation (Sklar, 1997).

The coherence bandwidth or respectively RMS delay spread are essential parameters for transmitted data rate. In radio communication without special techniques against multipath effects the transmitted data rate should be much smaller the coherence bandwidth for avoiding inter–symbol interference (Sklar, 1997)

$$Rate < B_c \cong \frac{1}{\alpha \tau_{rms}} \tag{3.3.14}$$

where parameter $\alpha \in \mathbb{R}$. If the coherence bandwidth is defined as a bandwidth over which the frequency correlation function is at least 0.9, then $\alpha = 50$ (Rappaport, 2002, p. 202).

The tap model with predefined number of taps models the frequency–selective channel. For constructing the tap model the number of taps is usually chosen as a trade–off between complexity and reliability of the model. Each tap experiences multipath fading as a result of a large number of multipath components. Each tap is characterized by the complex tap gain and the tap delay. Although in multipath propagation path delays are usually random, in the tap model they are fixed. The tap model with n number of taps has the following impulse response (Stueberg, 2001, p. 90)

$$h(\tau; t) = \sum_{k=1}^{n} h_k(t) \sigma(\tau - \tau_k)$$

where $h_k(t)$ is complex gain and τ_k is path delay of k^{th} tap. Let us remark that the channel impulse response of the tap channel model is obviously constructed on the ground of presented impulse response (3.2.7). Thus, the application of channel model properties yields the received envelope $y_z(t)$ to be defined by convolution of transmitted envelope $x_z(t)$ with the tap channel impulse response

$$y_z(t) \overset{(3.2.6)}{=} \sum_{k=1}^{n} h_k(t) x_z(t - \tau_k).$$

[1] P_k is equal to a path amplitude Ω_k (3.3.15) of the tap model

So, the tap model is fully described by the complex gain vector $\mathbf{h}(t) = [h_1(t), h_2(t), \ldots, h_n(t)]$ and the tap delay vector $\tau = [\tau_1, \tau_2, \ldots, \tau_n]$. Each tap gain $h_k(t)$ represents received complex envelope $y_z(t)$ been transmitted through multipath flat fading channel

$$\begin{aligned} h_k(t) &\overset{(3.2.8)}{=} \sum_{l=1}^{L} \alpha_l(t) e^{-i\phi_l(t)} \\ &= \alpha(t) e^{-i\phi(t)} \quad 1 \le k \le n. \end{aligned}$$

with a large number of paths L and assumption

$$\alpha_l(t) = \alpha_l, \quad \tau_l(t) = \tau_l$$

for a shot period of time. The central limit theorem can be applied to model the tap gain $h_k(t)$ as a complex Gaussian random process

$$h_k(t) \overset{(2.1.2)}{=} h_{kI}(t) + i h_{kQ}(t)$$

where quadrature components $h_{kI}(t)$ and $h_{kQ}(t)$ are WSS Gaussian random processes. From section 3.1.4 we know that each tap gain as WSS process can be statistically analyzed by autocorrelation in time domain or the PSD in frequency domain called Doppler spectrum in this case. The general form of autocorrelation is given in (Stueberg, 2001). We want to present only widely used special case of it. For macrocellular network the path lengths are long compared to the antenna heights. Hence, the following simplification can be made: the plane waves propagate in a 2-D (x, y) plane and arrive at the MS from all directions with equal probability, i.e. $p(\theta) = \frac{1}{2\pi}$, $\theta \in [-\pi, \pi]$. This model is commonly referred to *isotropic scattering model* and is firstly suggested by Clarke (Stueberg, 2001, p. 45). For isotropic scattering Rayleigh fading model the autocorrelation function is given by (Stueberg, 2001, p. 91)

$$R_{h_k}(\tau) = \frac{\Omega_k}{2} J_0(2\pi f_m \tau) \quad 1 \le k \le n \tag{3.3.15}$$

where $\Omega_k = E\{|h_k(t)|^2\}$ is the average envelope power associated with k^{th} path gain, $J_0(\cdot)$ is the zero–order Bessel function of the first kind, f_m is the maximum Doppler frequency (2.3.15). The application of the FT to the autocorrelation $R_{h_k}(\tau)$ yields the envelope Doppler spectrum of k^{th} path gain

$$S_{h_k}(f) = \begin{cases} \frac{\Omega_k}{2\pi f_m} \frac{1}{\sqrt{1-(f/f_m)^2}} & \text{if } |f| < f_m, \\ 0 & \text{otherwise} \end{cases} \tag{3.3.16}$$

The Doppler spectrum (3.3.16) is standardized in 3^{rd}GPP (3rd Generation Partnership Project, 06) as CLASS or Classical Doppler spectrum.

The tap model represented in Figure 3.2 characterizes the radio channel in terms of average envelope powers and delays.

So, in simulations frequency–selective multipath radio channel in specified environment can be modeled according to the tap model standardized for this environment. The tap model itself is described by fixed tap delay vector and fixed average envelope power vector. The time varying complex tap gains should be generated with the specified Doppler spectrum.

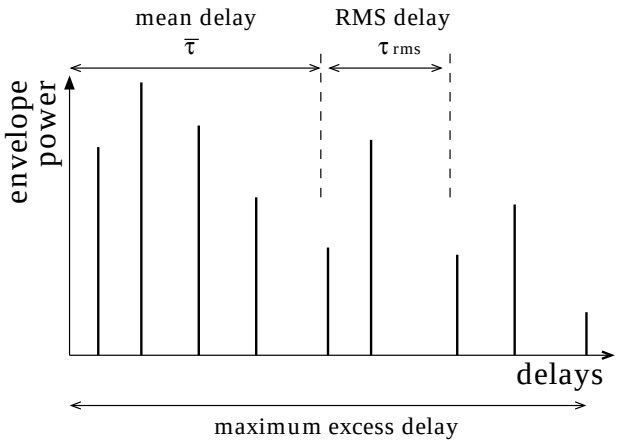

Figure 3.2: Channel characterization in a tap model.

3.4 Channel Model Examples: GSM TU, ETSI BRAN A

Let us now consider two concrete examples of channel tap model: "Typical Urban" model (TU), whose number of taps, taps coefficients α_i and tap delays τ_i are defined in GSM technical specification (3rd Generation Partnership Project, 06) and "ETSI BRAN A" model that is specified in ETSI BRAN standardization (Medro, 1998; Subgroup, 1998).

The tap model presented in the previous chapter is described by a number of taps, the amplitude paths, having average relative powers[2] $|h_i|^2$ measured in decibels (dB) and tap delays τ_i measured in microseconds (μs) and variation model.

TU model realizes the narrowband radio channel in the outdoor urban environment at 900 MHz. TU model is usually defined by 12 tap settings, but for simplification, if in simulations the complete model is not possible to simulate, 6 taps TU model is proposed. For TU model two alternative tap settings are given. TU model with 6 taps is represented in Table 3.1 and graphical representation of TU (1) model is shown in Figure 3.3. In TU model the Doppler spectrum corresponding to a speed of 3 km/h is classical (3.3.16) for all taps.

ETSI BRAN A is a channel model for the indoor typical office radio channel at 5 GHz. It is supposed to be used in HIPERLAN/2 link level simulations. It is defined by 18 taps settings. All taps have Rayleigh fading statistics and a classical Doppler spectrum (3.3.16) corresponds to a terminal speed of 3 km/h. Taps are spread within $[0, \tau_{rms} = 50ns]$ interval. ETSI BRAN A channel model is specified in Table 3.2 and graphical representation of ETSI BRAN A is shown in Figure 3.4.

[2] $|h_i|^2$ in some literature are called tap coefficients

Table 3.1: GSM TU model.

Tap number	Relative time (μs)		Average relative power (dB)	
	(1)	(2)	(1)	(2)
1	0.0	0.0	-3.0	-3.0
2	0.2	0.2	0.0	0.0
3	0.5	0.6	-2.0	-2.0
4	1.6	1.6	-6.0	-6.0
5	2.3	2.4	-8.0	-8.0
6	5.0	5.0	-10.0	-10.0

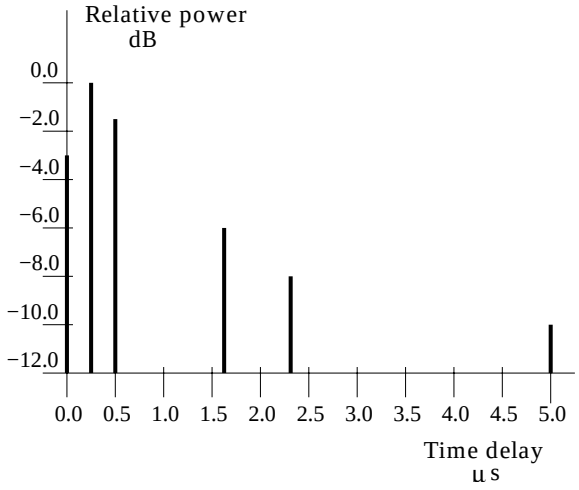

Figure 3.3: Graphical representation of TU model with 6 taps

Table 3.2: ETSI BRAN A model.

Tap number	Relative time (ns)	Average relative power (dB)
1	0.0	0.0
2	10	-0.9
3	20	-1.7
4	30	-2.6
5	40	-3.5
6	50	-4.3
7	60	-5.2
8	70	-6.1
9	80	-6.9
10	90	-7.8
11	110	-4.7
12	140	-7.3
13	170	-9.9
14	200	-12.5
15	240	-13.7
16	290	-18.0
17	340	-22.4
18	390	-26.7

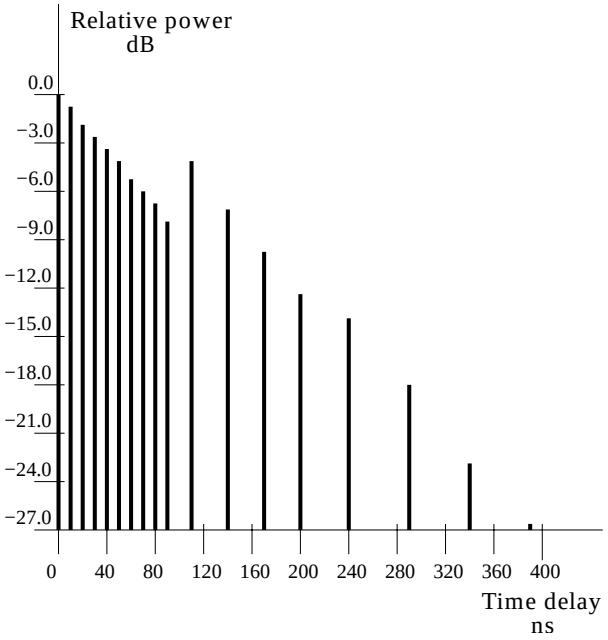

Figure 3.4: Graphical representation of ETSI BRAN A model.

Chapter 4

MIMO

Digital communication using multiple–input–multiple–output (MIMO) wireless system has recently become one of the most promising research areas in modern communications. MIMO systems promise high spectral efficiency since they allow transmission through parallel channels separated in spatial domain. In this chapter we present the signal model of MIMO system and describe flat fading MIMO channel in details. We attempt to explain the benefits of MIMO techniques. And also, we represent the the information theoretic capacity of MIMO system shown in (Foschini, 1996; Telatar, 1995).

The fundamentals of MIMO wireless system are essential for this thesis due to our suggestion and our further research of new technique for communication systems with MIMO.

4.1 Overview

MIMO system is referred to an arbitrary wireless system with multiple transmitting and/or receiving antenna elements (Telatar, 1995). Multiple antennas create a channel matrix $\mathbf{H}$, which size is equal to the number of transmitting antennas times the number of receiving antennas. The MIMO system diagram is illustrated in Figure 4.1. The following description of the whole process is given in (Gesbert et al., 2003).

"A compressed digital source in the form of binary data stream is fed to a simplified transmitting block encompassing the functions of error control coding and (possibly joined with) mapping to complex modulation symbols (quaternary phase–shift keying (QPSK), M-QAM, etc.). The latter produces several separate symbol streams which range from independent to partially redundant to fully redundant. Each is then mapped onto one of multiple transmitting antennas. Mapping may include linear spatial weighting of the antenna elements or linear antenna space–time precoding. After upward frequency conversation, filtering and amplification, the signals are launched into the wireless channel. At the receiver, the signals are captured by possibly multiple antennas and demodulation and demapping operations are performed to recover the message."

The goal to use MIMO system is to offer higher capacity and more reliable communication link in the presence of multipath fading and interference. Thus,

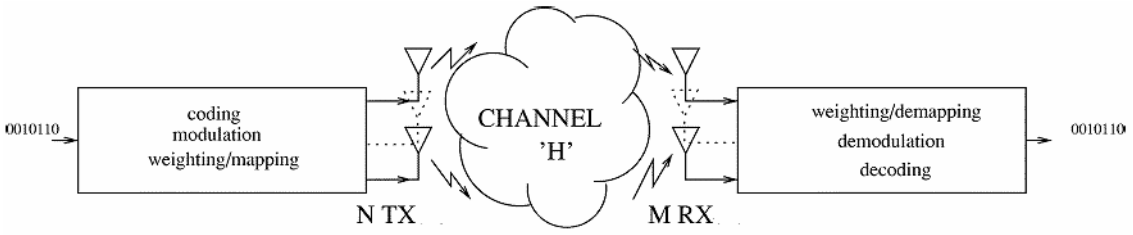

Figure 4.1: Diagram of MIMO wireless system (Gesbert et al., 2003).

MIMO system is used to increase the quality (to reduce Bit Error Rate or BER) of a wireless transmission, and to improve the data rate, i.e. to increase the channel capacity. Hence, two different transmission schemes over MIMO are observed: data rate maximization scheme and diversity maximization scheme.

Data rate maximization is obtained through *spatial multiplexing* of transmitted data when the independent signals are sent simultaneously using different transmitting antennas. The number of signals to be send is at most equal to the rank of the channel matrix $\mathbf{H}$. Figure 4.2 represents one example of spatial multiplexing in MIMO system.

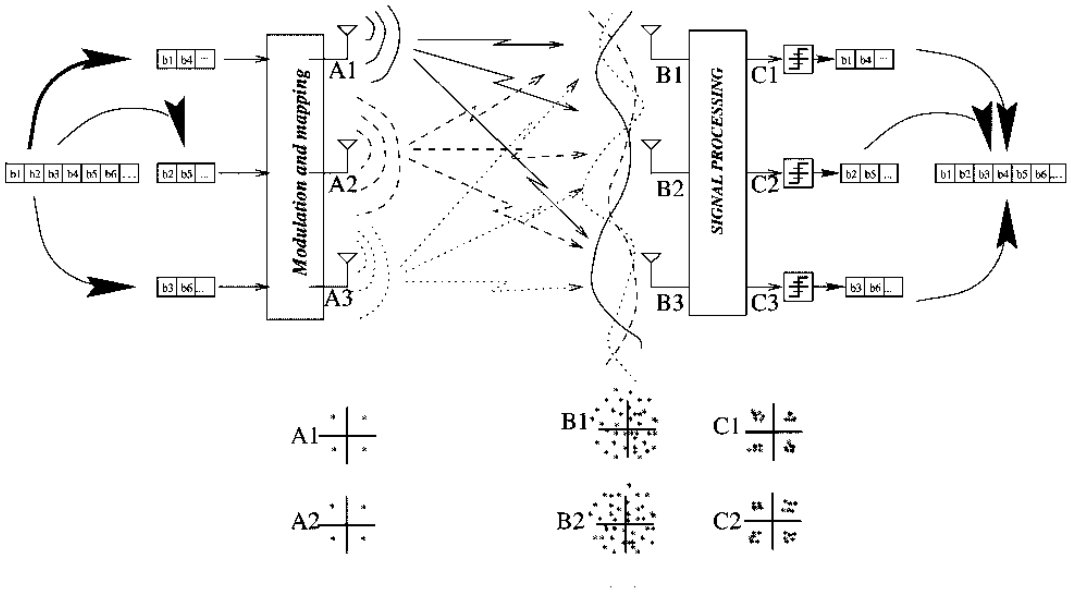

Figure 4.2: Spatial multiplexing scheme with 3 transmitting and 3 receiving antennas (Gesbert et al., 2003).

In Figure 4.2 high rate signal is factorized into three independent bit streams, which are transmitted at the same time through three transmitting antennas. Since the signals use the same frequency spectrum, they are totally mixed together. At the receiver side, the mixed channel matrix is determined using training symbols. Then three initial bit streams are separated and estimated. Separation of individual streams is possible due to presence of rich multipath, which creates essential differ-

ence in the channels received by each antenna. Finally, three bit streams are merged to yield the original high bit rate stream. In this example, the channel matrix $\mathbf{H}$ as 3×3 matrix has a full rank ($\text{rank}(\mathbf{H}) = 3$), that enables spatial multiplexing to get a spectrum efficiency gain of three. This result is explained in chapter 4.3 from the information theory point–of–view.

But commonly, the signals transmitted through different antennas should be encoded jointly against channel fading errors. In this case the diversity maximization scheme is used to improve the transmission quality. The set of schemes for adjuration and optimization joint encoding of multiple transmitting antennas is called *space–time coding*.

We should emphasize that improvement of transmission quality leads to reduction of the data rate. Since if we increase level of joint encoding between the transmitting antennas, then the amount of independence between the individual bit streams is decreased.

4.2 MIMO Channel Model

Let us consider a MIMO channel with M_t transmitting antennas and M_r receiving antennas. As before, let $h_{kl}(\tau; t)$ denote time–variant channel impulse response between k^{th}, $1 \leq k \leq M_r$, receiving antenna and l^{th}, $1 \leq l \leq M_t$, transmitting antenna. Likewise we showed in chapter 3.2, $h_{kl}(\tau; t)$ is the response at time t to unit impulse applied at time $t - \tau$. So, the compound MIMO channel response is given by $M_r \times M_t$ complex channel matrix $\mathbf{H}(\tau; t)$

$$\mathbf{H}(\tau; t) = \begin{bmatrix} h_{11}(\tau; t) & h_{12}(\tau; t) & \dots & h_{1M_t}(\tau; t) \\ h_{21}(\tau; t) & h_{22}(\tau; t) & \dots & h_{2M_t}(\tau; t) \\ \vdots & \vdots & \ddots & \vdots \\ h_{M_r1}(\tau; t) & h_{M_r2}(\tau; t) & \dots & h_{M_rM_t}(\tau; t) \end{bmatrix}$$

From chapter 3.2 we know that the received signal as an output of a linear system is represented by the convolution of the transmitted signal and the channel impulse response corrupted by additive noise. Similarly, the signal $y_k(t)$ received at k^{th} receiving antenna is defined as the sum of the convolutions of the transmitted signals $x_l(t)$ through all transmitting antennas corrupted by additive noise $n_k(t)$

$$y_k(t) \overset{(3.2.11)}{=} \sum_{l=1}^{M_t} h_{kl}(\tau; t) \star x_l(t) + n_k(t).$$

The application of the same input–output relation to all receiving antennas yields the general MIMO channel model

$$y(t) = \mathbf{H}(\tau; t) \star x(t) + n(t)$$

where $y(t)$ is $M_r \times 1$ received signal vector, $x(t)$ is $M_t \times 1$ transmitted signal vector, and $n(t)$ is $M_r \times 1$ AWGN vector.

For the sake of simplicity we suppress the time-variant nature of the channel and consider the narrowband, flat fading, MIMO channel. Thus, convolution effect in flat fading MIMO channel model reduces to multiplication

$$y = \mathbf{H}x + n \tag{4.2.1}$$

where received signal y linearly depends on the transmitted signal x through a flat fading channel impulse response $\mathbf{H}$.

In the signal model (4.2.1) the total average transmitted power is constrained to to P_T

$$P = E\{x^\dagger x\} = E\{\mathrm{tr}(xx^\dagger)\} \overset{(*)}{=} \mathrm{tr}E\{xx^\dagger\} \leq P_T \tag{4.2.2}$$

where superscript † stands for the Hermitian (conjugate transpose) transform, tr denotes trace of the matrix, and transition $(*)$ happens due to commutation of expectation and trace. AWGN noise vector n with covariance matrix

$$E\{nn^\dagger\} = \sigma_n^2 I_{M_r} \tag{4.2.3}$$

where I_{M_r} denotes a $M_r \times M_r$ identity matrix, affects different receiving antennas independently (Foschini, 1996; Telatar, 1995). Presented MIMO channel model is depicted in Figure 4.3.

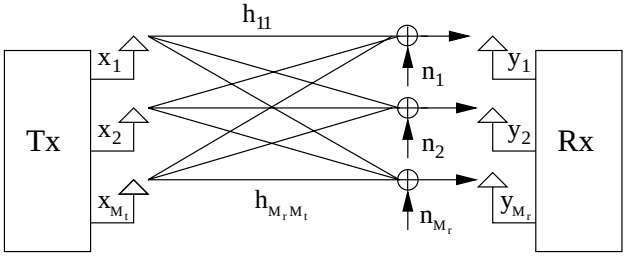

Figure 4.3: MIMO channel model with M_t transmitting and M_r receiving antennas.

In multipath surrounding environment the discrete flat fading MIMO channel has following impulse response

$$\mathbf{H}(\tau) = \sum_{l=1}^{L} \mathbf{H}_l \delta(\tau - \tau_l) \tag{4.2.4}$$

where $M_r \times M_t$ complex random matrix $\mathbf{H}_l$ represents l^{th}, $1 \leq l \leq L$, path. Each realization of matrix $\mathbf{H}_l$ specifies the environment.

Like in chapter 3.2, the application of the FT to the impulse response yields the MIMO channel frequency response (Paulraj et al., 2004)

$$\begin{aligned} \mathbf{H}(f) &\overset{(3.1.1)}{=} \int_{-\infty}^{\infty} \mathbf{H}(\tau) e^{-i2\pi f\tau} d\tau \\ &= \sum_{l=1}^{L} \mathbf{H}_l e^{-i2\pi f\tau_l}. \end{aligned} \tag{4.2.5}$$

According to (Paulraj et al., 2004) the elements of matrix $\mathbf{H}_l$ can be assumed to be independent identically distributed (i.i.d.) zero–mean complex Gaussian random variables with average power of one. The theorem in appendix A shows that the channel matrix elements have uniform phase and Rayleigh magnitude. Chosen channel matrix defines classical i.i.d. flat Rayleigh fading MIMO channel that accurately reflects non line–of–sight (NLOS) rich scattering environment with sufficient antenna spacing at both sides and with identically polarized antenna elements (Paulraj et al., 2004).

Although in this thesis we focus on i.i.d. Rayleigh fading MIMO channel, the channel matrix elements can also be chosen as complex Gaussian, but correlated random variable. Then the channel corresponds to spatial correlated Rayleigh fading environment. Rician fading environment can be modeled by summing Rayleigh NLOS component h_{kl} and constant LOS component h_{kl}^{LOS}.

We need to note that frequency–selective MIMO channel is constructed and is analyzed below with the help of OFDM technique.

4.3 Theoretical Capacity

Let us assume that the realization of channel $\mathbf{H}$ is known by the receiver.

The channel capacity with transmitted power constraint (4.2.2), when the channel transfer function H is constant and known, is generally defined as the maximum amount of a mutual information between transmitted and received signals (Cover and Thomas, 1991, p. 184)

$$\mathcal{C} = \max_{p(x):P\leq P_T} \mathcal{I}(x,y). \tag{4.3.6}$$

Hence, the mutual information should be maximized over transmitted signal x such that statistical distributions $p(x)$ satisfies the power constraint.

Let $\mathcal{H}_d(\cdot)$ denote differential entropy, i.e. entropy of a continuous random variable. Then the mutual information can be rewritten as (Cover and Thomas, 1991, p. 19)

$$\begin{aligned}
\mathcal{I}(x,y) &= \mathcal{H}_d(y) - \mathcal{H}_d(y|x) \\
&\overset{(4.2.1)}{=} \mathcal{H}_d(y) - \mathcal{H}_d(\mathbf{H}x + n|x) \\
&\overset{(*)}{=} \mathcal{H}_d(y) - \mathcal{H}_d(n|x) \\
&\overset{(**)}{=} \mathcal{H}_d(y) - \mathcal{H}_d(n)
\end{aligned} \tag{4.3.7}$$

where (*) transition is possible since channel $\mathbf{H}$ is perfectly known by the receiver. Thus, there is no uncertainty in $\mathbf{H}x$ conditioned to x. Since the noise n is assumed to be independent from x, the next (**) transition happens.

The channel capacity gives the theoretical upper limit on the data rate (bits/s/Hz) that is possible to transmit over the channel reliably. This means that with given BER requirement one can design the code that guarantees to transmit amount of information determined by the capacity.

As an example, capacity for single user single–input–single–output (SISO) system model

$$y = hx + n \quad y, h, x, n \in \mathbb{C}^1$$

for bandwidth of 1 Hz is represented as

$$\mathcal{C} = \log(1 + \frac{P_T}{\sigma_n^2}|h|^2)$$

where $P = P_T$ is assumed.

4.3.1 MIMO Capacity

Let derive the capacity formula for the Rayleigh fading Gaussian channel. The deducing needs a strong assumption. The input signals should be circularly symmetric.

Definition 4.3.1 *A Gaussian random vector $x \in \mathbb{C}^n$ is called circularly symmetric if for $\hat{x} = \begin{bmatrix} \mathfrak{Re}(x) \\ \mathfrak{Im}(x) \end{bmatrix}$ the covariance has the structure*

$$E\{(\hat{x} - E\{\hat{x}\})(\hat{x} - E\{\hat{x}\})^\dagger\} = \frac{1}{2}\begin{bmatrix} \mathfrak{Re}(Q) & -\mathfrak{Im}(Q) \\ \mathfrak{Im}(Q) & \mathfrak{Re}(Q) \end{bmatrix}$$

where Q is the covariance of vector x, $Q = cov(x)$.

The most important property of the circularly symmetric random vectors is in entropy maximization. This property is demonstrated in the following lemma.

Lemma 4.3.1 *Suppose the complex random vector $x \in \mathbb{C}^n$ is zero–mean and satisfies $E\{xx^\dagger\} = Q$. Then the entropy of x satisfies $\mathcal{H}(x) \leq \log\det(\pi e Q)$ with equality if and only if x is circularly symmetric complex Gaussian with*

$$E\{xx^\dagger\} = Q.$$

Proof. The proof can be found in (Telatar, 1995).

In this section let us assume that the channel is memoryless, i.e. for each use of the channel an independent realization of $\mathbf{H}$ is taken.

The mutual information between channel input vector x and channel output pair $(y, \mathbf{H})$ in the case of unfixed $\mathbf{H}$ is given by

$$\begin{aligned} \mathcal{I}(x, (y, \mathbf{H})) &= \mathcal{I}(x, \mathbf{H}) + \mathcal{I}(x, y|\mathbf{H}) \\ &\overset{(*)}{=} \mathcal{I}(x, y|\mathbf{H}) \\ &\overset{\text{def}}{=} E_{\mathbf{H}}\{\mathcal{I}(x, y|\mathbf{H} = H)\}. \end{aligned}$$

Since the channel is known to the receiver, (*) transition happens.

For calculating the capacity (4.3.6) we need to maximize $\mathcal{I}(x, y|\mathbf{H} = H)$. The definition of mutual information by means of differential entropy (4.3.7) yields the maximization only $\mathcal{H}_d(y|\mathbf{H} = H)$ since $\mathcal{H}_d(n|\mathbf{H} = H)$ is given and fixed. Recall that x satisfies power constraint (4.2.2) so as random vector $x - E\{x\}$. Then we can

restrict our attention to zero–mean random vector x with covariance $E\{xx^\dagger\} = Q$. Hence, vector $y = Hx + n$ is zero–mean random vector with covariance

$$\begin{aligned} E\{yy^\dagger\} &= E\{(Hx+n)(Hx+n)^\dagger\} \\ &\overset{(4.2.3)}{=} HQH^\dagger + \sigma_n^2 I_r \end{aligned}$$

under assumption that x and n are uncorrelated. By Lemma 4.3.1 vector y should be circularly symmetric complex Gaussian for maximizing the entropy. According to (Telatar, 1995) if x is circularly symmetric complex Gaussian, then y also possesses circularly symmetry, and mutual information is maximized.

$$\begin{aligned} \mathcal{I}(x,y) &= \log\det(\pi e(HQH^\dagger + \sigma_n^2 I_r)) - \log\det(\pi e\sigma_n^2 I_r) \\ &= \log\det\left(\frac{HQH^\dagger}{\sigma_n^2} + I_r\right) \\ &\overset{(*)}{=} \log\det\left(\frac{QH^\dagger H}{\sigma_n^2} + I_t\right) \end{aligned}$$

Following property of determinant $\det(AB + I_{AB}) = \det(BA + I_{BA})$ allows (*) transition.

Thus, in order to find the capacity we need to maximize

$$\mathcal{I}(x,(y,\mathbf{H})) = E_{\mathbf{H}}\left\{\log\det\left(I_t + \frac{Q}{\sigma_n^2}\mathbf{H}^\dagger\mathbf{H}\right)\right\} \tag{4.3.8}$$

or to find the correct power allocation. The capacity is different in the cases the channel is known and the channel is unknown to the transmitter since the power is allocated differently.

We need to emphasize that (4.3.8) capacity is the ergodic capacity, i.e. averaged over the channel realizations.

4.3.2 Independent Parallel Gaussian Channels

For complex channel matrix $\mathbf{H}$ always exists such a singular value decomposition

$$\mathbf{H} = U^\dagger \Sigma V \tag{4.3.9}$$

where U and V are unitary matrices of $M_r \times M_r$ and $M_t \times M_t$ size, respectively, Σ is a $M_r \times M_t$ diagonal matrix with $\min(M_t, M_r)$ positive singular values of the channel matrix located on the main diagonal. This yields that the channel correlation matrix may be eigenvalue decomposed as

$$\begin{aligned} \mathbf{H}^\dagger\mathbf{H} &= (U^\dagger\Sigma V)^\dagger U^\dagger\Sigma V \\ &= V^\dagger\Sigma^\dagger U U^\dagger \Sigma V \\ &= V^\dagger \Lambda V \end{aligned} \tag{4.3.10}$$

where $\Lambda = \Sigma^\dagger \Sigma$ is a diagonal matrix, which diagonal elements are eigenvalues λ_i, $1 \leq i \leq min(M_t, M_r)$, of the matrix $\mathbf{H}^\dagger \mathbf{H}$. Hence, applying eigenvalue decomposition (4.3.10) to the mutual information (4.3.8) we get

$$\begin{aligned}
\mathcal{I}(x,(y,\mathbf{H})) &= E_{\mathbf{H}} \left\{ \log\det\left(I_t + \frac{Q}{\sigma_n^2} V^\dagger \Lambda V \right) \right\} \\
&\overset{(*)}{=} E_{\mathbf{H}} \left\{ \log\det\left(I_t + \frac{\Lambda^{1/2} V Q V^\dagger \Lambda^{1/2}}{\sigma_n^2} \right) \right\} \qquad (VQV^\dagger := \widetilde{Q}) \\
&= E_{\mathbf{H}} \left\{ \log\det\left(I_t + \frac{\Lambda^{1/2} \widetilde{Q} \Lambda^{1/2}}{\sigma_n^2} \right) \right\} \\
&\leq E_{\mathbf{H}} \left\{ \log \prod_{i=1}^{\min(M_t,M_r)} \left(1 + \frac{\widetilde{Q}_{ii}}{\sigma_n^2} \lambda_i \right) \right\} \\
&= \sum_{i=1}^{\min(M_t,M_r)} E_{\mathbf{H}} \left\{ \log\left(1 + \frac{\widetilde{Q}_{ii}}{\sigma_n^2} \lambda_i \right) \right\}
\end{aligned} \tag{4.3.11}$$

with the equality when $\widetilde{Q}$ is diagonal matrix. Applying the property of determinant, $\det(AB) = \det(A)\det(B) = \det(BA)$, transition (*) happens. We maximize the mutual information over $\widetilde{Q}$ since unitary transformation does not change trace of the matrix, $tr\widetilde{Q} = trQ$. Furthermore, matrix Q is a non–negative define matrix since it is the covariance matrix. Hence, $\widetilde{Q}$ is also non–negative define matrix. Applying the following property of non–negative define matrices $\det A \leq \prod A_{ii}$, we finally obtain equation (4.3.11).

Let us consider the case of deterministic matrix H and rewrite the channel model as

$$y = HWx + n \quad E\{x_i x_j^*\} = \delta_{ij} \tag{4.3.12}$$

where $M_t \times M_t$ matrix W allocates the power to the M_t different input streams. Since objective of matrix W is maximization of received power, it is chosen in the following way

$$E\{tr(Wxx^\dagger W^\dagger)\} = tr(WW^\dagger) = trQ = P_T.$$

Substituting singular value decomposition (4.3.9) to MIMO channel model (4.3.12), we obtain

$$y = U^\dagger \Sigma V W x + n \quad \Leftrightarrow \quad Uy = \Sigma V W V^\dagger V x + Un \quad \Rightarrow \quad \tilde{y} = \Sigma \widetilde{Q}^{1/2} \tilde{x} + \tilde{n}$$

with the orthogonal transform $\tilde{y} = Uy$, $\tilde{x} = Vx$ and $\tilde{n} = Un$. Note, the orthogonal transform reserves the power constraint and does not change the distribution of noise. So, with diagonal matrices Σ, $\widetilde{Q}$ the signal model can be decomposed into independent parallel Gaussian channels

$$\begin{aligned}
&\tilde{y}_i = \sqrt{\widetilde{Q}_{ii}} \sqrt{\lambda_i} \tilde{x}_i + \tilde{n}_i \quad && 1 \leq i \leq \min(M_t, M_r) \\
&\tilde{y}_j = \tilde{n}_j && \min(M_t, M_r) \leq j \leq r
\end{aligned} \tag{4.3.13}$$

as shown in Figure 4.4.

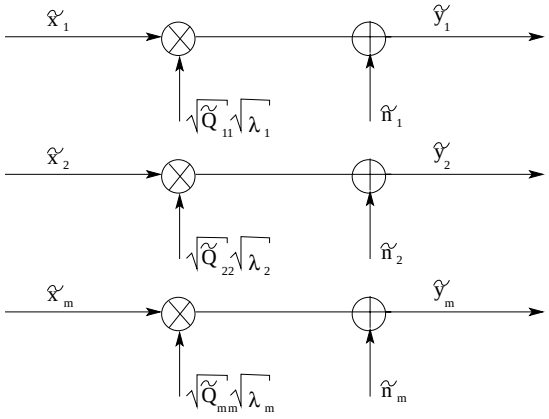

Figure 4.4: Independent parallel Gaussian channels.

Then the capacity can be expressed as

$$\begin{aligned} \mathcal{C} &= \max_{p(x):P\leq P_T} \mathcal{I}(x,y) \\ &\overset{(4.3.11)}{=} \sum_{i=1}^{\min(M_t,M_r)} \log\left(1+\frac{\widetilde{Q}_{ii}}{\sigma_n^2}\lambda_i\right). \end{aligned}$$

So, the capacity becomes a sum over $\min(M_t, M_r)$ parallel Gaussian channels and expresses the spectral efficiency of the i.i.d. flat Rayleigh fading MIMO channel. Linear growth of capacity with the number of eigen SISO channels illustrates the main advantage of MIMO systems.

This capacity can be achieved using the following procedure. First, we organize the data into vector stream $\tilde{x}$ with $\min(M_t, M_r)$ substreams, and we modulate them according to the power allocation $\widetilde{Q}^{1/2}$. After that we rotate the signal $\tilde{x}$ by multiplying $V^\dagger$. At the receiver we rotate received signal y by U to get $\min(M_t, M_r)$ parallel Gaussian substreams. Finally, we need to decode the substreams using the knowledge of channel eigenvalues.

4.3.3 Power Allocation

Let us consider optimal power allocation in open loop and closed loop MIMO systems. Systems without channel knowledge at the transmitter except the knowledge of the number of transmitting and receiving antennas and the fading statistics are called open loop systems whereas systems possessing the channel state information at the transmitter are called closed loop systems.

In open loop MIMO system the total available transmit power P_T due to optimization should be distributed among the transmitting antennas evenly

$$Q = \frac{P_T}{t} I_t \quad \Rightarrow \quad \widetilde{Q} = VQV^\dagger = \frac{P_T}{t} V I_t V^\dagger = \frac{P_T}{t} I_t.$$

With the help of mutual information (4.3.11) the capacity becomes a sum over $\min(M_t, M_r)$ independent parallel Gaussian SISO channels corresponding to the

eigenvalues λ_i, $1 \leq i \leq \min(M_t, M_r)$, of channel correlation matrix

$$\begin{aligned}\mathcal{C} &= \max_{trP=P_T} I(x,(y,\mathbf{H})) \\ &= \sum_{i=1}^{\min(M_t,M_r)} E\left\{\log\left(1+\frac{P_T}{t\sigma_n^2}\lambda_i\right)\right\}\end{aligned}$$

where the expectation is taken over the distribution of eigenvalues of $\mathbf{H}^\dagger\mathbf{H}$.

In closed loop MIMO systems with perfect channel state information at the transmitter side optimal power allocation to each eigenvalue channel should be done via water filling (Telatar, 1995)

$$\widetilde{Q}_{ii} = \left(\mu - \frac{\sigma_n^2}{\lambda_i}\right)^+ \quad 1 \leq i \leq M_t$$

where $\widetilde{Q} = VQV^\dagger$ is a diagonal matrix and a^+ means $\max(0,a)$. Power constraint $\sum_i \widetilde{Q}_{ii} = P$ should be valid to μ value. Note, some eigen channels corresponding to small eigenvalues may be allocated to $\widetilde{Q}_{ii} = 0$ passing through water filling.

So, the capacity becomes a sum over $M \leq \min(M_t, M_r)$ parallel channels with different power locations

$$\begin{aligned}\mathcal{C} &= \max_{trP=P_T} I(x,(y,\mathbf{H})) \\ &= \sum_{i=1}^{M} E\left\{\log\left(1+\frac{\widetilde{Q}_{ii}}{t\sigma_n^2}\lambda_i\right)\right\} \\ &= \sum_{i=1}^{M} E\left\{\log\left(\frac{\lambda_i}{M}\sum_{j=1}^{M}\lambda_j^{-1} + \frac{P}{M\sigma_n^2}\lambda_i\right)\right\}.\end{aligned}$$

4.3.4 Non–ergodic Capacity

Let us consider non–ergodic channel where $\mathbf{H}$ is chosen randomly but fixed once it is realized. Then the maximum mutual information is not always equal to the channel capacity since it is not always achievable. Alternative frequently used measure of the capacity is *outage capacity*. It is a trade off between outage probability and supportable rate. It is defined as a random variable associated with outage probability q

$$P_{\text{out}}(C_{\text{outage}}) = Prob\{C \leq C_{\text{outage}}\} = q$$

where q is defined as

$$q = \inf_{Q:Q\geq 0, tr(Q)\leq P} Prob\{\log\det(I_r + \mathbf{H}Q\mathbf{H}^\dagger) \leq C_{\text{outage}}\}.$$

Chapter 5

Orthogonal Frequency Division Multiplexing

Orthogonal Frequency Division Multiplexing (OFDM) is a modulation technique that can be compounded with MIMO to increase the diversity gain and/or to improve capacity on time–variant and frequency–selective channels.

OFDM transforms a frequency–selective wideband channel into a set of flat narrowband channels that are orthogonal in frequency domain. OFDM transformation is realized in discrete domain by means of the DFT discussed in chapter 3.1.2. The Fast Fourier Transform (FFT) described in appendix B is an efficient method of the DFT implementation.

In this chapter we present the main principles of discrete time OFDM modulation. Besides, we show how OFDM modulations turns a frequency–selective MIMO channel into a set of parallel flat MIMO channel examined in chapter 4.

5.1 OFDM Principles

For better understanding the main idea of OFDM transmission, let us review the structure of frequency–selective channel explained in chapter 3.2.

According to channel model (3.2.6) received signal envelope in time domain can be expressed by convolution of transmitted signal envelope with the channel impulse response. The channel becomes frequency–selective if its coherence bandwidth is smaller than the bandwidth occupied by the transmitted signal (Rappaport, 2002). So, different frequency components of the transmitted signal are attenuated differently. That is why complex procedure should be applied to retrieve transmitted signal from channel model equation (3.2.6). The transmission scheme based on OFDM technique simplifies this problem. Using OFDM the convolution in time domain is transformed into multiplication in frequency domain according to channel model conversion (3.2.10).

OFDM technique is usually used to improve the capacity. As we know from chapter 3.3 the coherence bandwidth B_c measures a frequency band over which fading is highly correlated. The coherence bandwidth can be expressed by means of

maximum excess delay T_m (Sklar, 1997)

$$B_c \cong \frac{1}{T_m}.$$

So, we can conclude that channel becomes frequency–selective if maximum axcess delay caused by multipath propagation is larger than time duration of transmitted signal. In this case delayed path of the previous signal interferes with the next direct signal, and it causes inter–symbol interference and difficulties in retrieving of the received signal. For avoiding inter–symbol interference the time for each transmission shouldn't be shorter than maximum axcess delay. Since maximum axcess delay is constant in one environment the coherence bandwidth also remains constant. That yields the limitation in the transmitted data rate as we showed by equation of rate limit (3.3.14). OFDM escapes this limitation by transmitting the high data rate through several low data rate channels simultaneously.

OFDM basic principles may be described through three main points: high data rate stream is split into N parallel low data rate streams, the whole channel bandwidth is split into N orthogonal subcarriers with equal bandwidth and each low data rate stream is transmitted through each subcarrier.

The separation of the available bandwidth into subcarriers is essential. On the one hand, the width of each subcarrier should be narrow enough for flat fading. But on the other hand, the width of each subcarrier should be wide enough to enable transmission given data rate (3.3.14). Furthermore, for efficient use of total bandwidth the separation should be tight, but at the same time the inter–subcarrier interference should be avoided. All these features are supplied with the orthogonal separation. The property of orthogonality holds

$$\int_{-\infty}^{\infty} f(t)g^*(t)dt = 0 \quad \forall t \ : \ f(t) \neq g(t) \ \ f, g \in \mathbb{C}^1$$

where superscript * stands for function complex conjugate.

Let us obtain required orthogonal frequency spacing. Transmitting the bandpass signal (2.1.4) with complex envelope $s_z(t) = e^{i2\pi f_m t}$ through subcarrier m and $s_z(t) = e^{i2\pi f_l t}$ through subcarrier l during signal interval T we have

$$\int_0^T e^{i2\pi f_m t} e^{-i2\pi f_l t} dt = 0 \Longleftrightarrow f_m - f_l = \frac{m-l}{T}.$$

Thus, subcarriers are separated from each other with $\frac{1}{T}$ frequency interval. Such spacing allows to have orthogonal behavior in frequency domain.

Let us focus on OFDM model presented in Figure 5.1. Here, we consider noiseless transmission case for simplicity.

The transmitter converts the incoming high data rate stream from serial stream into N parallel substreams. Thus, the data is transmitted by block OFDM symbols of size N. Each k^{th} block is described as

$$s(k) = [s_1(k), s_2(k), \ldots, s_N(k)]$$

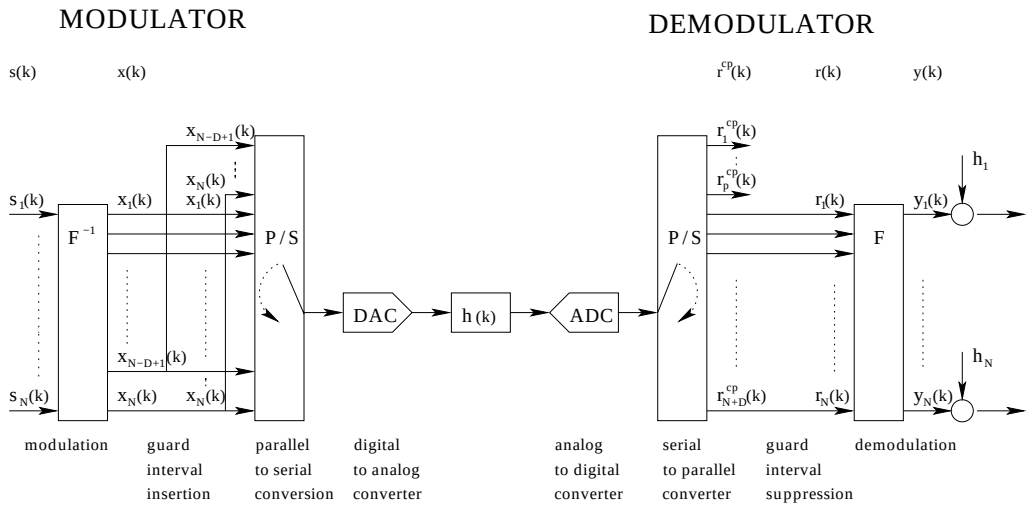

Figure 5.1: OFDM transceiver model (Debbah, 2002).

where $s_j(k),\ 1 \leq j \leq N$, denotes one symbol in k^{th} block for each subcarrier. Then the block OFDM symbol is transformed to time domain block vector

$$x(k) = [x_1(k), x_2(k), \ldots, x_N(k)]$$

by the IFFT matrix F_N^{-1}. After that at the beginning of the block vector $x(k)$ a guard interval with length of D is inserted. The guard interval consists of D last samples of the block vector $x(k)$. Thus, we get OFDM signal

$$x(k) = [x_{N-D+1}(k), \ldots, x_N(k), x_1(k), x_2(k), \ldots, x_N(k)].$$

The guard interval is called the cyclic prefix. It is appended between each block in order to transform the multipath linear convolution into a circular convolution (Debbah, 2002). A circular convolution is essential for OFDM since it can be diagonalized in the Fourier basis at the receiver. Therefore, the block OFDM symbol $s(k)$ is turned to be transmitted over N parallel flat fading channels.

Usually the length D of cyclic prefix is smaller than N, commonly, $D = \frac{N}{4}$, and greater than maximum axcess delay for avoiding inter–symbol interference. The cyclic prefix insertion adds redundant information, and the redundancy factor is equal to $\frac{N}{N+D}$. To avoid inefficient transmission the redundancy factor should be close to 1. So, N should be chosen much greater that D. But the FFT complexity grows slightly faster than linear with N. Therefore, N should be chosen depending on the channel and the an accepted complexity cost.

After cyclic prefix insertion Parallel to Serial and Digital to Analog conversions are carried out, and the OFDM signal is transmitted through a frequency–selective channel.

At the receiver side inverse Analog to Digital and Serial to Parallel conversions are implemented. The received block symbol

$$r^{CP}(k) = [r_1^{CP}(k), r_2^{CP}(k), \ldots, r_{N+D}^{CP}(k)]$$

in time domain is reduced to r(k)

$$r(k) = [r_1(k), r_2(k), \ldots, r_N(k)]$$

by deleting first D samples due to suppress the inter–block interference. The FFT processing at the receiver by matrix F_N transforms $r(k)$ in time domain into vector block $y(k)$ in frequency domain.

$$y(k) = [y_1(k), y_2(k), \ldots, y_N(k)]$$

The application of the FFT yields diagonalization of the channel. Hence, the block OFDM symbol $s(k)$ is turned to be transmitted over N parallel flat fading channels (Debbah, 2002)

$$\begin{bmatrix} y_1(k) \\ \vdots \\ \vdots \\ \vdots \\ y_N(k) \end{bmatrix} = \begin{bmatrix} h_1 & 0 & \ldots & \ldots & \ldots & 0 \\ 0 & h_2 & 0 & \ldots & \ldots & \ldots \\ \vdots & 0 & \ddots & 0 & \ldots & \ldots \\ \vdots & \ldots & \ldots & \ddots & \ldots & \ldots \\ \vdots & \ldots & \ldots & \ldots & \ddots & \ldots \\ \vdots & \ldots & \ldots & \ldots & \ldots & h_N \end{bmatrix} \begin{bmatrix} s_1(k) \\ \vdots \\ \vdots \\ \vdots \\ s_N(k) \end{bmatrix}$$

with a complex frequency attenuation $h_j = H(e^{i2\pi(j-1)/N})$, $1 \leq j \leq n$, where $H(f;t) = H(f)$ is a channel frequency response (3.2.9).

In the case of noise presence, Gaussian noise vector

$$n(k) = [n_1(k), n_2(k), \ldots, n_N(k)]$$

corrupts the transmission. At the receiver side noise is orthogonal transformed into frequency domain by the FFT matrix multiplication

$$\tilde{n}(k) = \begin{bmatrix} \tilde{n}_1(k) \\ \vdots \\ \vdots \\ \tilde{n}_N(k) \end{bmatrix} = F_N \begin{bmatrix} n_1(k) \\ \vdots \\ \vdots \\ n_N(k) \end{bmatrix}.$$

Since this transformation does not change the statistics, block noise vector $\tilde{n}(k)$ remains white Gaussian with the same variance. Therefore, OFDM model in frequency domain in the case of noisy transmission is described as a system of N equation (Debbah, 2002)

$$y_j(k) = h_j(k)s_j(k) + \tilde{n}_j(k) \quad 1 \leq j \leq N \tag{5.1.1}$$

where each symbol $y_j(k)$ received by j^{th} subcarrier linearly depends on transmitted symbol $s_j(k)$. Extracting of each $s_j(k)$ symbol is possible through multiplying each $y_j(k)$ by $h_j^*(k)$.

In this section we showed how frequency–selective channel can be converted to the set of flat orthogonal channels using OFDM technique. The orthogonality

of subcarriers allows to use efficiently the total bandwidth. The conversion from frequency–selective channel let us to improve frequency diversity, for example, by transmitting signals with the same information through different subcarriers. Since different fading replicas can be received, a more reliable received information can be performed. On the other hand, using OFDM the data rate can be increased instead of diversity gain achievement.

5.2 MIMO–OFDM System

So far we discussed flat fading MIMO channels. But modern wideband communication systems need to deal with frequency–selective channel. The application of OFDM modulation allows frequency–selective MIMO channel to be converted into a set of parallel flat fading MIMO channel. The block diagram of MIMO–OFDM system with M_t transmitting antennas, M_r receiving antennas and N subcarriers is depicted in Figure 5.2.

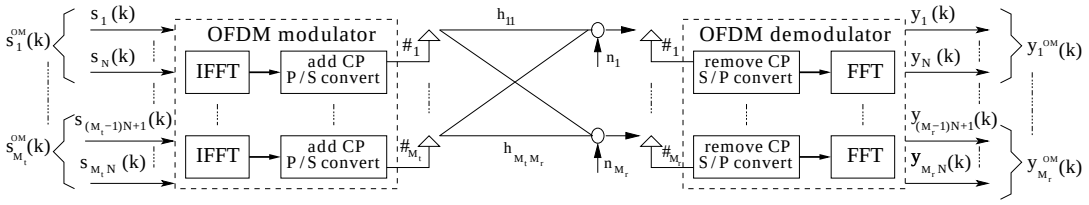

Figure 5.2: MIMO system combined with OFDM modulation.

The incoming high data rate is split into $M_t \times N$ substreams. So, set of M_t k^{th} block OFDM symbols is organized.

$$\begin{aligned} s_1^{OM}(k) &= [s_1(k), s_2(k), \ldots, s_N(k)], \\ &\vdots \\ s_{M_t}^{OM}(k) &= [s_{(M_t-1)N+1}(k), s_{(M_t-1)N+2}(k), \ldots, s_{M_tN}(k)]. \end{aligned}$$

Each block OFDM symbol is transformed to time domain vector by the IFFT and is inserted with the cyclic prefix. Then the parallel to serial conversation is executed, and M_t OFDM signals are transmitted through M_t different antennas. At the receiver side signals are converted from serial to parallel and the cyclic prefix is removed. Using the FFT signals are transformed to frequency domain vector blocks

$$\begin{aligned} y_1^{OM}(k) &= [y_1(k), y_2(k), \ldots, y_N(k)], \\ &\vdots \\ y_{M_r}^{OM}(k) &= [y_{(M_r-1)N+1}(k), y_{(M_r-1)N+2}(k), \ldots, y_{M_rN}(k)]. \end{aligned}$$

Let us superscript ^{T} stand for vector transpose. According to OFDM channel model (5.1.1) frequency-selective MIMO channel is converted into the set of N parallel flat MIMO channels in frequency domain

$$y_j^{OM}(k) = \mathbf{H}_j s_j^{OM}(k) + \tilde{n}_j(k) \qquad 1 \leq j \leq N \tag{5.2.2}$$

where $y_j^{OM}(k) = [y_j(k), y_{N+j}(k), \ldots, y_{(M_r-1)N+j}(k)]^T$ is $M_r \times 1$ signal vector received by j^{th} subcarrier, $s_j^{OM}(k) = [s_j(k), s_{N+j}(k), \ldots, s_{(M_t-1)N+j}(k)]^T$ is $M_t \times 1$ signal vector transmitted through j^{th} subcarrier, $\mathbf{H}_j = \sum_{l=1}^{L} \mathbf{H}_l e^{-i2\pi(j-1)/N\tau_l}$ represents $M_r \times M_t$ flat frequency MIMO channel response (4.2.5), $\tilde{n}_j(k)$ is $M_r \times 1$ complex Gaussian noise uncorrelated across subcarriers (4.2.3).

The objective of combining OFDM modulation with MIMO system is neglecting of frequency–selectivity inside MIMO channel. Moreover, OFDM modulation brings the advantages illustrated in the previous section such as the diversity gain or the spectral efficiency. Thus, OFDM technique applied to MIMO system is quite promising candidate for future wireless communications.

Chapter 6

Effective SNIR Mapping

In the present time study of a cellular system performance is implemented by simulations due to complexity of the whole cellular system. Furthermore, simulations are carried out by link level simulator and system level simulator. Link level simulations are solely used to investigate physical layer performance while system level simulations study higher layer processing (Alexiou et al., 2005). Link level and system level simulators are combined through *link–to–system* (L2S) *interface*.

In this chapter we take an overall look at a quality model based on signal to noise ratio. The quality model describes the process of precise estimation the results obtained with simulators. Particularly, the quality model specifies L2S interface methods. In this chapter we represent two advanced L2S interface approaches and suggest novel link–to–system interface for MIMO systems.

6.1 Quality Model

Link level simulator simulates a continuous transmission between BS and MS involving different specific characteristics: coding scheme, modulation scheme, spatial pre- and post–processing, parameter estimation (synchronization, channel estimation, automatic gain control), small–scale fading. One objective of the link level simulator is producing the results for the system simulator. In general, two kinds of results are required: estimating the link quality from BER (burst wise) to FER (frame wise) or PER (packet wise) and channel quality measures. One of the important measures of channel quality under specific system parameters is *signal to interferer and noise ratio* (SINR) described in the next section. Estimating the link quality is done by quality model.

Quality model describes a procedure of accurately estimate the link performance for each user of known block length, physical transmission mode, scheduling decision, resource allocation, propagation conditions and inter-cell interference (Alexiou et al., 2005).

Figure 6.1 represents possible realization of quality model. First, resources are allocated between users, power levels are determined for each user. Then individual channels including fading, shadowing, path loss, interference are computed. From these results a set of quality measures $\{\theta_1, \theta_2, \ldots, \theta_N\}$ is obtained for all resource elements. Since number of resource elements may be large, multidimensional mapping

to PER is difficult. Therefore, accurate compression into small number of quality value parameters should be done. Typically, one or two compressed values $\{\Theta_1, \Theta_2\}$ are required for mapping to PER. Mapping itself is realized through look–up tables (LUT), i.e. tabulated BER function of SINR, or analytical equations, which depend on applied coding, interleaving, modulation scheme and packet length.

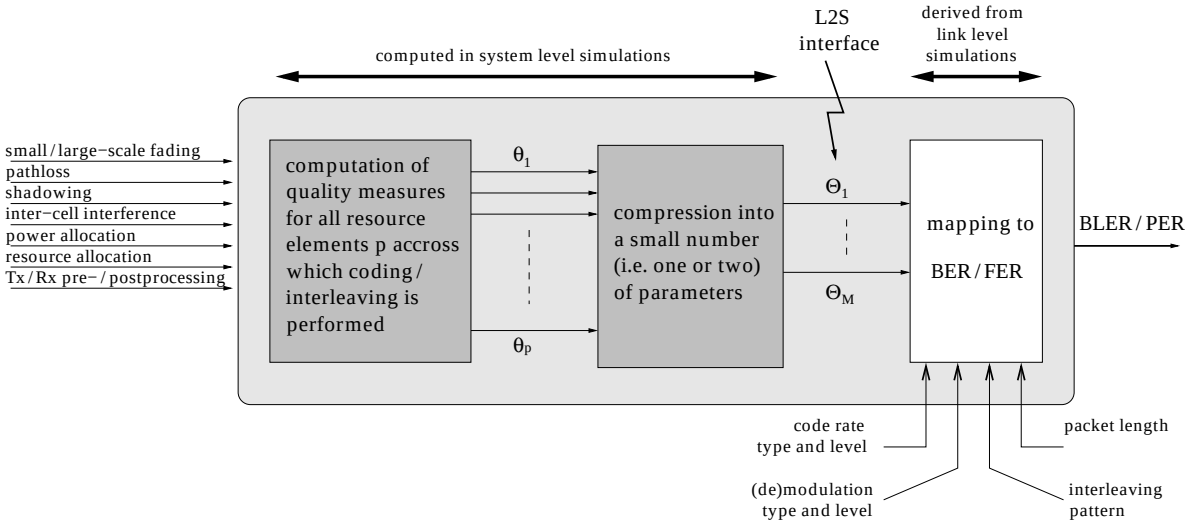

Figure 6.1: Potential realization of a link quality model (Alexiou et al., 2005).

Let us recall that different bits transmitted in various OFDM symbols through various OFDM subcarriers may have different quality. Thus, in multi–state channel number of frequency resource elements (e.g., subcarriers or set of subcarriers), time resource elements (e.g., OFDM symbols) and space resource elements (e.g., layers for MIMO vector) is too large to be used directly. So, key issue for accurate estimation of link performance is in accurate compression. Such compression reduces instantaneous channel state, appeared as instantaneous quality measures of all resource elements $\{\theta_1, \theta_2, \ldots, \theta_N\}$, to one or two scalar values, $\{\Theta_1, \Theta_2\}$. These values are later used to find an estimated BLER of the specific channel state. According to (Alexiou et al., 2005) compression may be done through the *effective SNR mapping* (ESM). In this chapter we represent two variants of novel ESM function for SISO. Also, we suggest our model of the ESM function for MIMO.

6.2 Link Level Model Measurement

In the previous section we have mentioned that the quality of transmission between BS and MS in link level is measured by means of SINRs. In the case of multi–state channel SINRs vary from one OFDM subcarrier to another. SINR sample in j^{th} subcarrier is simply calculated as

$$SINR_j = \frac{C_j}{I_j + N_0} \tag{6.2.1}$$

where C_j is received signal power in j^{th} subcarrier, I_j is interference power in j^{th} subcarrier, and N_0 is background noise power.

SINR values may also be calculated in link level across frequency blocks, i.e. set of subcarriers,

$$SINR_j = \frac{C_j}{\sum_{i=1,\, i\neq j}^{N} I_{ji} + N_0} \tag{6.2.2}$$

where C_j is received signal power in j^{th} frequency block, N is the number of OFDM subcarriers or OFDM size, I_{ji} is i^{th} interference power in j^{th} frequency block, and N_0 is background noise power.

6.3 Basic Principles of the ESM

In section 6.1 we learned that the ESM is a compression function used as advanced L2S approach in quality model. The ESM maps an instantaneous channel state carried out by set of SINRs across OFDM channel $\{SINR_j\}$ into an instantaneous scalar value, an effective signal to noise ration $SINR_{eff}$, as (Alexiou et al., 2005, p. 94)

$$SINR_{eff} = I^{-1}\left(\frac{1}{N}\sum_{j=1}^{N} I\left(SINR_j\right)\right). \tag{6.3.3}$$

Here, function $I(\cdot)$ is referred to "information measure" function, and $I^{-1}(\cdot)$ is its inverse. The number N is a total number of resource elements for quality measurement. Particularly, N may be the amount of OFDM subcarriers.

The effective SINR value is later mapped on user quality in terms of BLER for AWGN channel (3.2.13).

So, the ESM model follows three main steps:

1. In each subcarrier SINR sample is calculated with the help of equation (6.2.1).

2. The effective SNR under specific model parameters is calculated from the set of SINRs according to the ESM compression function (6.3.3).

3. The effective SNR is mapped to a single BLER via correct look–up table for AWGN channel. Look–up tables are constructed empirically in link level taking channel characteristics and used coding schemes into account.

The accuracy of the ESM approach can be validated by the following approximate equivalence

$$BLER\left(SINR_j\right) \approx BLER\left(SINR_{eff}\right) \tag{6.3.4}$$

where $BLER\left(SINR_j\right)$ is the actual (simulated) BLER for instantaneous channel state $\{SINR_p\}$ and $BLER\left(SINR_{eff}\right)$ is BLER value for AWGN channel. We should emphasize that the accuracy of each channel realization has to be checked.

Equalization of BLER values (6.3.4) for all instantaneous channel states lets the ESM approach to be used not only for AWGN channel but also for other types of channel in system level simulations.

We need to highlight that one of the main advantage of the ESM approach is the fact that it relies on AWGN look–up table, whereas the previous L2S interface methods build on various look–up tables for different channel realizations.

6.3.1 The Exponential ESM for SISO

One of the most–used form of the ESM function is the *exponential effective SNIR mapping* (EESM). The exponential compression function of L2S interface is applied only to SISO system with one transmitter and one receiver.

From the previous section we know that the ESM (6.3.3) utilizes the information measure function. For the EESM approach this function is defined as exponent (Alexiou et al., 2005, p. 94). Substituting exponent and logarithm as its inverse to the ESM mapping (6.3.3) we get the EESM function

$$SINR_{eff} \overset{(6.3.3)}{=} -\beta \ln\left(\frac{1}{N}\sum_{j=1}^{N} e^{-\frac{SINR_j}{\beta}}\right) \tag{6.3.5}$$

where β is a scaling factor dependent on modulation and coding rate. For computational efficiency, the number of OFDM subcarriers N should be equal to the amount of useful subcarriers.

Figure 6.2 illustrates the EESM approach used together with link level results for different modulation/coding schemes (MCS) on some specific channel. For each MCS scheme the specific relation between the effective SINR and BLER is obtained.

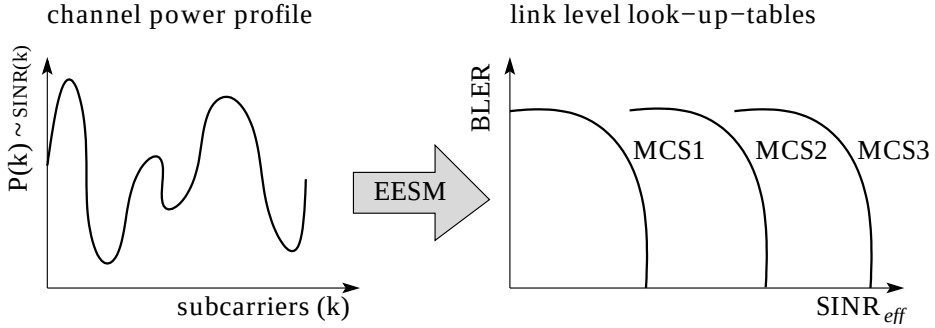

Figure 6.2: Exponential Effective SINR Mapping.

The scaling parameter β in the EESM approach is used for minimizing mismatch between the actual (simulated) BLER and BLER estimated through the EESM approach. The concrete values of parameter β for different MCSs are obtained by training specific model in link level simulator as described in (Alexiou et al., 2005). As an example, parameter values specified in (3rd Generation Partnership Project, 03) are given in Table 6.1.

The validation of the EESM equalization in link level is presented in (Alexiou et al., 2005) where the EESM accuracy for the OFDM performance is carefully studied. Alexiou et al. (2005) claim that good accuracy of the EESM for BPSK and QPSK modulation can be provided through proper MCS scaling parameter.

Table 6.1: Parameter set for β determined in 3GPP.

Modulation	Code Rate	Information Bit Payload	β value
QPSK	1/3	4800	1.49
QPSK	1/2	7200	1.57
QPSK	2/3	9600	1.69
QPSK	3/4	10800	1.69
QPSK	4/5	11520	1.65
16QAM	1/2	14400	4.56
16QAM	2/3	19200	6.42
16QAM	3/4	21601	7.33
16QAM	4/5	23041	7.68

They conclude that the EESM for 16QAM modulation is less accurate, but still can provide optimistic estimate of OFDM link level performance.

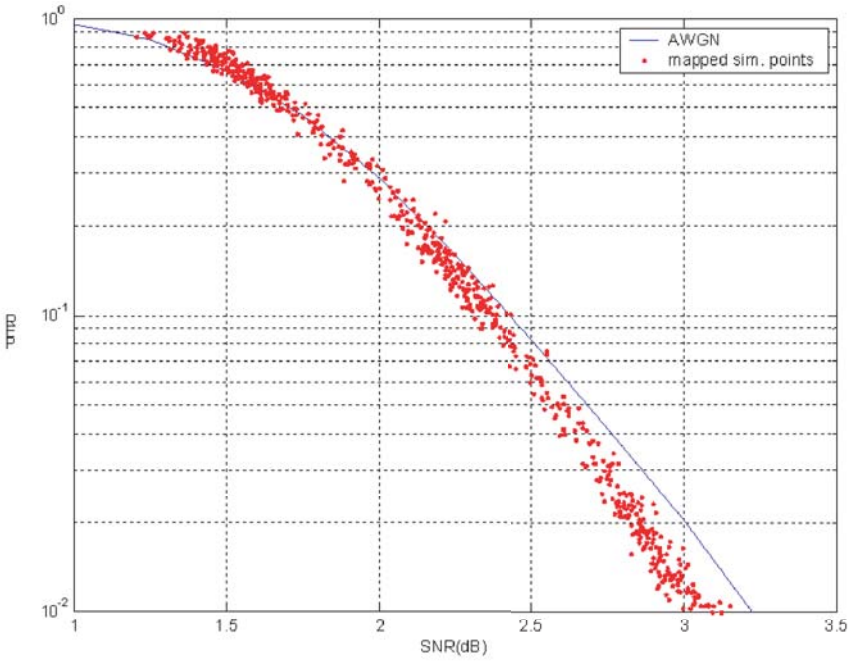

Figure 6.3: Simulated SINRs for the EESM vs. PER, $\beta = 1.72$, QPSK$\frac{1}{2}$ (Alexiou et al., 2005).

As an example, validation results for the exponential ESM with scaling factor $\beta = 1.72$, QPSK modulation and code rate 1/2 are shown in Figure 6.3. PER samples of AWGN channel are drawn with solid line, other dots are simulation results for different channel realizations. Choice of appropriate scaling parameter allows simulated PER for different channels to be close to the AWGN PER.

In spite of the fact that proper chosen scaling factor brings general advantages of the ESM we need to highlight one disadvantage of the EESM mapping. Since

the EESM utilizes the exponent function the complexity of the EESM approach increases with the number of SINRs taken into account. Thus, minimum number of OFDM subcarriers should be specified.

6.3.2 The Mutual Information ESM for SISO

Let us now consider the mutual information as a candidate of "measured information" in advanced L2S interface approach presented in (Alexiou et al., 2005). The application of the proposed "measured information" function to the the ESM mapping (6.3.3) yields the *mutual information ESM mapping* (MI–ESM) function given by (Alexiou et al., 2005, p. 95)

$$SINR_{eff} = \beta \cdot I_{m_{\text{ref}}}^{-1}\left(\frac{1}{N}\sum_{j=1}^{N} I_{m_j}\left(\frac{SINR_j}{\beta}\right)\right) \tag{6.3.6}$$

where m_j is a number of bits per symbol j, m_{ref} is an average number of transmitted bits per data symbols, i.e. $m_{\text{ref}} = \frac{1}{N}\sum_{j=1}^{N} m_j$, I_{m_j} is the mutual information function of the applied modulation alphabet of size 2^{m_j} at the j^{th} data symbol and I^{-1} its inverse. As for the EESM approach, β is a MCS parameter that must be estimated in link level for each modulation coding scheme. The OFDM size N may be reduced to a number of useful subcarriers since some subcarriers are not used due to bad fading conditions.

For ability to use the MI–ESM approach we need to specify the mutual information function realization. One possible choice is bit–interleaved coded modulation (BICM) capacity defined as (Alexiou et al., 2005, p. 95)

$$I_{m_j}(x) = m_j - E_Y\left(\frac{1}{2^{m_j}}\sum_{i=1}^{m_j}\sum_{b=0}^{1}\sum_{z\in X_b^i}\log\frac{\sum_{\hat{x}\in X} exp(-|Y-\sqrt{x}(\hat{x}-z)|^2)}{\sum_{\tilde{x}\in X_b^i} exp(-|Y-\sqrt{x}(\tilde{x}-z)|^2)}\right) \tag{6.3.7}$$

where X is the set of 2^{m_j} symbols, X_b^i is the set of symbols for which bit i equals to b, Y is zero mean unit variance complex Gaussian variable. Figure 6.4 illustrates mutual information for three various modulation alphabets.

The main advantage of the MI–ESM is in its accurate performance for mixed modulation since mutual information function takes modulation alphabet into account (Alexiou et al., 2005).

One possible modification of the MI–ESM approach can be proposed since conversion into mutual information domain may bring implementation advantage. We can calculate mutual information for each $\frac{SINR_j}{\beta}$ value and then sum up these numbers to the total mutual information $I_{\text{tot}} = \frac{1}{N}\sum_{j=1}^{N} I_{m_j}\left(\frac{SINR_j}{\beta}\right)$. Then the total mutual information is mapped directly to BLER. Operating in mutual information domain let us avoid inverse mapping.

Likewise in the EESM, the scaling factor β in the MI–ESM approach is used for appropriate equalization between actual BLER values and BLER estimated through the MI–ESM. The validation of the MI–ESM and general conclusion about the MI–ESM accuracy for the OFDM channel performance in sense of precise matching to

PER samples of AWGN channel realization are given in (Alexiou et al., 2005). Validation results presented in (Alexiou et al., 2005) indicate a good accuracy of the MI–ESM for BPSK and QPSK modulation using proper MCS scaling parameter. Alexiou et al. (2005) show that for 16QAM and 64QAM modulations the MI–ESM is less accurate but still can provide optimistic estimate of OFDM link level performance.

As as example, in Figure 6.5 validation results for the mutual information ESM with scaling factor $\beta = 1.16$, QPSK modulation and code rate 1/2 are presented. PER samples of AWGN channel are drawn with solid line, other dots are simulation results for different channel realizations. Proper selection of scaling parameter shifts simulated PER for different channels to be close to the AWGN PER.

6.4 Proposal of the ESM for MIMO

For estimation of the multi–state SISO channel performance the ESM approach is adapted through the EESM and the MI–ESM compression functions described above. But 4G wireless system requires to support MIMO channel model. So, the estimation of MIMO link performance for each user is needed. In this section we suggest the ESM approach adaptation for estimation of the uncorrelated Rayleigh fading MIMO channel performance.

From chapter 6.3 we know that the main advantage of the ESM approach is its universality for different type of channels due to its equalization (6.3.4) and β scaling parameter optimization. Since the scaling factor is used to avoid large difference between different subcarriers and channels, the same parameter value is applied for all subcarriers regardless of coding and modulation. The same properties of the ESM compression function are desirable to have for estimation MIMO channel quality where frequency resource elements and space resource elements must be taken into account.

Let us recall the MIMO–OFDM system with M_t transmitting antennas, M_r receiving antennas and N OFDM subcarriers described in details in chapters 4 and 5.2. From chapter 5.2 we know that in frequency domain the application of OFDM modulation yields the conversion frequency–selective MIMO channel into the set of N parallel flat fading MIMO channels. Moreover, in chapter 4.3.2 we demonstrated that flat Rayleigh fading MIMO channel can be decomposed into $\min(M_t, M_r)$ independent parallel Gaussian channels. Thus, in multi–state MIMO–OFDM channel $N \cdot \min(M_t, M_r)$ resource elements should be accurate compressed to one effective SINR value through the ESM compression function.

The ESM approach (6.3.3) maps sequence of varying SINRs to a single SINR sample that is strong correlated with the actual BLER value. Since in frequency domain frequency–selective MIMO is transformed into N frequency–flat fading MIMO channel, we can map N frequency varying quality measures $\{QM_j\}$ of flat MIMO channel to one effective SINR value through the MI–ESM or the EESM compression function using β scaling parameter. Thus, we need only to specify the quality measure of flat Rayleigh fading MIMO channel.

In chapter 5.2 we showed that each subcarrier in frequency domain is character-

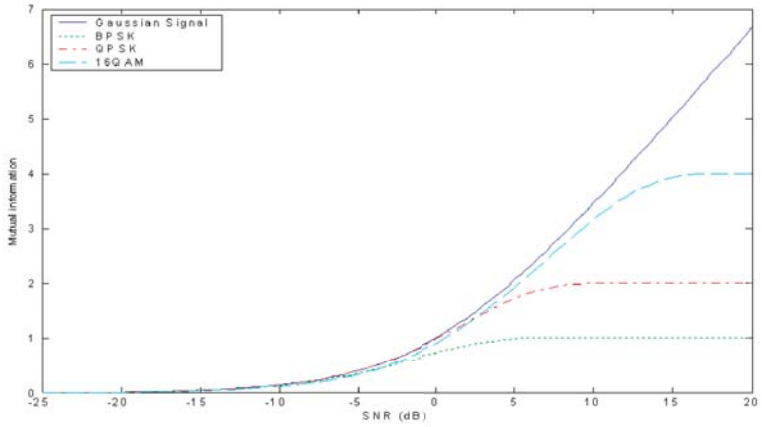

Figure 6.4: BICM mutual information for different modulation alphabets (Alexiou et al., 2005).

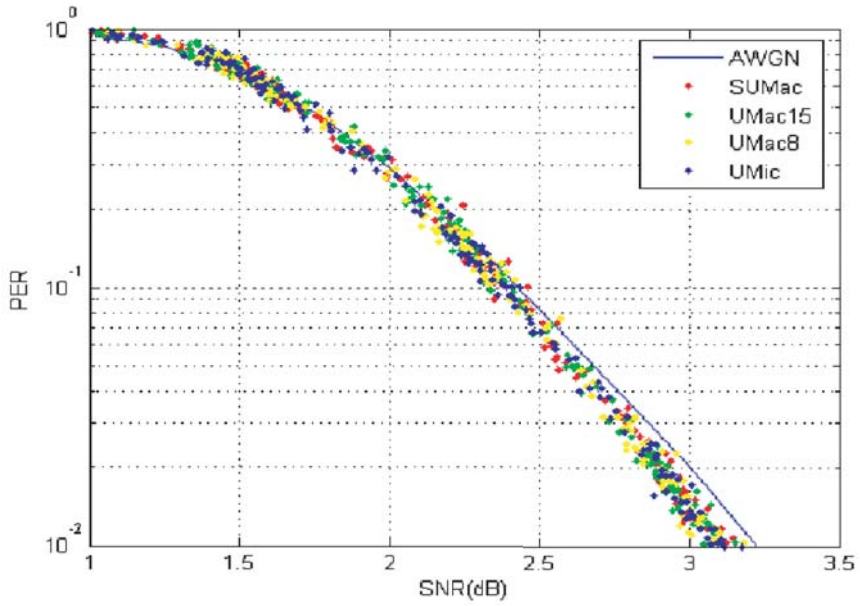

Figure 6.5: Simulated SINRs for the MI–ESM vs. PER, $\beta = 1.16$, QPSK$\frac{1}{2}$ (Alexiou et al., 2005).

ized by flat fading frequency response $\mathbf{H}(f)$ (5.2.2), and, equivalently, in time domain each subcarrier is characterized by its FT, flat fading channel impulse response (4.2.4). In chapter 4.3.2 we presented that flat Rayleigh fading MIMO channel with channel impulse response matrix $\mathbf{H}$ can be decomposed into independent Gaussian SISO channel corresponding to eigenvalues of the matrix $\mathbf{H}^{\dagger}\mathbf{H}$. Hence, the eigenvalues $\{\lambda_1, \lambda_2, \ldots, \lambda_{\min(M_t,M_r)}\}$ are the essential indicators of channel quality and may fully reflect distortion caused by multipath fading propagation. Therefore, separating large- and small–scale fading in the received signal power (2.3.8), we propose to calculate MIMO channel quality in term of SINRs in the following way

$$SINR_k = \frac{\lambda_k C_k C_T}{I_k + N_0} \quad 1 \leq k \leq \min(M_t, M_r)$$

where C_k is the large–scale fading component of received signal power in k^{th} eigenchannel, C_T is transmitted signal power level, I_k is interference power in k^{th} eigenchannel, and N_0 is background noise power.

Then the set of space varying SINRs is mapped to effective SINR value, that is quality measure QM_j of the flat fading MIMO j^{th} subchannel, through the ESM approach

$$QM_j = I^{-1}\left(\frac{1}{\min(M_t, M_r)} \sum_{k=1}^{\min(M_t,M_r)} I(SINR_k)\right)$$

where function $I(\cdot)$ is referred to "information measure" function, and $I^{-1}(\cdot)$ is its inverse.

Here, the proposed ESM approach adaptation for MIMO–OFDM system takes into account frequency–selective and space–selective nature of the channel where different OFDM subcarriers experience different channel gains. Since we suggest to use the MI–ESM or the EESM mapping for accurate compression of frequency resource elements, the proper selection of scaling parameter reduces mismatch between actual BLER and AWGN BLER samples and allows to use proposed mapping for different types of channels.

Chapter 7

Implementation of 4G Performance in SLS

Nowadays need for high data rate, multimedia support and other services are increasing rapidly. Thus, novel fourth generation wireless communication is proposed to provide better speed, high capacity, universal IP based services with lower cost. 4G is expected to be launched in near future, and now different techniques for producing desired features are studied with system level simulators. In this chapter we take an overall look at the implementation of radio interface in 4G wireless system and also briefly describe the principles of dynamic system level simulator (SLS) such as 4G system simulator.

7.1 General Description of the Dynamic SLS

In the previous chapter we learned that cellular network can be modeled by simulations. The simulations are carried out with the help of link level and system level simulators. We described the task of link level simulator in chapter 6.1. The objective of this chapter is to illuminate the functionality of a system level simulator.

System simulators can be divided into two types: static simulators and dynamic simulators. They are distinguished by their modeling of the movement of the mobile terminals and also by the correlation between consecutive time steps. These features are neglected by the static simulators. The static simulators are beneficial in execution speed and in simplicity of result interpretation. But for studying 4G system performance dealing with radio propagation dynamic simulators are desired.

In dynamic simulators the user mobility with change of time reflects a system dynamics. During each simulation step time is updated and movement of mobile terminals around their paths is executed. Also, RRM algorithms are executed in each step as depicted in Figure 7.1. Dynamic simulators allow to evaluate the affect of feedback loops, in which input depends on output.

The results analyzed in this thesis are obtained with a discrete dynamic system level simulator created for 4G wireless system and provided by Nokia Research Center.

4G system simulator is configured as follows. Simulated area is covered with

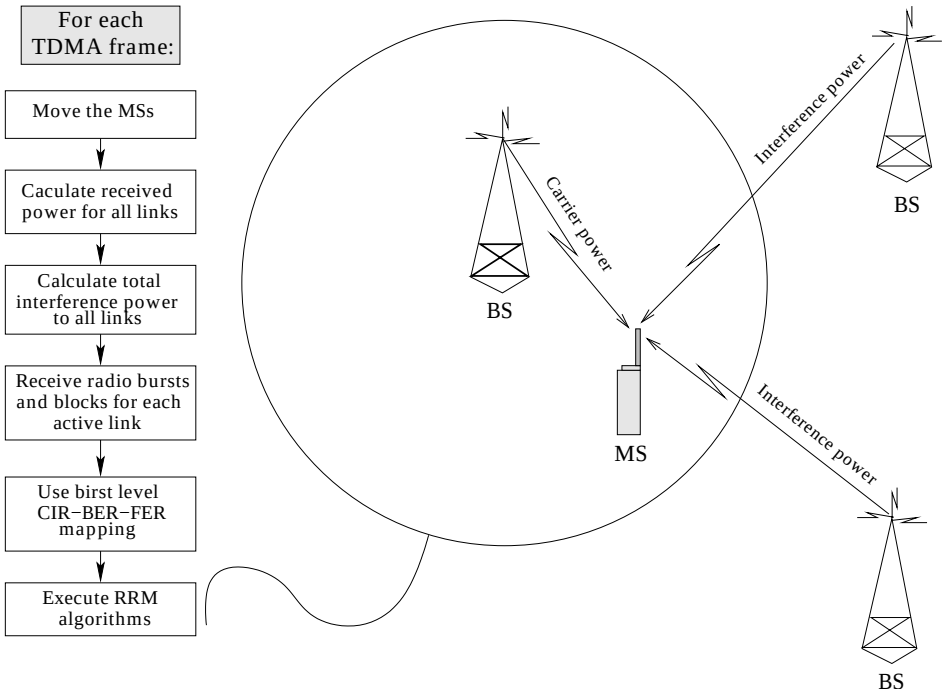

Figure 7.1: Principles of dynamic system level simulator (Romero et al., 2002, p. 574).

10–cell macrocellular network. Each cell has hexagonal shape with diameter of 167 meters. Base stations are located in the corners of each cell. In the case of narrowband transmission clusters with 3 cells and separation of 0.25 km are used. In Figure 7.2 simulation cellular layout with BS locations is represented.

In the simulator TDMA access with TDD is implemented, and both uplink and downlink transmission are simulated. Dualband mode is performed with 102.4 MHz for wideband channel and 20.0 MHz for narrowband channel at 2.5 or 5.0 GHz carrier frequency, respectively. Base stations operate at both modes simultaneously, but mobile stations use only one band at each time step. Mobile station velocity of 3 km per hour corresponding to walking speed is accepted as default parameter value for dynamic simulation behavior. Mobility of mobile stations is realized through the direction change and through the displacement to the new position.

In 4G system simulator OFDM modulation is realized. Simulation time step is defined as single OFDM symbol duration that is 22 microsecond time period by default. Current implementation of simulator holds SISO channel model and provides basic functionality for MIMO channel model.

In 4G system simulator radio related parameters presented in Table 7.1 are used.

Simulations with 40 millions time steps are typically carried out with presented SLS. The simulations usually take time from several days up to one–two weeks. Obtained simulated results are reliable enough for evaluation basic 4G system performance according to presented initial characteristic of the dynamic system simulator.

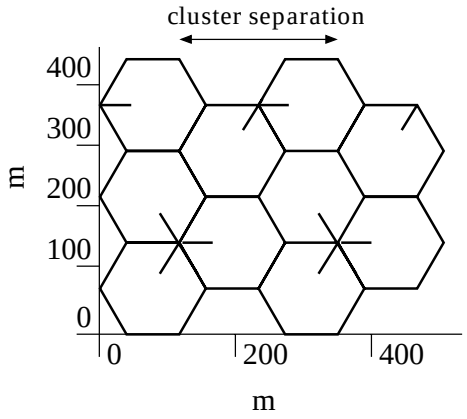

Figure 7.2: 4G cellular network geometry.

Table 7.1: Parameter set for 4G system simulator.

Parameter	Description		Comments
Transmit power	MT	BS	Constant, no power control
dBm	23.0	43.0	
Frequency reuse	Narrowband	Wideband	
	1/3	1/1	
Downlink noise power	Narrowband	Wideband	Includes noise figure
dBm	-94.0	-85.0	of 10 dB
Uplink noise power	Narrowband	Wideband	Includes noise figure
dBm	-98.0	-89.0	of 6 dB
Slow fading model	Log–normal model		
Fast fading model	Rayleigh model		
Basic MCS	BPSK$\frac{1}{2}$		
MCS for DCH	BPSK$\frac{1}{2}$, QPSK$\frac{1}{2}$ 16QAM$\frac{1}{2}$, 16QAM$\frac{5}{6}$		For narrowband only 16QAM$\frac{5}{6}$, for wideband all

7.2 Radio Propagation Modeling in 4G SLS

Radio propagation model has strong relationship with simulation environment where obstacles located along the propagation path produce attenuation, reflection and scattering of the transmitted signal. In 4G system simulator the radio channel is assumed to be constant during one OFDM symbol period and to vary from one OFDM symbol to another. Hence, the propagation is modeled with OFDM symbol time step. Note, however, that different subcarriers within one OFDM symbol can have different channel gains.

Modeling the radio propagation in system level requires to model the received signal strength, interference power and noise power for each time step. Since in 4G SLS OFDM modulation is applied, the received power and interference power are calculated per each subcarrier.

Received Signal Power

Let us recall that the large–scale and small–scale fading components of received power can be computed separately as two independent component random variables (2.3.8). Thus, received signal strength $C_j(f,d)$ for each j^{th} OFDM subcarrier in frequency domain can be written as

$$C_j(f,d) \overset{(3.2.10)}{=} H_j(f;t) \cdot C_T = p(d) \cdot s(d) \cdot f_j(f;t) \cdot C_T \quad 1 \leq j \leq N \tag{7.2.1}$$

where N is a number of OFDM subcarriers, d is a distance between transmitter and receiver, $p(d)$ is mean distance–dependent path loss attenuation factor, $s(d)$ is a shadow fading or large–scale fading value, $f_j(f;t)$ is a fast fading or small–scale fading value. Transmitted power level denoted by C_T is defined in Table 7.1.

Taking into account path loss model (2.3.10) the attenuation factor $p(d)$ is simulated based on used central frequency, distance and environment conditions, e.g., LOS or NLOS transmission. Usually path loss is modeled to fit the measurements in predefined surrounding environment.

Shadow fading $s(d)$ is modeled as log–normally distributed random variable (2.3.12) with zero mean and standard deviation that is equal to 4.0 dB in LOS condition and 5.5 dB in NLOS condition. The correlation between adjacent fading values to a single MS from all close BSs is modeled with the help of autocorrelation function (2.3.13). In 4G SLS shadow fading values are taken from precalculated look–up table depending on transmitter and receiver location d.

Fast fading or small–scale fading caused by multiple paths between transmitter and receiver is calculated for each OFDM subcarrier in frequency domain. From chapter 3.3 we know that multipath channel in time domain is modeled by tapped delay line model where each complex tap gain represents uncorrelated Rayleigh flat fading process. This process is statistically analyzed by autocorrelation function (3.3.15) or classical Doppler spectrum (3.3.16). Improved sum–of–sinusoids Jakes' model provides the accurate simulation of the process (Zheng and Xiao, 2002). The flat Rayleigh fading process through Jakes' model is given by

$$\begin{aligned} h(t) &= h_I(t) + ih_Q(t) \\ h_I(t) &= \sqrt{\frac{2}{M}} \sum_{n=1}^{M} \cos(w_d t \cos\alpha_n + \phi_n) \\ h_Q(t) &= \sqrt{\frac{2}{M}} \sum_{n=1}^{M} \cos(w_d t \sin\alpha_n + \psi_n) \end{aligned} \tag{7.2.2}$$

with

$$\alpha_n = \frac{2\pi n - \pi + \theta}{4M} \quad 1 \leq n \leq M$$

where ϕ_n, ψ_n and θ are statistically independent and uniformly distributed on $[-\pi, \pi)$ interval for all n. Maximum angular Doppler frequency

$$w_d = 2\pi f_m \overset{(2.3.15)}{=} 2\pi \frac{\vartheta}{\lambda_c}$$

occurs with $\alpha_n = 0$. Zheng and Xiao (2002) show that the fading process $h(t)$ has autocorrelation function

$$R_h(\tau) = 2J_0(w_d\tau).$$

Hence, the multiplication of each complex path gain simulated using Jakes' model by proper average envelope power yields needed isotropic Rayleigh fading process (3.3.15).

Zheng and Xiao (2002) prove that the envelope $|h(t)|$ is Rayleigh distributed when parameter M approaches infinity. Good approximation can be achieved with at least eight sinusoids. Thus, fading channel impulse response for one environment is simulated by tapped delay line model with predefined tap delay vector and average envelope power vector. Each time step varying complex tap gain as a fast fading process is simulated according to Jakes' model with $M \geq 8$ and is stored in look–up table with OFDM symbol resolution.

For 4G SLS we need to simulate frequency–selective fast fading process in frequency domain. Due to OFDM modulation the set of flat uncorrelated fast fading processes $\{f_j(f;t)\}$ in frequency domain is required as we showed in chapter 5.1. This set can be obtained in two steps. First, flat discrete channel impulse response for each OFDM subcarrier is modeled as described above. Then set of flat impulse responses is transformed to frequency domain by the DFT or by the FFT, its efficient implementation. Thus, required number of flat discrete frequency responses is simulated.

For open loop MIMO system with M_t transmitting and M_r receiving antennas the received signal strength $C_{jk}(f,d)$ for j^{th} OFDM subcarrier in frequency domain and for k^{th} eigenchannel can be modeled as proposed in section 6.4

$$C_{jk}(f,d) = p(d) \cdot s(d) \cdot \lambda_{jk} \cdot \frac{C_T}{M_t}$$

where λ_{jk} is flat Rayleigh fading MIMO j^{th} subchannel eigenvalue.

Interference power

In 4G SLS the calculation of interference power is performed similarly as received power. From chapter 2.2.2 we know that cellular network experiences different types of interference. In 4G system simulator the number of closest adjacent interference channels is fixed while all co–channel interference is examined. The interference power for each interferer is estimated using received power model (7.2.1). The total interference power is obtained by summing of co-channel interference power with scaled adjacent interference power. Since the scaling factors are not available yet, the adjacent channel interference is not not taken into account in our simulations. In MIMO system total interference power is calculated for each receiving antenna elements.

Noise power

The thermal noise power N_0 is a constant value defined as

$$N_0 = k \cdot T \cdot B \cdot NF$$

where k is Boltzmann constant, temperature T equals to 293K, B is the effective receiver noise bandwidth assumed to 10 MHz for narrowband and 80 MHz for wideband, NF is the noise figure parameter depending on device set to 6 dB for MS and 10 dB for BS. The noise power values for narrowband and wideband dual mode are given in Table 7.1. In MIMO system with M_r receiving antennas noise power N is split between all antenna elements. So, noise level for each receiving antenna is given by $\frac{N}{M_r}$ constant.

7.3 Implementation of L2S Interface in the 4G SLS

In chapter 6.1 we showed that performance analysis of a cellular system is done independently at system level and at link level. Using quality model depicted in Figure 6.1 the signal quality measures, i.e. BER samples, obtained from link level simulator are integrated into in system level through look–up mapping tables. In system level, the mapping tables use instantaneous effective SINR sample as an input and produce BER value as an output. Packet error probability P as a link quality measure is later determined according to the specified model. Since received packet holds probability of error P, random experiment is carried out to detect the final packet error subsequently utilized by the RRM algorithms. We need to emphasize that in MIMO system the performance evaluation is done for each antenna element.

Various approaches for modeling channel quality measures and predicting PER based on these measures bring different accuracy of performance estimation. In this thesis we analyze and compare only two of them, the traditional AVI approach and the advance ESM approach.

AVI Approach

In the traditional L2S interface approach called an Actual Value Interface (AVI) the effective SINR value, $SINR_{AVI}$, is defined as the mean SINR value given by

$$SINR_{AVI} = \frac{1}{N}\sum_{j=1}^{N} SINR_j \tag{7.3.3}$$

$$= \frac{1}{N}\sum_{j=1}^{N} \frac{C_j(f,d)}{I_j + N_0} \tag{7.3.4}$$

where N is a number of OFDM subcarriers, SINR_j is a SINR sample for each j^{th} subcarrier. Received signal strength $C_j(f,d)$, interference power I_j and noise power N_0 are calculated as described in the previous section.

The effective channel quality measures are computed for all OFDM symbols in the packet through chosen L2S interface and the minimum one is later used as mapping table input.

The model of packet error probability P for certain coded BER value p is given by

$$P(p(MCS), l) = 1 - (1 - p)^l$$

where l is the packet length in bits.

Presented PER predicting holds the drawbacks such as lack of fast fading performance in link quality measure calculations and detecting of packet correctness only by the worst quality measure.

The ESM Approach

4G SLS also supports advanced L2S interface through the ESM mapping described in detail in chapter 6. Two variants of effective SINR samples are provided: the EESM case of effective SINR (6.3.5) and the MI–ESM case of effective SINR (6.3.6). For the ESM approach the set of input SINR samples for all OFDM subcarriers are based on received power calculations (7.2.1). Thus, each OFDM subcarrier channel gains is added into effective SINR calculations, and the ESM approach illuminates the frequency–selectivity of the channel. Hence, the ESM approach produces accurate performance estimation, which allows to apply detailed RRM studies.

The mapping function from effective SINR sample to packet error probability is the same as in the AVI approach. We may propose one improvement of the current model. The substitution of packet error probability to OFDM symbol error probability as a function of effective SINR and MCS scheme may yield fast fading performance into result PER sample.

Chapter 8

Simulations

In the previous chapters 6 and 7 we learned that system level and link level simulators are combined through L2S interface to study 4G system performance. In this chapter we present the results of simulations running with 4G SLS. The objective is to compare the results between different L2S interface approaches described in chapters 6 and 7.3

8.1 Testing and Validation

4G system simulator is implemented using C++ object oriented language. The principles of 4G SLS can be described with the following main steps.

- **Initialization.** At initialization stage the simulation environment and propagation model are set, BSs are created in the correct positions and MSs are spread in the cellular network.
- **Simulation loop.** In the simulation loop all steps of dynamic time driven system simulator depicted in Figure 7.1 are realized. The simulation loop starts by updating the time. The receiver side actions, such as calculations of received power, interference power, SINR values and correctness of the transmission, are handled. Using this knowledge RRM algorithms are executed. Then at the transmitter side active links are checked and removed. The simulation loop is continued through traffic generation for active services. For the next stage mobile stations move around their paths, and new transmitting links are initialized. Collecting statistics is the last stage in the simulation loop.

One of the main interest in our simulations is the comparison of results between the different L2S interface approaches. The results are obtained during simulation loop. They are used as input for RRM algorithm for the next stage. Thus, for accurate comparison we want to ensure that the results in pseudo-random simulation with basic settings do not differ from each other.

For the validation of the MI–ESM we tested BICM capacity (6.3.7) through the MI–ESM approach for different modulation schemes. The results obtained in simulations are drawn in Figure 8.1. They conform to the theoretical results presented in Figure 6.4.

For verification of the pseudo–random nature of simulator we set 1000000 steps as network simulation time, that is 22 seconds of real time, with 200 mobile terminals for narrowband channel. The simulations were carried out with three different L2S interface mappings for QPSK$\frac{1}{2}$. The retransmissions were neglected.

Figure 8.2 exhibits collected received powers for the AVI, the EESM and the MI–ESM approaches in uplink and downlink directions. Figure 8.2 clearly presents pseudo-random nature of simulator since all three different kind of simulations provides exactly the same received power without frequency–selectivity.

For verification of the L2S interface we set 1000000 steps as network simulation time, that is 22 seconds of real time, with 200 mobile terminals for narrowband channel. The simulations were carried out with three different L2S interface mappings for two MCSs, QPSK$\frac{1}{2}$ and 16QAM$\frac{1}{2}$.

Figure 8.3 shows that SINR and effective SINR values obtained through the AVI, the EESM and the MI–ESM L2S interface are mapped to corresponding PER reasonably since system level packet error probability equals to link level look–up tables.

8.2 Theoretical Comparison of Advanced L2S Interface Approaches

The objective of SLS is to produce reliable system results, where L2S interface has essential contribution for accurate estimation of the performance. The mapping candidates to model PER performance through multi–state channel link quality measures are the AVI, the EESM and the MI–ESM approaches developed for SISO system and stated in chapter 6. These approaches may be generalized using the ESM mapping (6.3.3) through "information measure" function $I(\cdot)$ that characterizes the channel capacity of a multi–state channel in the following way (Tsai and Soong, 2003)

$$\begin{aligned} I(SINR_{eff}) &= \sum_j p_j I(SINR_j) \\ &\overset{(6.3.3)}{=} \frac{1}{N}\sum_{j=1}^{N} I(SINR_j) \end{aligned} \tag{8.2.1}$$

Here, $p_j = \frac{1}{N}$ is the probability mass function for $SINR_j$ sample in j^{th} subcarrier since the total number of subcarriers equals to N. Note, the function $I(\cdot)$ only characterizes the channel capacity as it may not determine well–defined channel capacity in informational theory.

Represented property (8.2.1) allows to create various mappings of multi–state channel depending on characteristics of used information measure function. The mappings bring different accuracies and efficiencies in performance modeling and may have significant influence on system level evaluation. In this chapter we provide comparison and analysis of advanced L2S interface approaches from information measure point–of–view. Earlier, in chapters 6.3.1 and 6.3.2 we illustrated the ac-

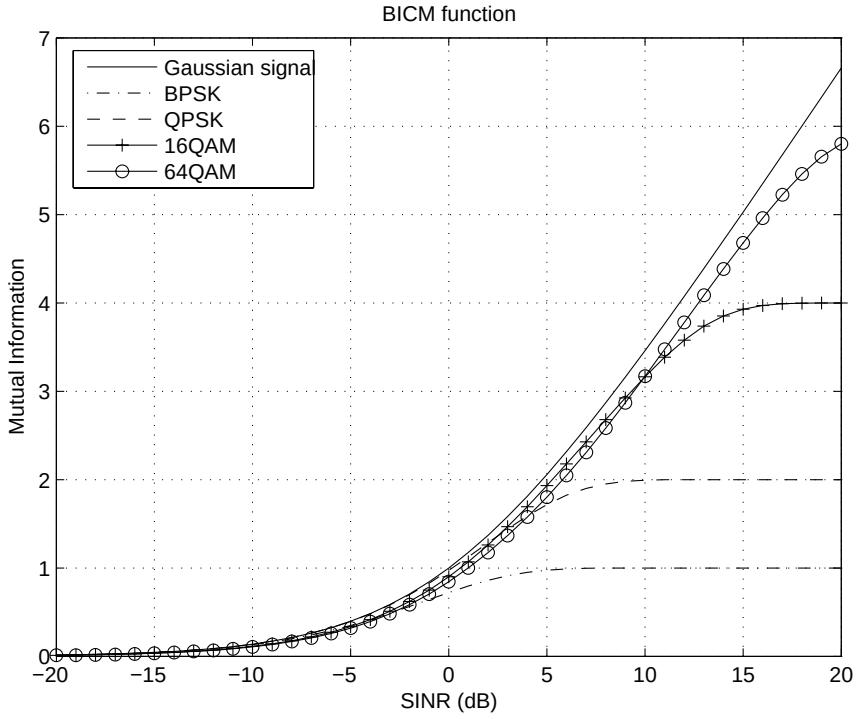

Figure 8.1: BICM modulation function constructed from simulations.

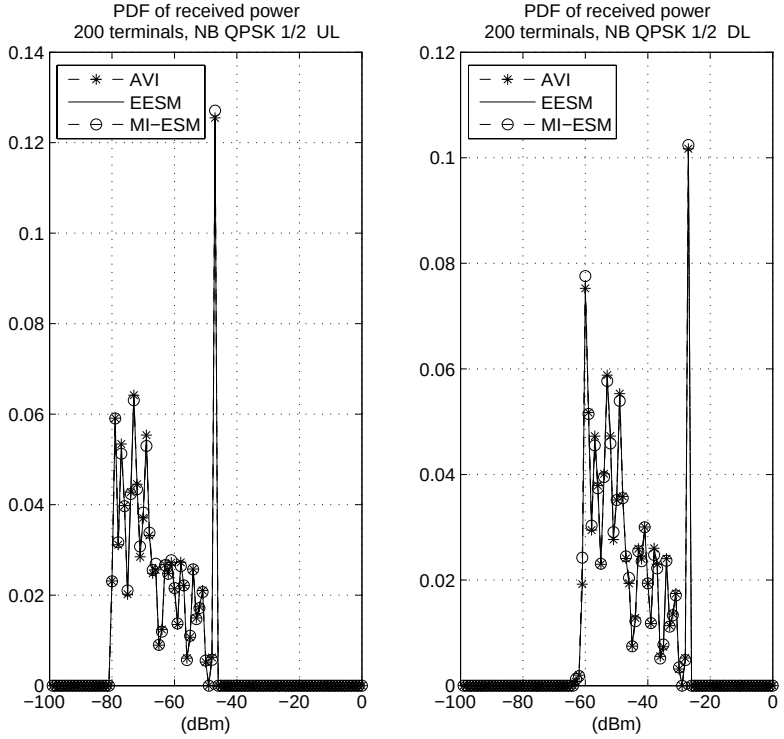

Figure 8.2: PDF of received power for different L2S approaches and MCSs schemes.

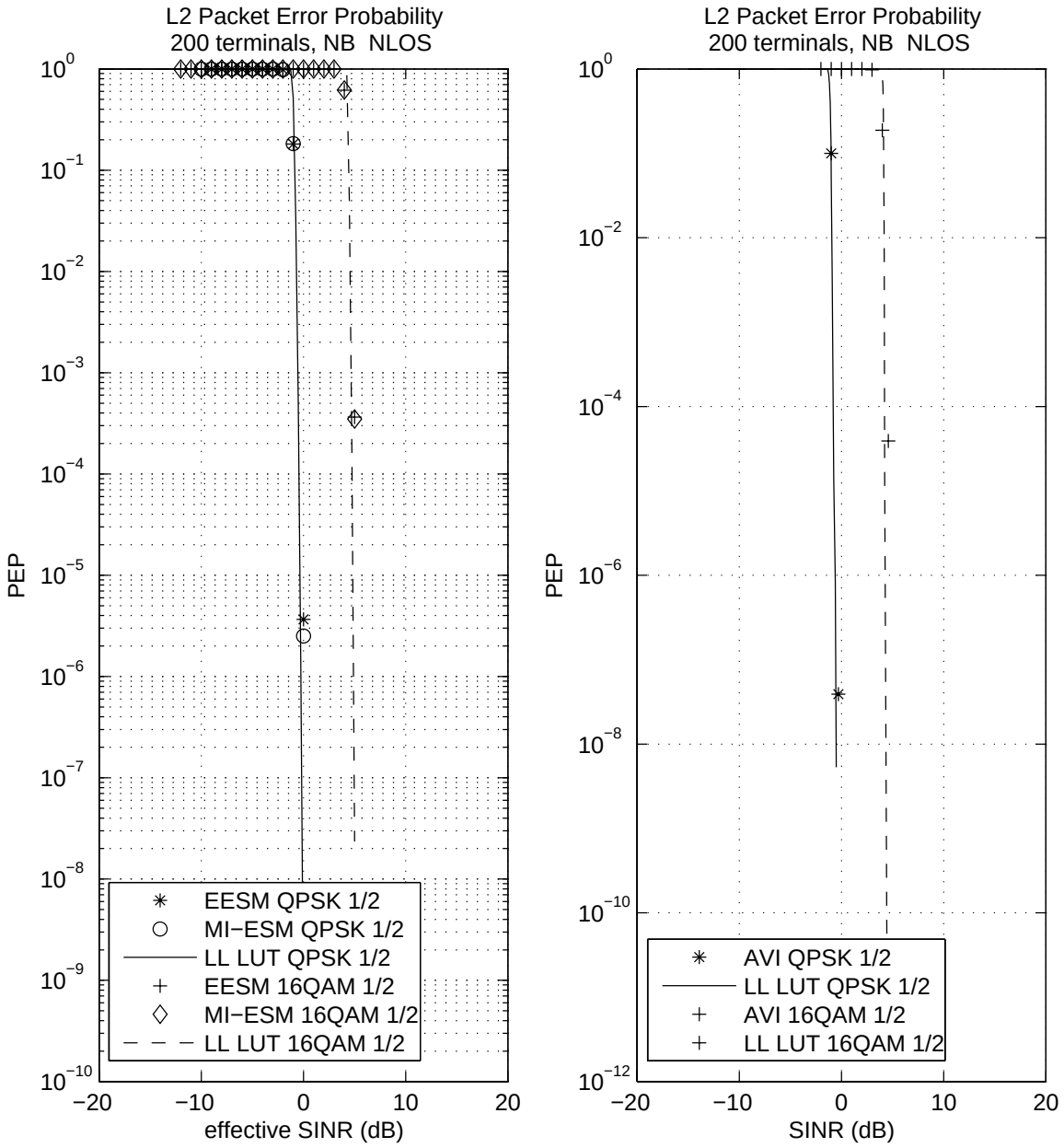

Figure 8.3: Packet error probability of received packets for different L2S approaches and MCSs schemes produced by system level simulator and the curves by link level simulator.

curacy of advanced L2S interface approaches through matching to AWGN channel realization.

Let us first derive the informational measures for each case of L2S interface mapping. For the AVI approach (7.3.3) the quality measure is used directly

$$I(x) = x \tag{8.2.2}$$

as an information measure. Substituting (8.2.2) in (8.2.1), we get the AVI approach itself since

$$\begin{aligned} I(SINR_{AVI}) &= SINR_{AVI} \\ &= \frac{1}{N}\sum_{j=1}^{N} SINR_j. \end{aligned}$$

For the EESM approach (6.3.5) an information measure extended by a scaling factor β and parametrized through A and B parameters is defined as

$$I(x) = A - Be^{\frac{-x}{\beta}} \qquad A, B \in \mathbb{R}. \tag{8.2.3}$$

Such definition of the information measure produces the exponential effective SINR value given by (6.3.5) as substituting (8.2.3) in (8.2.1) yields

$$\begin{aligned} I(SINR_{EESM}) &\overset{(8.2.3)}{=} A - Be^{\frac{-SINR_{EESM}}{\beta}} \\ &\overset{(8.2.1)}{=} \tfrac{1}{N}\textstyle\sum_{j=1}^{N} A - Be^{\frac{-SINR_j}{\beta}} \\ e^{\frac{-SINR_{EESM}}{\beta}} &= \tfrac{1}{N}\textstyle\sum_{j=1}^{N} e^{\frac{-SINR_j}{\beta}} \\ SINR_{EESM} &= -\beta \ln\left(\tfrac{1}{N}\textstyle\sum_{j=1}^{N} e^{-\frac{SINR_j}{\beta}}\right) \end{aligned}$$

The MI–ESM approach (6.3.6) utilizes mutual information function as an information measure by means of BICM capacity (6.3.7).

These information measures are plotted in Figure 8.4 for QPSK$\frac{1}{2}$ and 16QAM$\frac{1}{2}$ MCSs. Notice that, in order to compare the shape of information measure functions A and B parameters for the EESM approach are chosen as follows

$$\begin{aligned} A = B = 1 \quad &\text{if} \quad \text{MCS} = \text{QPSK}\tfrac{1}{2}, \\ A = B = 2 \quad &\text{if} \quad \text{MCS} = \text{16QAM}\tfrac{1}{2}. \end{aligned}$$

Since scaling factor β is adjusted to match effective SINRs to a specific modulation scheme, we represent two curves of information measures for the EESM and the MI–ESM approaches in Figure 8.4. In plots "without beta shifting" parameter β is equal to one for both information measure functions, in plots "with beta shifting" parameter β adapted for 4G system level simulator is given in Table 8.1. It can be observed that β–shifted information measure curves approach in sense of mean square error (MSE). In the case of QPSK$\frac{1}{2}$ matching through β scaling improves MSE from 0.221 to 0.02 value, in the case of 16QAM$\frac{1}{2}$ MSE changes from 3.034 to 0.2955 value.

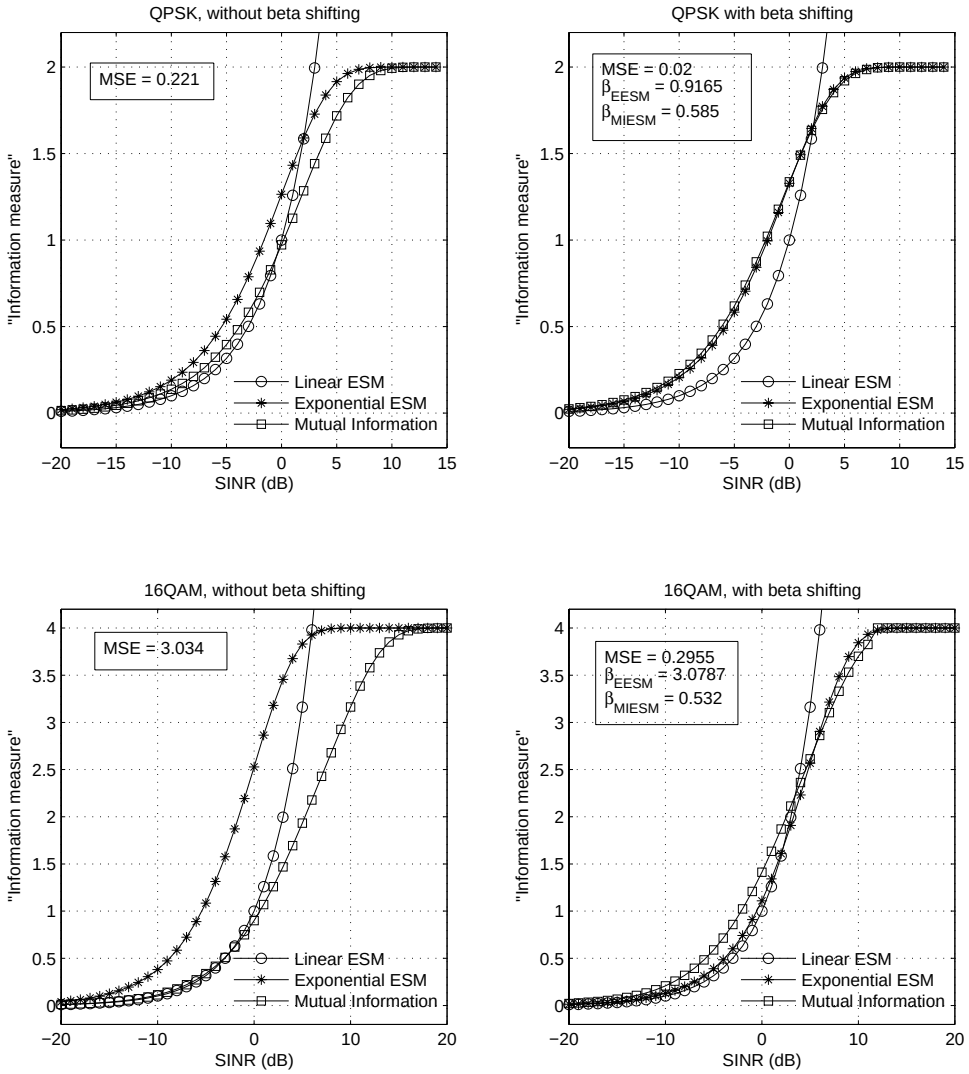

Figure 8.4: "Information measure" function for the AVI, the EESM and the MI–ESM approaches in the case of QPSK modulation with $\frac{1}{2}$ code rate and 16QAM modulation with $\frac{1}{2}$ code rate.

Three information measure curves depicted in Figure 8.4 can be differed on the specific characteristic: convexity or sigmoid (so called S–shape). The AVI information measure function is a convex function, but the EESM and the MI–ESM information measure functions are sigmoidal. This difference partially occurs due to modulation format being involved into the EESM and the MI–ESM information measures, and has a great impact on how various SINR samples are relatively weighted passing through the information measure function. Since the amount of information over precise modulation scheme that a channel can pass should follow the sigmoidal curves (Tsai and Soong, 2003), the AVI convex information measure will overestimate the carried information through overweighting high SINR samples. The EESM and the MI–ESM sigmoidal information measure functions will better describe the information transfered by the SINR samples.

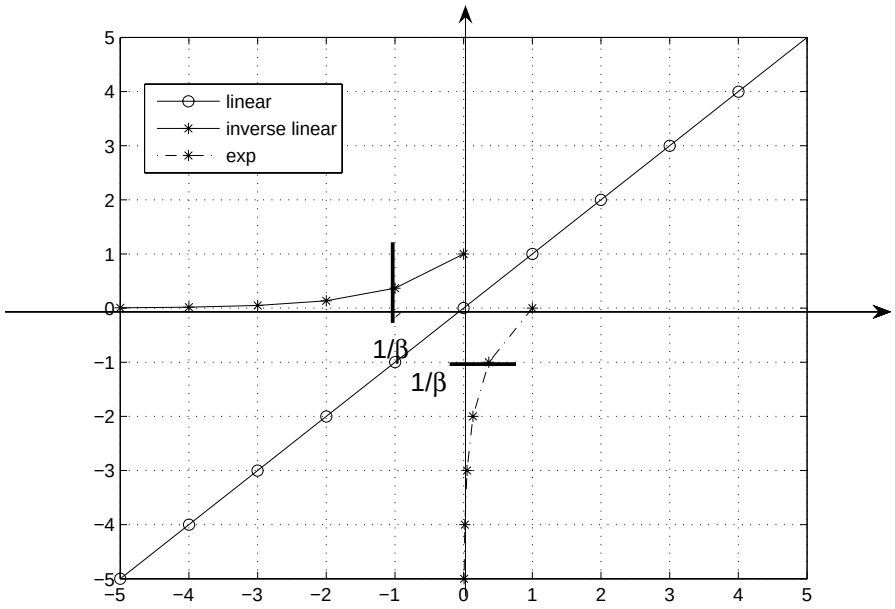

Figure 8.5: Utilization information measure functions in the AVI and in the EESM L2S interface approaches.

Comparing the EESM and the AVI information measure functions shown in Figure 8.5 we should notice that the AVI information measure estimates or relatively weights all SINR samples equally, and result $SINR_{AVI}$ examines the performance for a given channel "on average". This quality measure is later adjusted for a given modulation format estimating the performance in terms of bit error probability.

Instead, the EESM information measure produces relatively higher weights at lower SINRs and relatively lower weights at higher SINRs. Thus, more critical, in sense of presence of errors in a transmitted packet, low SINR samples determine mean value of weighted SINRs, $\frac{1}{N}\sum_{j=1}^{N} e^{-\frac{SINR_j}{\beta}}$. Applying inverse information measure to derived mean value yields higher result for higher mean. Therefore, meaningful SINR samples mainly characterize effective SINR itself.

The MI–ESM information measure in general behaves similarly as the EESM information measure. SINR samples passing through the information measure are evaluated contrastingly: low SINRs and high SINRs are weighted by information measure's low and upper limits respectively, weights for SINRs that may contribute in non-zero bit error probability are widely spread between. Such evaluation of SINR samples allows crucial SINR samples to dominate on performance quality estimation. Comparison of the EESM and the MI–ESM information measures in terms of channel capacity given in (Tsai and Soong, 2003) instead of SINR weighting shows that the MI–ESM information measure better characterizes the system performance, but the EESM measure function also provides accurate results for performance estimation.

Analyzing the behavior of relative weighting for convex and sigmoidal functions let us propose an improvement for the convex AVI information measure. Since sigmoidal functions are bounded, we may also bound the convex AVI information measure so, that crucial SINR samples will have more contribution in final quality measure. As we have mentioned above the EESM and the MI–ESM information measures are bounded by the modulation format and the bandwidth. Thus, these characteristics should define the thresholds for the AVI information measure to indicate crucial SINRs. In the AVI approach the modulation structure and the bandwidth are involved in performance estimating through coded BER calculations. So, the bounds for the AVI information measure may be obtained from link level look–up tables.

The analyzed L2S interface methods are evaluated and compared also through system level simulations. The results and conclusions are performed in the following chapters.

8.3 Performance Benchmarking

General settings for system level simulations are presented in chapters 7.1, 7.2 and in Table 7.1. We choose the simulations to be run with 200 MSs uniformly spread in the 10–cell macrocellular network. Mobile terminal speed was set to be constant 3 km/h. The traffic model for simulations was specified to be constant 1500 byte packet size, constant interval and full downlink traffic load. The simulations were carried out with 128 subcarriers for narrowband transmission. The simulations were run only through SISO system due to incompleteness of the 4G system level simulator for MIMO case.

Figure 8.6 shows simulated radio propagation for these system simulator settings: complex valued Jakes' fast fading, fast fading amplitude, used tap model, simulated channel frequency response for wideband and simulated received power with different resolutions.

In order to explore L2S interface mapping behavior we considered three approaches in our simulations: the AVI and its improved version, the EESM and the MI–ESM discussed in chapters 6, 7.3 and 8.2. For analyzing signal quality as a function of effective SINR we used link level look–up tables depicted in Figure 8.7.

In system level simulations we used only two various MCSs, QPSK$\frac{1}{2}$ and 16QAM$\frac{1}{2}$, and the link adaptation was forbidden. The utilized scaling parameter β

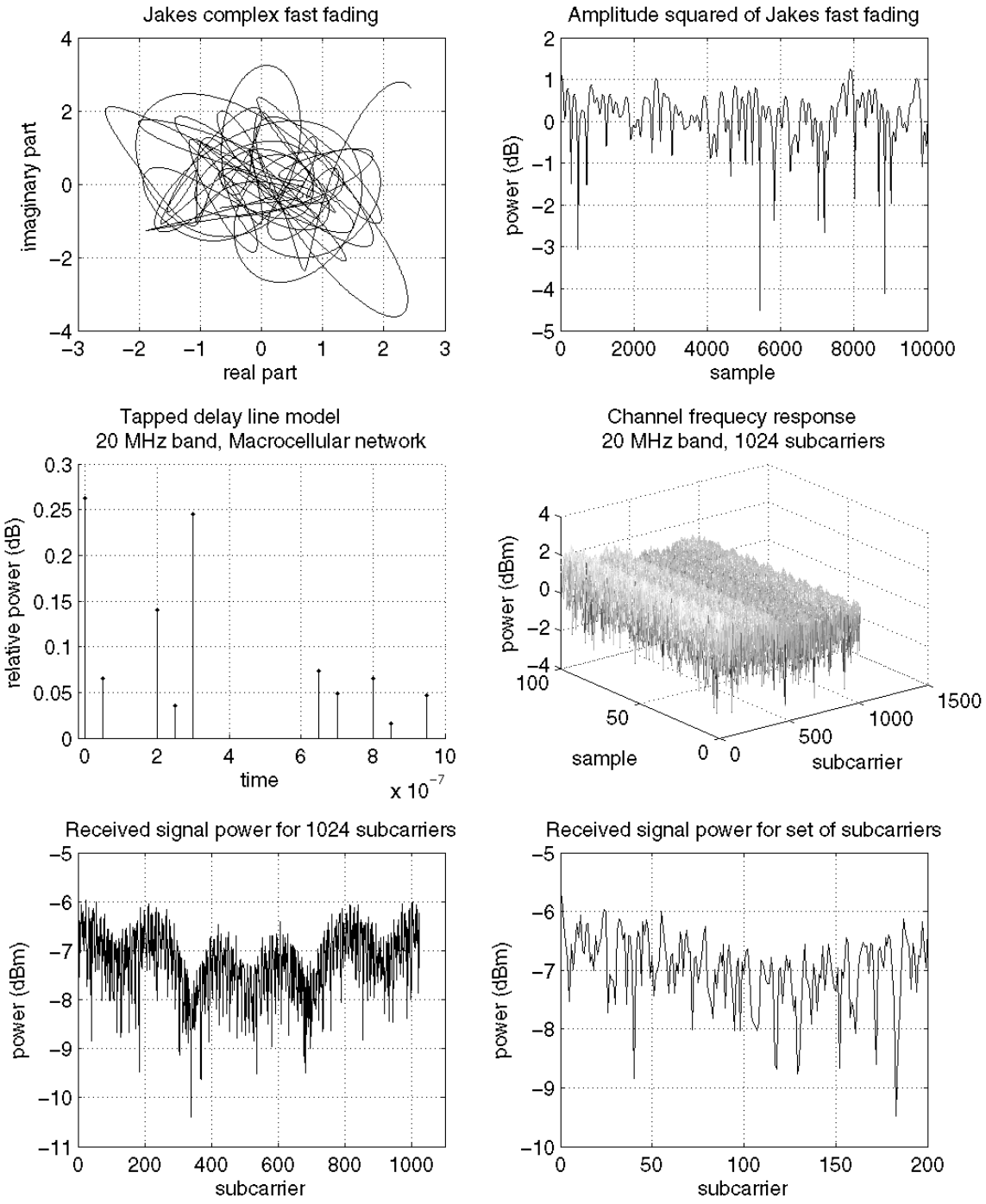

Figure 8.6: Simulated radio propagation: complex valued Jakes' fast fading, fast fading amplitude, tap model, channel frequency response and received power.

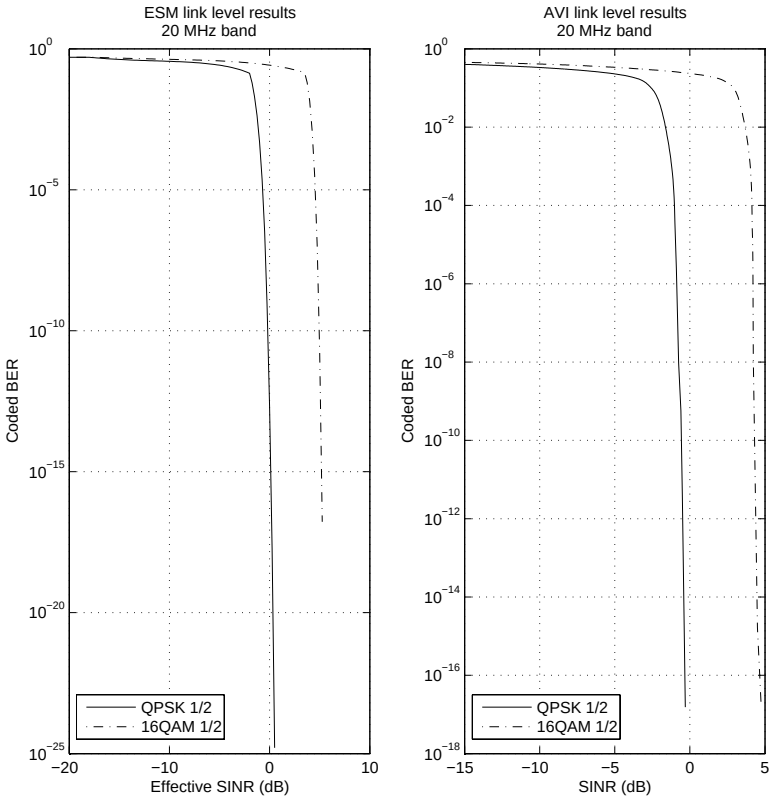

Figure 8.7: Link Level results for BER mapping.

for both MCSs adapted to 4G system simulator is given in Table 8.1. Complying to link level look–up tables for the AVI approach we specified upper and low limits for the AVI information measure shown in Table 8.1.

Table 8.1: Parameter set for β in 4G system simulator.

Modulation	Code Rate	β value EESM	β value MI–ESM	low bound improved AVI	upper bound improved AVI
QPSK	1/2	0.9165	0.585	-15 (dB)	0 (dB)
16QAM	1/2	3.0787	0.532	-15 (dB)	5 (dB)

We ran two different types of simulations: artificial simulations, where all transmitted packets were received correctly, and normal simulations with required retransmissions. The first type of simulations were run with time period of 50000 steps (1.1 second of real time), the second one with 10 millions steps (220 seconds of real time).

Let us first consider simulations where retransmissions were neglected. These simulations allow to illuminate the particular differences between L2S approaches applied to the same set of SINR samples produced by simulator. The simulation results are presented in appendix C.

Comparing simulation results obtained through the EESM and the MI–ESM L2S interfaces for both MCSs illustrated in Figures C.1 and C.7 we may notice that both effective SINRs and final coded BERs have no significant difference. However, if we compare magnitude of coded BER dispersion, the deviation of 1.5747×10^{-4} for QPSK$\frac{1}{2}$ and of 8.9393×10^{-4} for 16QAM$\frac{1}{2}$ can be observed. These results are predictable since adjusted information measure curves do not follow exactly the same shape (see Figure 8.4), and MSE error in the case of 16QAM modulation is approximately 15 times higher. The exponential ESM relatively underweights meaningful SINRs especially noticeably in the case of 16QAM$\frac{1}{2}$ MCS leading to overestimation of system level performance.

Comparing the AVI simulation results with the EESM and the MI–ESM results depicted in Figures C.2, C.3, C.8, C.9, we can immediately find out that the AVI quality measures are significantly differed from the EESM and the MI–ESM simulation results. The variance in effective SINR values was expected since given modulation format is not taken into $SINR_{AVI}$ calculations. But large deviations, occurred in simulated coded BER values achieved through the AVI approach and given in Table 8.2, show that the AVI approach can not accurate estimate the performance.

Table 8.2: Deviation of coded BER values in the AVI and the improved AVI L2S interface approaches.

	QPSK$\frac{1}{2}$		16QAM$\frac{1}{2}$	
	AVI	improved AVI	AVI	improved AVI
EESM	67.4820×10^{-4}	64.4957×10^{-4}	96.7987×10^{-4}	91.3839×10^{-4}
MI–ESM	68.1743×10^{-4}	65.071×10^{-4}	98.9695×10^{-4}	92.6203×10^{-4}

Our proposal for the AVI approach may slightly improve the accuracy of performance estimation. The simulation results given in Figures C.4, C.5, C.10, C.11 and in Table 8.2 indicate less deviations of coded BER values obtained through the improved AVI. So, we can draw into conclusion, that the improved AVI approach produces more reliable quality measures and provides better estimation of the performance, but still can not be equivalent to the EESM and the MI–ESM approaches.

Evaluating advanced L2S interfaces we tried to explore relationship and regularity between spreading SINR samples and final difference of coded BER values. Figures in appendix C constructed for each L2S interface approach show no straight forward relation between variation of the set of SINRs and errors in computed coded BERs. Also we analyzed relations between difference of effective SINR samples and final difference of coded BER values. All figures in appendix C indicate no direct dependence between them.

Figures C.6 and C.12 present linear regressions for simulated coded BER values and exponential regressions for relationships explained above. Once again, presented exponential regressions illustrate no explicit dependency neither between errors in coded BERs and variation of the set of subcarrier's SINR samples nor between errors in coded BERs and effective SINR difference. Comparing constructed linear regressions the higher accuracy of the improved AVI approach for both MCSs can be revealed. Table 8.3 provides the MSE between linear regressions computed for both modulation schemes, where the higher accuracy (lower MSE results) of performance estimation through the improved AVI is demonstrated.

Table 8.3: MSE between linear regressions coded BER values in the AVI and the improved AVI L2S interface approaches.

	$\text{QPSK}\frac{1}{2}$	$\text{16QAM}\frac{1}{2}$
	EESM vs. MI–ESM	EESM vs. MI–ESM
improved AVI vs. MI–EESM	4.0687×10^{-3}	1.2235×10^{-3}
improved AVI vs. EESM	3.8432×10^{-3}	2.3977×10^{-3}
AVI vs. MI–EESM	4.5789×10^{-3}	3.4318×10^{-3}
AVI vs. EESM	4.3540×10^{-3}	3.5194×10^{-3}

The results obtained from normal 4G system simulations let us discover real 4G cellular system performance. The key figures of normal simulations are presented in appendix D.

The link quality measure's distributions for downlink data transmission outlined in Figures D.1 and D.4 reflect similarities in the MI–ESM and the EESM mappings. Confirming to artificial simulation results the distributions of effective SINRs obtained through the MI–ESM and the EESM for QPSK modulation have the same behavior until the MI–ESM effective SINR reaches the upper limit. As stated earlier, for 16QAM modulation the effective SINR samples computed by the EESM and the MI–ESM approaches are noticeably varied, that is explained by differences in information measure functions. The distribution of SINR samples produced by the AVI approach illuminates significant density shifting to higher quality measures that

comes from overestimating the performance through averaging all subcarrier quality measures and not taking modulation format into account. Focusing on the crucial effective SINRs we can reveal higher density of crucial SINR values calculated using the improved AVI approach in comparison with the AVI approach that guarantees the enhancement of estimation accuracy. Note, that the AVI and the improved AVI SINR distribution should not follow the shape of the MI–ESM and the EESM SINR distributions since the modulation format is not included in $SINR_{AVI}$ computation.

Analyzing the amount of erroneously received packets during the simulation time period PER increase for more accurate L2S interface is observed. The results presented in Table D.1 exhibit the maximum percentile of failed packets for the MI–ESM and the minimum percentile of failed packets for the AVI approach. It was anticipated since the AVI produces relatively higher link quality measures that later causes lower packet error probability. The improved AVI affects similarly, but here insignificant SINR samples are upper bounded and relatively lower quality measures in comparison with the AVI approach are produced. Thus, higher packet error probability will be achieved in the case of improved AVI. Since the EESM and the MI–ESM weight crucial SINR values more accurately, the probability of packet error is not underestimated in these cases and larger amount of failed packets is detected. Comparing the results for QPSK and 16QAM modulations, we can find out that the percentile of failed packets for all approaches in case of QPSK modulation is essentially lower since QPSK modulation is more robust.

Figures D.2 and D.5 illustrate distributions of the amount of failed packets depending on estimated link quality for QPSK$\frac{1}{2}$ and for 16QAM$\frac{1}{2}$, respectively. Figures also depict distributions of successfully received packets to demonstrate correct PER mapping. Plotted distributions show high density of failed packets around crucial effective SINRs in the case of the ESM approaches and larger scattering of amount of failed packets in the case of the AVI and its improved version.

When evaluating the performance through system level simulations, data throughput and delay of data packets are the most significant measures of service quality. The data throughput defines the total amount of bits per time step in correctly received data packets during active connection. The packet delay is the time period between two events, when the packet starts to be transmitted by the BS until it is entirely received by the MS. Simulation results for throughput and packet delay in comparison to different L2S interface approaches are depicted in Figure D.3 for QPSK$\frac{1}{2}$ and in Figure D.6 for 16QAM$\frac{1}{2}$, respectively. Their mean values and standard deviations are summarized in Table D.1.

The results show that the different L2S mapping methods do not affect very much on packet delays. However, we should note that packet delay distributions are dominated a lot by non radio related issues like scheduling. Instead, the user perceived throughput has clear relationship with utilized L2S interface approach. According to the simulation results the higher throughput is achieved using the AVI and the improved AVI for link quality estimation. We can outline two main reasons for throughput reduction: larger amount of failed packets and larger amount of retransmissions, that are occurred in the case of the ESM mapping. Throughput reduction for all applied L2S interfaces is naturally happened due to utilization of QPSK modulation format.

8.3.1 CPU Time Results

CPU time that is needed to run the simulations is a very important factor when considering the usability of the L2S interface in practice. Table 8.4 shows CPU time statistics collected from normal simulations running for explored L2S interface approaches for QPSK$\frac{1}{2}$ and 16QAM$\frac{1}{2}$.[1]

Table 8.4: CPU time results.

	QPSK$\frac{1}{2}$	16QAM$\frac{1}{2}$
	dd:hh:mm:ss	dd:hh:mm:ss
AVI	7:00:54:47	4:19:49:37
improved AVI	7:19:49:05	4:23:10:56
EESM	10:13:54:47	6:13:31:19
MI–EESM	10:05:51:16	7:21:53:54

Clearly, the main drawback of the ESM mapping in comparison with the AVI approach is its high simulation time. Moreover, the MI–ESM approach also needs additional offline time to construct BICM function for desirable modulation format. In chapter 6 we discussed that OFDM size reduction may essentially improve CPU cost. Thus, only meaningfully subcariers should be involved into link quality estimation through advanced L2S interface mappings.

8.3.2 Conclusions

In chapter 6 we presented that both the EESM and the MI–ESM approaches provide a relative accurate technique to model OFDM link level performance. For the AVI approach link level look–up tables are constructed for one specific channel model and allow to evaluate the OFDM performance in link level for a given channel model reasonably. In this thesis we focused on evaluating the OFDM performance of 4G wireless system through chosen L2S interfaces in system level.

First, when comparing the L2S interface approaches from theoretical point–of–view, we can conclude the following. The differences in information measure curves leads to essential differences in link quality measures, that are later used to estimate the performance in terms of probability of bit errors. The EESM and the MI–ESM produce quite similar results in the case of QPSK modulation, but slight variance is observed in the case of 16QAM modulation. Evaluation of the performance through the AVI approach can cause the overestimation, and its improved version can only slightly increase the accuracy.

The simulation results justify that the ESM mappings provide good accuracy for QPSK modulation and the MI–ESM estimates better the performance in the case of 16QAM modulation due to taking into account the modulation format in BICM mutual information in a suitable way. The AVI approach provides too optimistic estimation that is indicated through achieved throughput. The improved AVI may

[1] The simulations were run under Linux 2.4 compatible operating system with 3 GHz processors. The time period of simulations was 10 millions steps.

compensate the lack of 'average' weighting but still is not comparable with the ESM mappings.

The CPU time required for simulations is one of the biggest disadvantage of the ESM mappings, but it can be reduced using only meaningful subcarriers for effective SINR calculations.

The conclusion can be drawn as follows. The ESM mapping should be used to produce accurate evaluation of system level performance. The MI–ESM approach for higher modulation is more accurate but already the EESM approach demonstrates good accuracy and requires less CPU time. The AVI approach involving suggested improvement can be used instead when CPU time is essential or when higher inaccuracy in results can be tolerated.

Chapter 9

Conclusion

In this thesis we went through the major principles of radio propagation and channel modeling and made an overview of OFDM and MIMO techniques applied to 4G wireless system. We carefully analyzed advanced L2S interface approaches that accurately estimate OFDM system performance. In this chapter we summarize the results of comparison of presented L2S interfaces and outline the next steps of further research in performance evaluation.

9.1 General Conclusion

The thesis aimed to investigate and evaluate efficiency and accuracy of performance estimation through advanced EESM and MI–ESM approaches and traditional AVI approach. Existing AVI approach was improved to provide better estimate of OFDM performance.

The analyzed L2S interface methods were compared through information measure point–of–view and system level simulations.

4G dynamic OFDM/TDMA/TDD/SISO system level simulator was used to carry out all required simulations. The simulations were run in macrocellular network with 10–cells for QPSK$\frac{1}{2}$ and 16QAM$\frac{1}{2}$ modulation and coding scheme and 200 uniformly spread MSs to verify the similarity and the difference in mappings. The link level look–up tables and scaling parameters were provided for given MCSs. For each modulation two types of simulations were run: artificial simulations, where all transmitted packets were received correctly, and normal simulations with required retransmissions.

The artificial simulations showed that the EESM and the MI–ESM provided good accuracy in case of QPSK modulation. For 16QAM modulation the EESM was less accurate and slightly overestimated the performance. Nevertheless, the link quality measures in terms of BER values were sufficiently similar in order to yield reasonable accuracy. The AVI approach clearly provided low accuracy of multi–state channel performance estimation for both modulations. Our improvement could hardly enhance accuracy, but still could not be compared to the ESM mappings.

The normal simulations produced the simular results. Unfortunately, the CPU time required for the advanced L2S mapping is high compared to the traditional mapping. Therefore, the improvements are desired to reduce running time.

9.2 Future Study Items

In the study of 4G wireless system performance there is a number of key areas for future research that may have major impact on proposed requirements. One of them is the modeling of multiple antenna techniques in system level. As we indicated earlier, the link–to–system interface for MIMO system combined with OFDM technique is still an open research field. Further development of the L2S interface that will produce accurate quality measure of time, frequency and space resources simultaneously should be provided and evaluated through simulations. Thus, our proposal for MIMO system should be specified and its accuracy should be examined through 4G SLS.

Further investigation of advanced L2S interface will be both of high relevance and high interest to examine. The comparison of various L2S interfaces in the case of mixed modulation, carefully modeled frequency–selective co–channel interference, presence of adjacent channel interference through 4G system simulations may reveal new issues that were not covered in this thesis.

Future optimization of system level simulator will be extremely needed work. Since required CPU time is one of the main critical characteristics, new approaches should be studied and applied to 4G SLS to speed up L2S interface in particular and the whole simulations in general.

Appendix A

Rayleigh Fading Channel

Theorem A.1 *Let $H = X + iY$ be a random Gaussian variable with i.i.d. normal random real and imaginary parts with zero–mean, i.e., $X, Y \sim N(0, \sigma^2)$. Then the random variable $R = \sqrt{X^2 + Y^2}$ is Rayleigh distributed, i.e.,*

$$p_R(x) = \frac{x}{\sigma^2} e^{-\frac{x^2}{2\sigma^2}} \quad x \geq 0$$

and the random variable $\Phi = \arctan\left(\frac{Y}{X}\right)$ is uniform distributed, $\Phi \sim$ Uniform$(-\pi, \pi)$, i.e.,

$$p_\Phi(x) = \frac{1}{2\pi}.$$

Proof. Since X and Y are independent and $X, Y \sim N(0, \sigma^2)$, therefore,

$$p_{X,Y}(x, y) = p_X(x) \cdot p_Y(y) = \frac{1}{2\pi\sigma^2} e^{-\frac{x^2+y^2}{2\sigma^2}}. \tag{A.1}$$

Let us then express X and Y by means of R and Φ.

$$\begin{aligned} X &= R\cos(\Phi) \\ Y &= R\sin(\Phi) \end{aligned}$$

Now with the help of bivariate transformation, we get

$$\begin{aligned} p_{R,\Phi}(r, \phi) &= p_{X,Y}(r\cos\phi, r\sin\phi)|J(r, \phi)| \\ &\overset{(A.1)}{=} \frac{1}{2\pi\sigma^2} e^{-\frac{(r\cos\phi)^2 + (r\sin\phi)^2}{2\sigma^2}} \begin{vmatrix} \frac{\vartheta X}{\vartheta r} & \frac{\vartheta X}{\vartheta \phi} \\ \frac{\vartheta Y}{\vartheta r} & \frac{\vartheta Y}{\vartheta \phi} \end{vmatrix} \\ &= \frac{1}{2\pi\sigma^2} e^{-\frac{r^2\left(\cos^2\phi + \sin^2\phi\right)}{2\sigma^2}} \begin{vmatrix} \cos\phi & -r\sin\phi \\ \sin\phi & r\cos\phi \end{vmatrix} \\ &= \frac{1}{2\pi\sigma^2} e^{-\frac{r^2}{2\sigma^2}} r(\cos^2\phi + \sin^2\phi) \\ &= \frac{r}{2\pi\sigma^2} e^{-\frac{r^2}{2\sigma^2}}. \end{aligned} \tag{A.2}$$

So, we are able to calculate the probability density functions for R and Φ.

$$
\begin{aligned}
p_R(r) &= \int_0^{2\pi} p_{R,\Phi}(r,\phi)d\phi \\
&\overset{\text{(A.2)}}{=} \int_0^{2\pi} \frac{r}{2\pi\sigma^2} e^{-\frac{r^2}{2\sigma^2}} d\phi \\
&= \frac{r}{\sigma^2} e^{-\frac{r^2}{2\sigma^2}}, \quad r \geq 0, \\
p_\Phi(\phi) &= \int_0^{\infty} p_{R,\Phi}(r,\phi)dr \\
&\overset{\text{(A.2)}}{=} \int_0^{\infty} \frac{r}{2\pi\sigma^2} e^{-\frac{r^2}{2\sigma^2}} dr \\
&= \int_0^{\infty} \frac{1}{2\pi} e^{-\frac{r^2}{2\sigma^2}} d\frac{r^2}{2\sigma^2} \\
&= \frac{1}{2\pi} \square
\end{aligned}
$$

Appendix B

The Fast Fourier Transform

The DFT transform discussed in chapter 3.1.2 can be applied to any N length sequence, but the transformation takes $\mathcal{O}(N^2)$. The FFT algorithm originally developed by Cooley and Tukey around 1965 is much faster, it takes only $\mathcal{O}(N \log N)$. The algorithm is simplified if the length of the sequence is a power of 2, but it is not a requirement.

There are other FFT algorithms that are differ from Cooley–Tukey algorithm. Some of them are developed for the special case of sequence length, others are developed for real value sequences. Here, we discuss only original Cooley–Tukey algorithm.

The Cooley–Tukey algorithm splits the DFT of size $N = N_1 N_2$ in terms of smaller DFTs of sizes N_1 and N_2, recursively. Let us assume for simplicity that $N = 2^n$. Here, we present the most common form of the Cooley–Tukey algorithm called a radix–2 decimation–in–time FFT, that splits the problem size into two equal parts each recursive step.

B.0.1 Divide and Conquer Method

First, let us explain why it is possible to break the DFT of N length sequence into two DFTs of $N/2$ sequences, one of which consists of odd entries and another consists of even entries of the original sequence.

Let us recall the DFT (3.1.3) is applied to sequence $f(0),\ f(1),\ \ldots,\ f(N-1)$.

Defining $\omega_N = e^{-i2\pi/N}$ as N^{th} root of unity and denoting $M = N/2$, we get

$$\begin{aligned}
\mathcal{F}(\xi) &\overset{(3.1.3)}{=} \frac{1}{2M}\sum_{x=0}^{2M-1} f(x)\omega_{2M}^{\xi x} \\
&= \frac{1}{2}\left(\frac{1}{M}\sum_{x=0}^{M-1} f(2x)\omega_{2M}^{\xi(2x)} + \frac{1}{M}\sum_{x=0}^{M-1} f(2x+1)\omega_{2M}^{\xi(2x+1)}\right) \\
&\overset{(*)}{=} \frac{1}{2}\left(\underbrace{\frac{1}{M}\sum_{x=0}^{M-1} f(2x)\omega_{M}^{\xi x}}_{\mathcal{F}_{\text{even}}(\xi)} + \underbrace{\frac{1}{M}\sum_{x=0}^{M-1} f(2x+1)\omega_{M}^{\xi x}}_{\mathcal{F}_{\text{odd}}(\xi)}\omega_{2M}^{\xi}\right) \\
&= \frac{1}{2}\left(\mathcal{F}_{\text{even}}(\xi) + \mathcal{F}_{\text{odd}}(\xi)\right) \qquad \text{(B.1)}
\end{aligned}$$

where (*) transition is possible due to following property

$$\omega_{2M}^{\xi(2x)} = e^{-i2\pi\xi(2x)/2M} = e^{-i2\pi\xi x/M} = \omega_M^{\xi x}.$$

Using the properties of ω

$$\omega_M^{M+\xi} = \omega_M^{\xi} \quad \text{and} \quad \omega_{2M}^{M+\xi} = -\omega_{2M}^{\xi}$$

we can also have

$$\mathcal{F}(\xi + M) = \frac{1}{2}\left(\mathcal{F}_{\text{even}}(\xi) - \mathcal{F}_{\text{odd}}(\xi)\omega_{2M}^{\xi}\right). \qquad \text{(B.2)}$$

Now the DFT of N length sequence can be computed with division into two parts: the first part of $\mathcal{F}(\xi)$ for $\xi = 0, \ldots, M-1$ is calculated according to equation (B.1) and the second part of $\mathcal{F}(\xi)$ for $\xi = M, \ldots, 2M-1$ is calculated according to equation (B.2). Thus, we obviously obtain divide and conquer method.

We want to emphasize that the same algorithm is possible to use for the inverse DFT with a simple modification. We need to take the complex conjugate of the IDFT

$$f^*(x) \overset{(3.1.4)}{=} \sum_{\xi=0}^{N-1} \mathcal{F}^*(\xi)e^{-i2\pi\xi x/N}.$$

For using divide and conquer method we need, first, to take the complex conjugate of the Fourier space data and to put the complex conjugate through a forward algorithm. After that we need to take the complex conjugate of the result and, finally, to multiply each value by N.

B.0.2 Three Main Steps of the FFT Algorithm

In the previous section we showed how the IDFT can be computed using divide and conquer method originally developed for the DFT. Therefore, in this section we represent only the FFT algorithm since the IFFT algorithm can be obtained easily from it.

The FFT algorithm follows three main steps (Smith, 1997): time domain decomposition, frequency spectra calculating and frequency domain synthesis.

Time domain decomposition. During the first step the FFT decomposes time domain sequence with length of N into N time domain sequences each consisted of one entry. The decomposition process consists of $\log N$ stages. During each stage the sequence is separated into its even and odd numbered sequences. The decomposition process is shown in Figure B.1. In this example, a sequence of 16 numbers is decomposed through 4 stages.

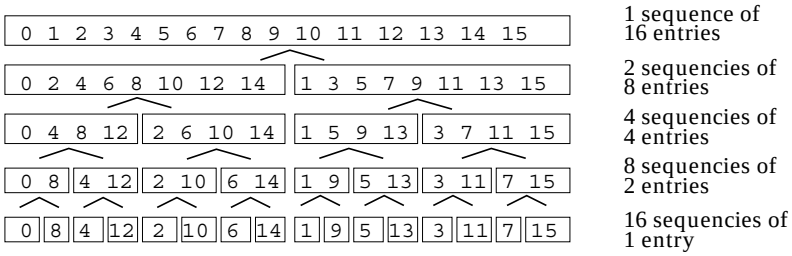

Figure B.1: The FFT time domain decomposition (Smith, 1997, p. 228).

In Figure B.2 entries of original sequence are listed with their binary representations on the right and entries of decomposed sequence are listed also with their binary representations on the left. It can be noticed that the binary numbers of corresponding original and decomposed entries are reversals of each other.

Entry numbers in normal order			Entry numbers after bit reversal	
Decimal	Binary		Decimal	Binary
0	0000		0	0000
1	0001		8	1000
2	0010		4	0100
3	0011		12	1100
4	0100		2	0010
5	0101		10	1010
6	0110		6	0100
7	0111		14	1110
8	1000		1	0001
9	1001		9	1001
10	1010		5	0101
11	1011		13	1101
12	1100		3	0011
13	1101		11	1011
14	1110		7	0111
15	1111		12	1111

Figure B.2: The FFT time domain decomposition bit reversal sorting (Smith, 1997, p. 229).

Thus, the FFT time decomposition is carried out by bit reversal sorting algorithm, i.e., reordering of entries is done by counting binary representation of original entries and flipping the bits left–for–right.

Frequency spectra calculating. The second step of the FFT is to find frequency spectra of the time domain sequence with only one entry. But according to the DFT equation (3.1.3) such frequency spectrum is equal to the sequence entry itself. That means that there is no calculations during this step.

Frequency domain synthesis. During the last step the FFT combines all N frequency spectra in the reverse order that the first step was hold. Such kind of combining in frequency domain is called synthesis, and it must correspond to the time domain combining.

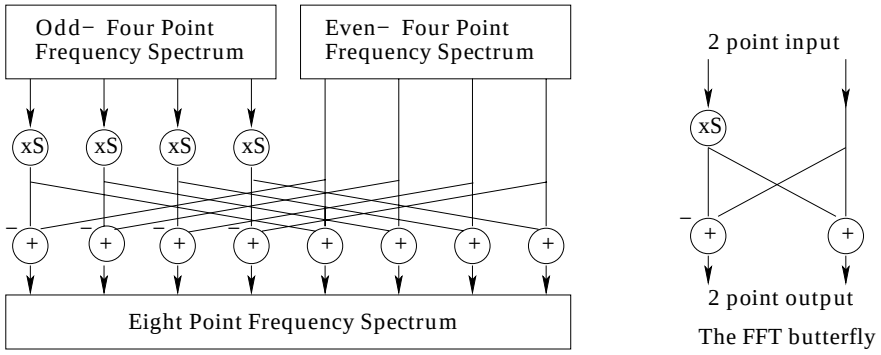

Figure B.3: The FFT synthesis flow diagram (Smith, 1997, p. 231).

Figure B.3 shows a flow diagram for combining two sequences of 4 entry spectra into a sequence of 8 entry spectra. Duplication of the frequency spectrum corresponds to diluting time domain sequences with 4 entries with zeroes. Multiplying by sinusoid in frequency domain corresponds to time domain shift to the right by the sequence with originally odd entries.

We should note that Figure B.3 consists of the basic pattern called the FFT butterfly. It is the basic element of the FFT algorithm. It makes a transformation of two complex numbers in two other complex numbers. It is repeated for all frequency spectra each stage.

Thus, all three steps of the FFT algorithm can be represented in flow diagram depicted in Figure B.4. The following description of this diagram is given in (Smith, 1997).

"Figure B.4 shows the structure of the entire FFT. The time domain decomposition is accomplished with a bit reversal sorting algorithm. Transforming the decomposed data into the frequency domain involves nothing and therefore does not appear in the figure. The frequency domain synthesis requires three loops. The outer loop runs through the $\log N$ stages. The middle loop moves through each of the individual frequency spectra in the stage being worked on. The innermost loop uses the butterfly to calculate the points in each frequency spectra. The overhead boxes determine the beginning and ending indexes for the loops, as well as calculating the sinusoids needed in the butterflies."

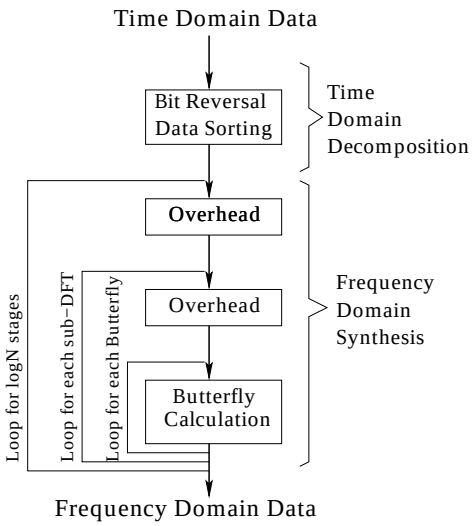

Figure B.4: Diagram of three main steps of the FFT (Smith, 1997, p. 232).

Appendix C

Comparison Results

In the following Figures results obtained with 4G system level simulator for comparison L2S interface approaches are presented. 4G SLS set with parameters given in chapters 7.1 and 8.2. The simulation running time was chosen as 50000 time steps. No retransmission statistics were accumulated from all packets. Data were collected with received packet resolution.

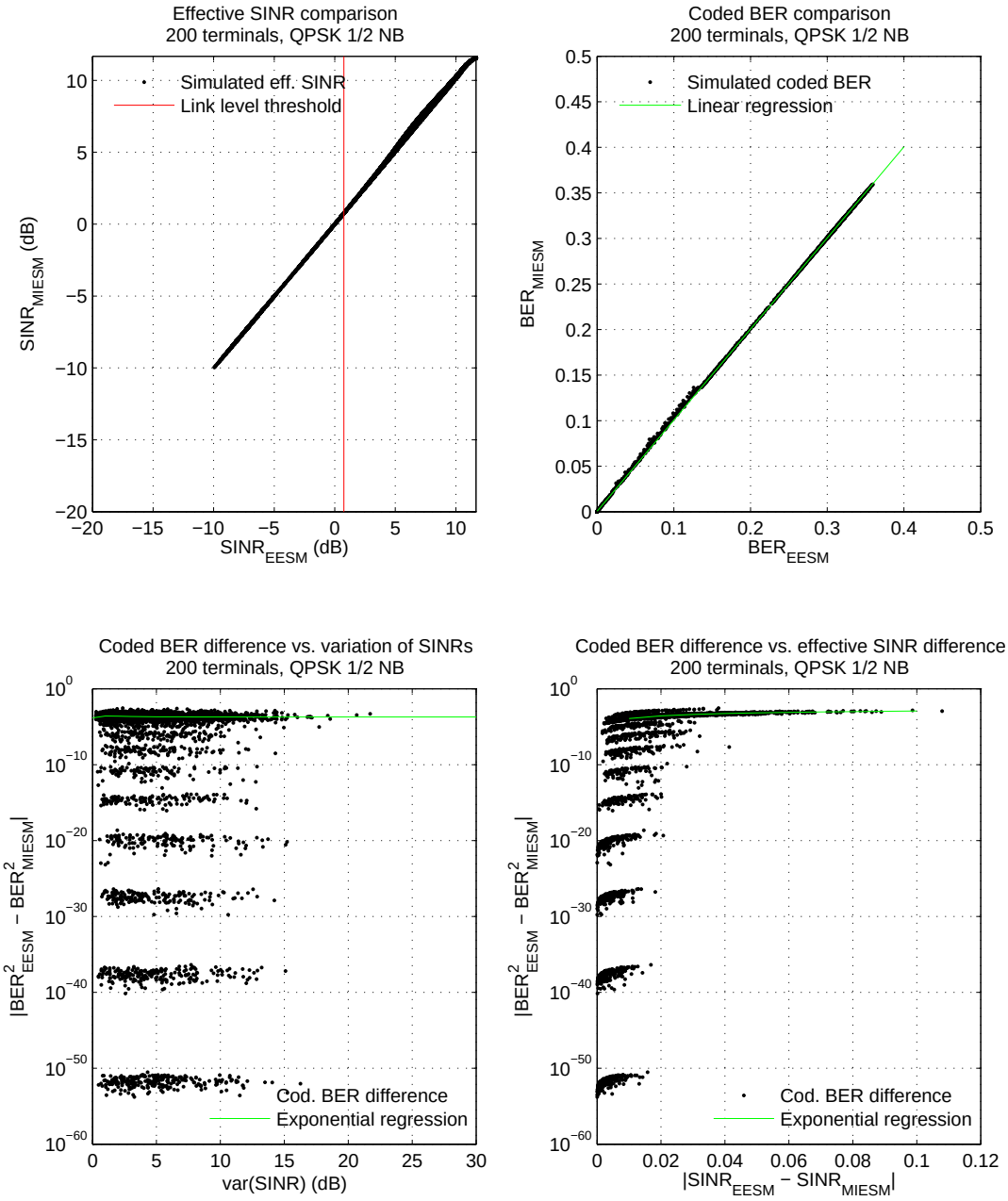

Figure C.1: Comparison of collected effective SINR and coded BER values obtained using the EESM and the MI–ESM approaches in 4G system level simulations for QPSK$\frac{1}{2}$.

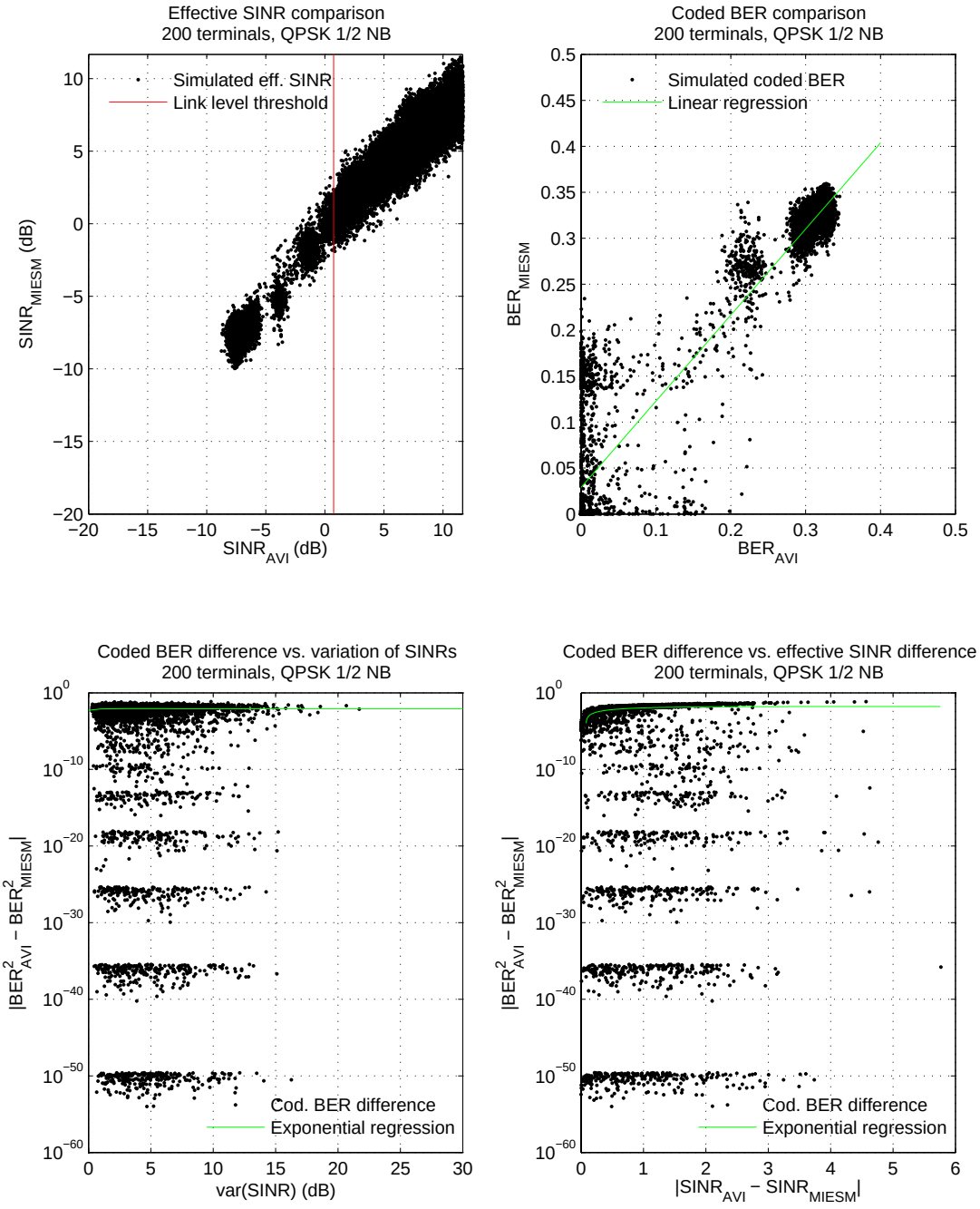

Figure C.2: Comparison of collected effective SINR and coded BER values obtained using the AVI and the MI–ESM approaches in 4G system level simulations for QPSK$\frac{1}{2}$.

Figure C.3: Comparison of collected effective SINR and coded BER values obtained using the AVI and the EESM approaches in 4G system level simulations for QPSK$\frac{1}{2}$.

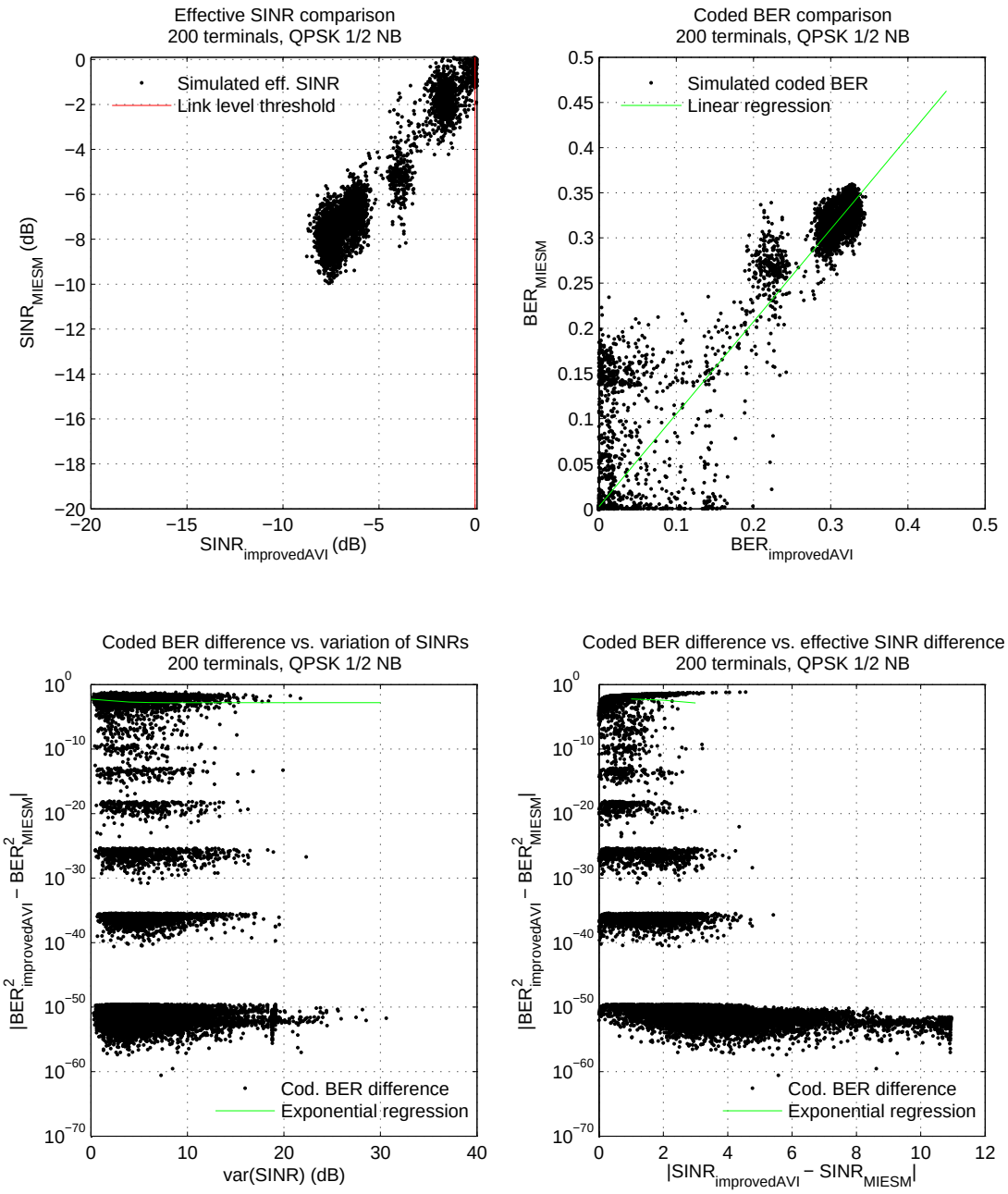

Figure C.4: Comparison of collected effective SINR and coded BER values obtained using the improved AVI and the MI–ESM approaches in 4G system level simulations for QPSK$\frac{1}{2}$.

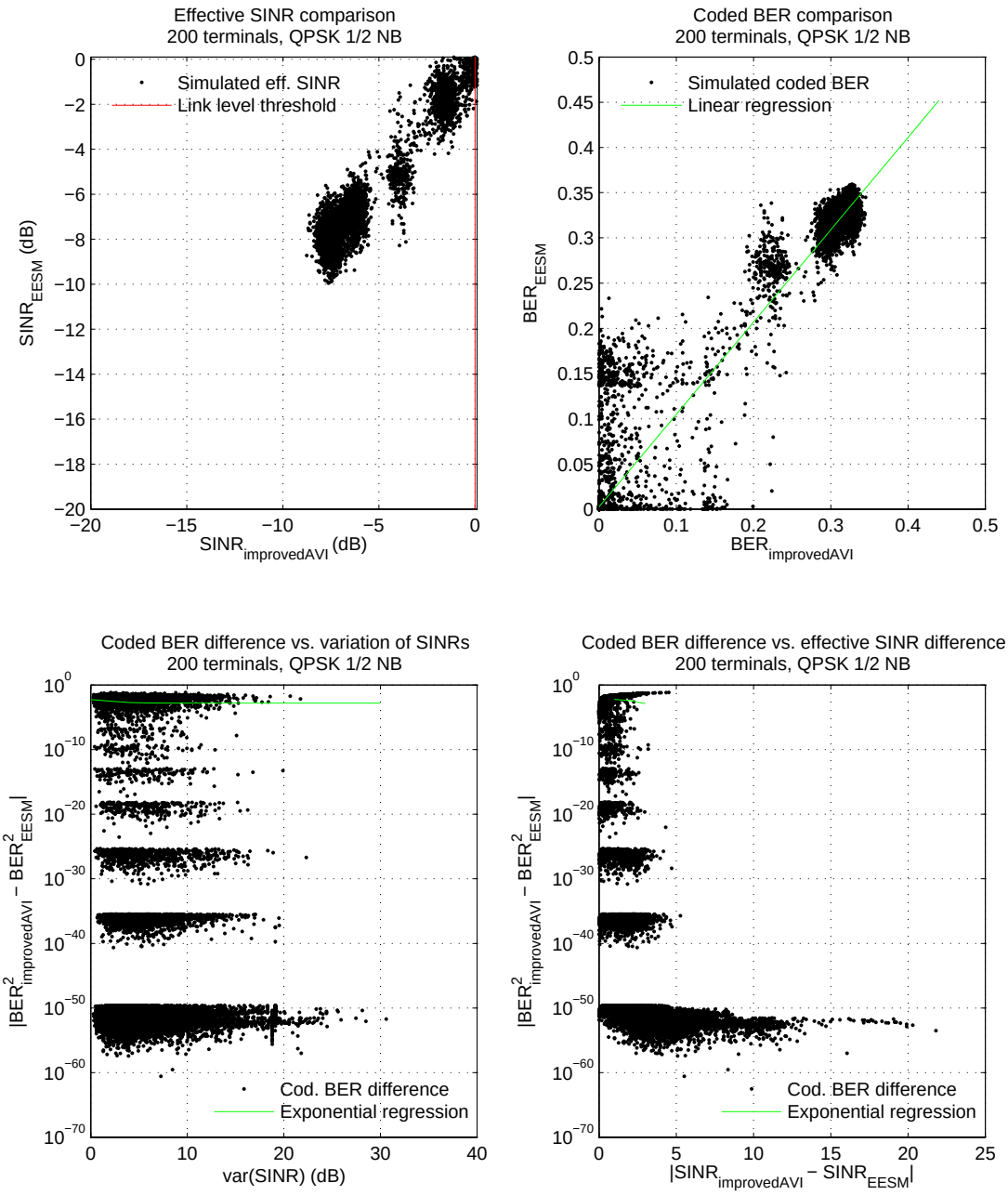

Figure C.5: Comparison of collected effective SINR and coded BER values obtained using the improved AVI and the EESM approaches in 4G system level simulations for QPSK$\frac{1}{2}$.

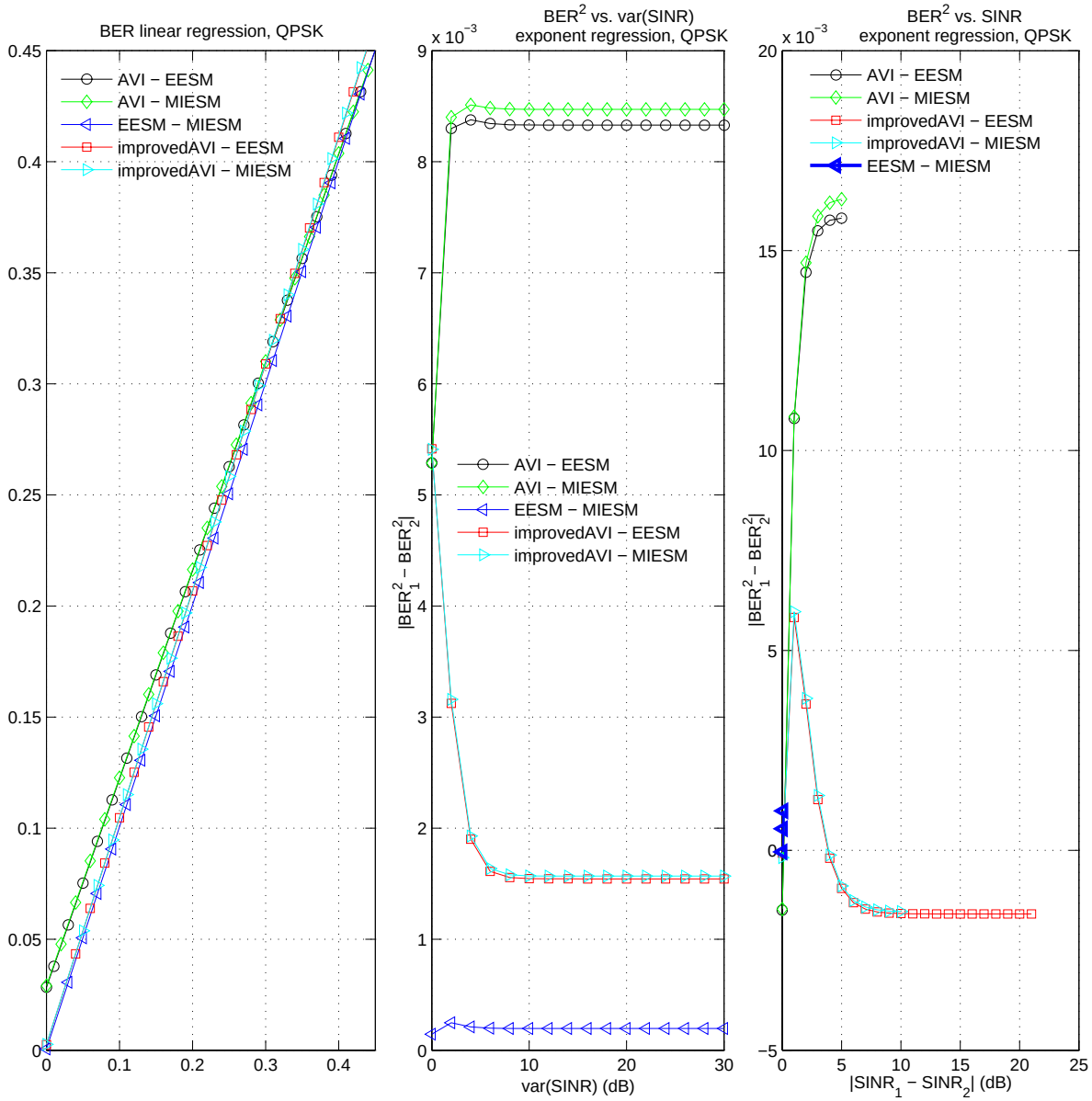

Figure C.6: Linear and exponential regressions based on collected effective SINR and coded BER values obtained using the AVI, the improved AVI, the EESM and the MI–ESM approaches in 4G system level simulations for QPSK$\frac{1}{2}$.

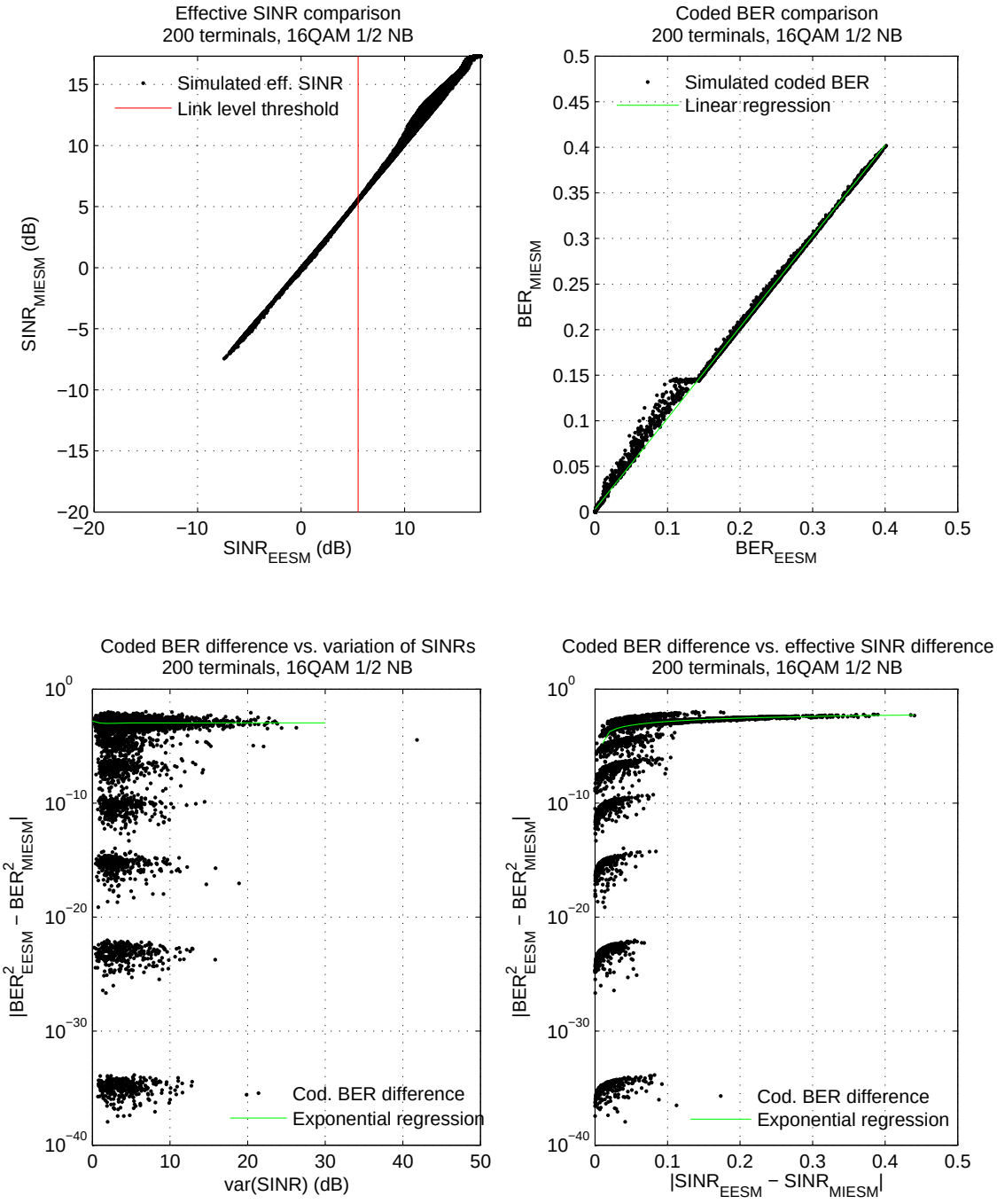

Figure C.7: Comparison of collected effective SINR and coded BER values obtained using the EESM and the MI–ESM approaches in 4G system level simulations for $16\text{QAM}\frac{1}{2}$.

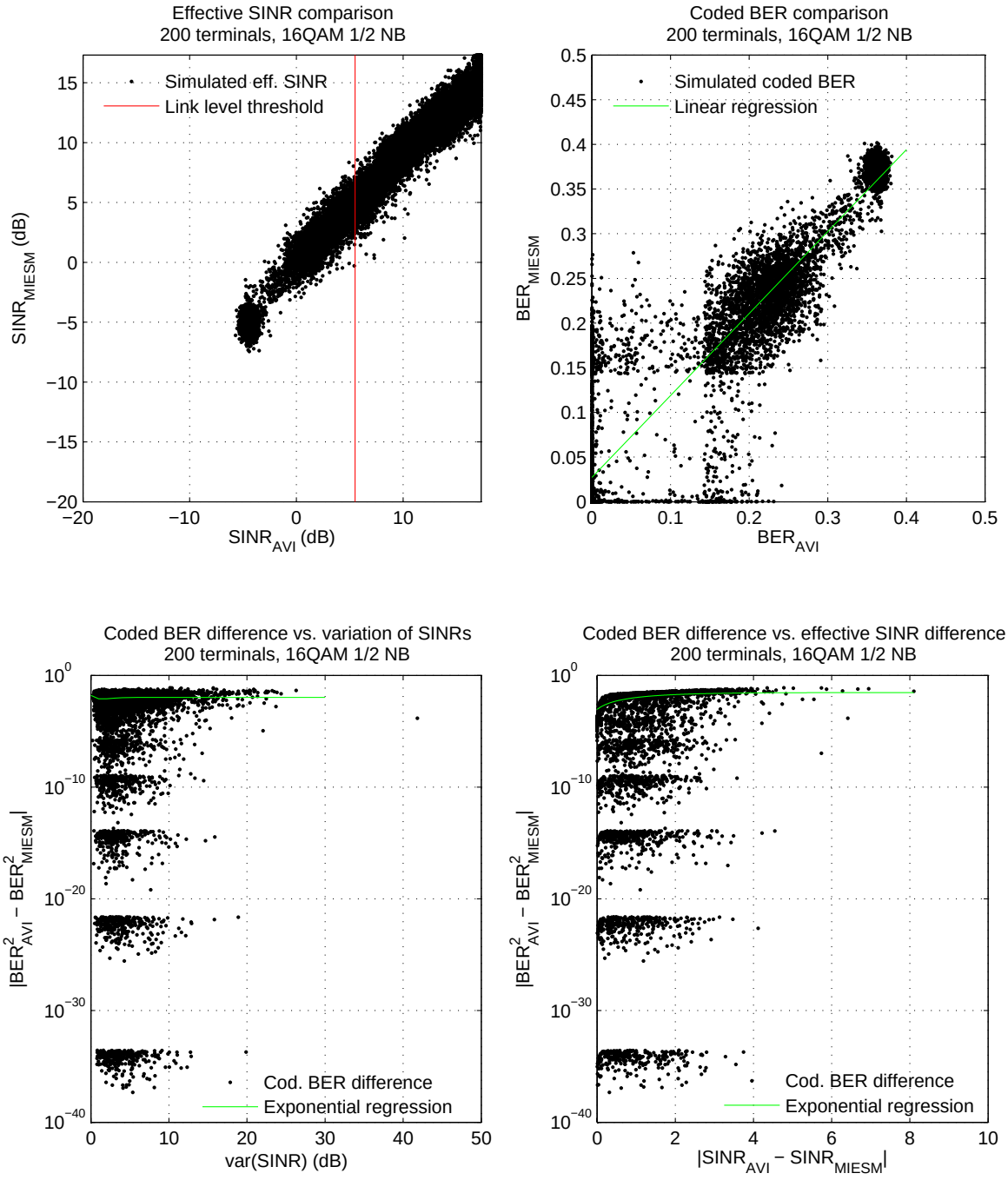

Figure C.8: Comparison of collected effective SINR and coded BER values obtained using the AVI and the MI–ESM approaches in 4G system level simulations for 16QAM$\frac{1}{2}$.

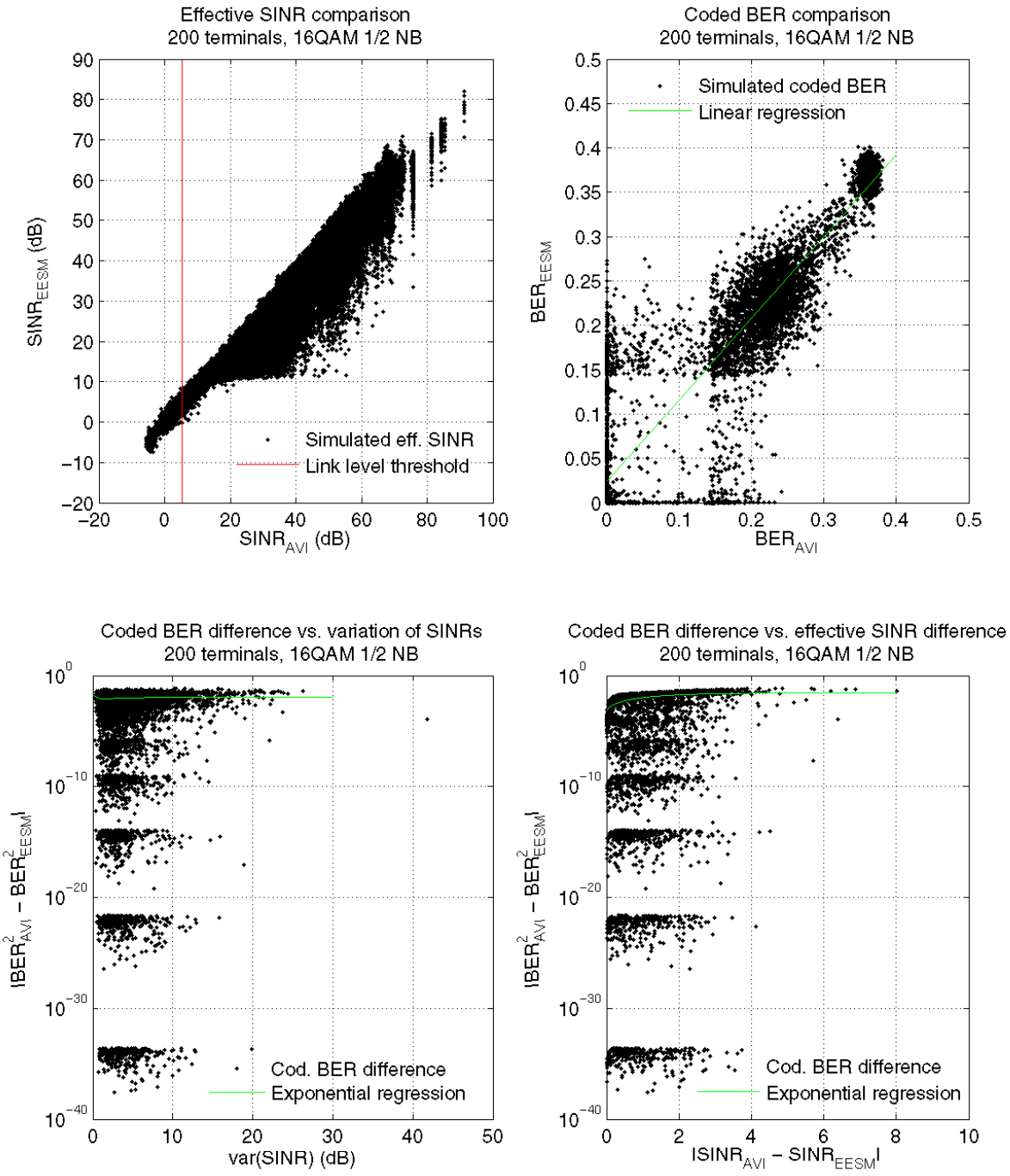

Figure C.9: Comparison of collected effective SINR and coded BER values obtained using the AVI and the EESM approaches in 4G system level simulations for 16QAM$\frac{1}{2}$.

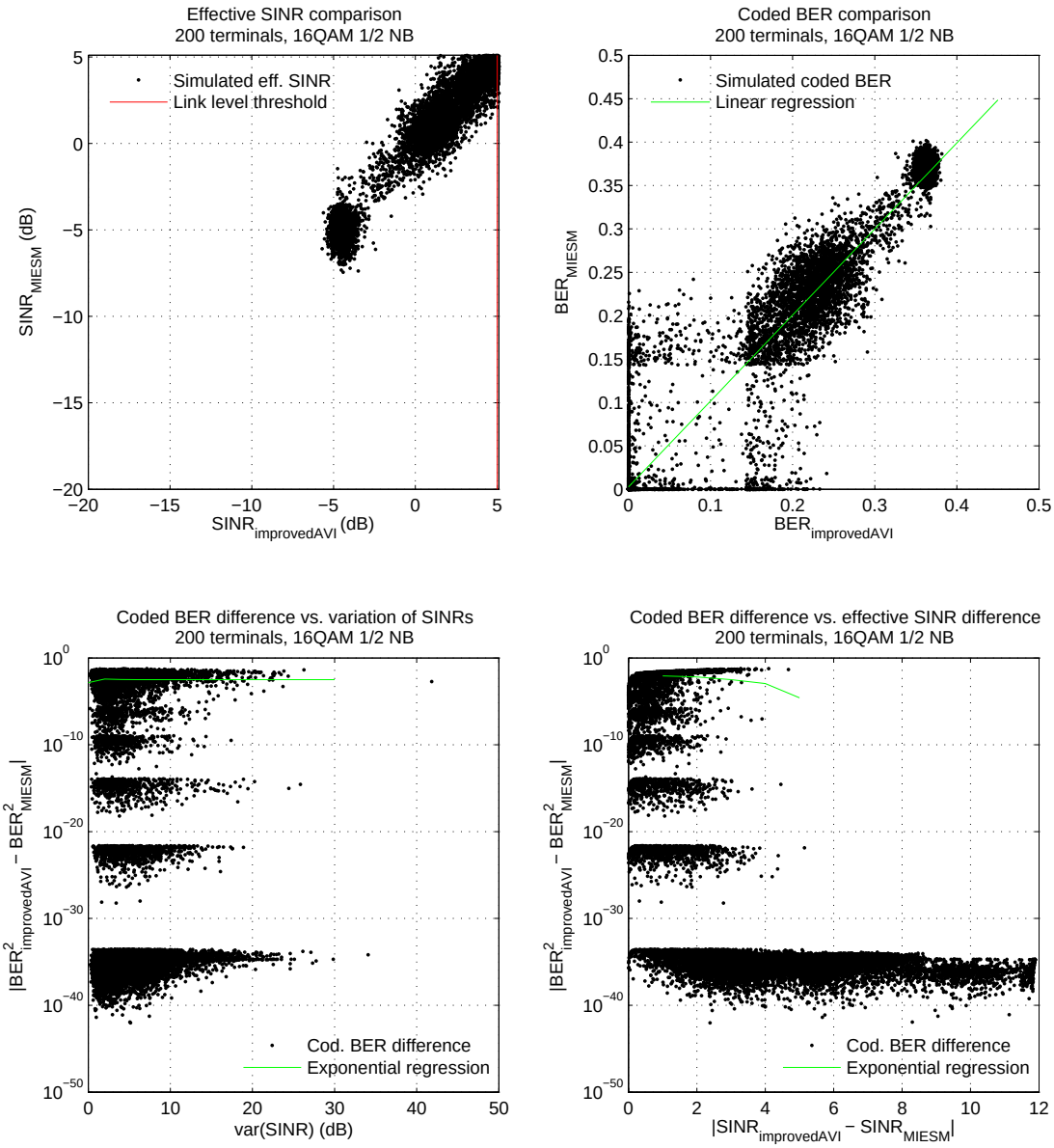

Figure C.10: Comparison of collected effective SINR and coded BER values obtained using the improved AVI and the MI–ESM approaches in 4G system level simulations for 16QAM$\frac{1}{2}$.

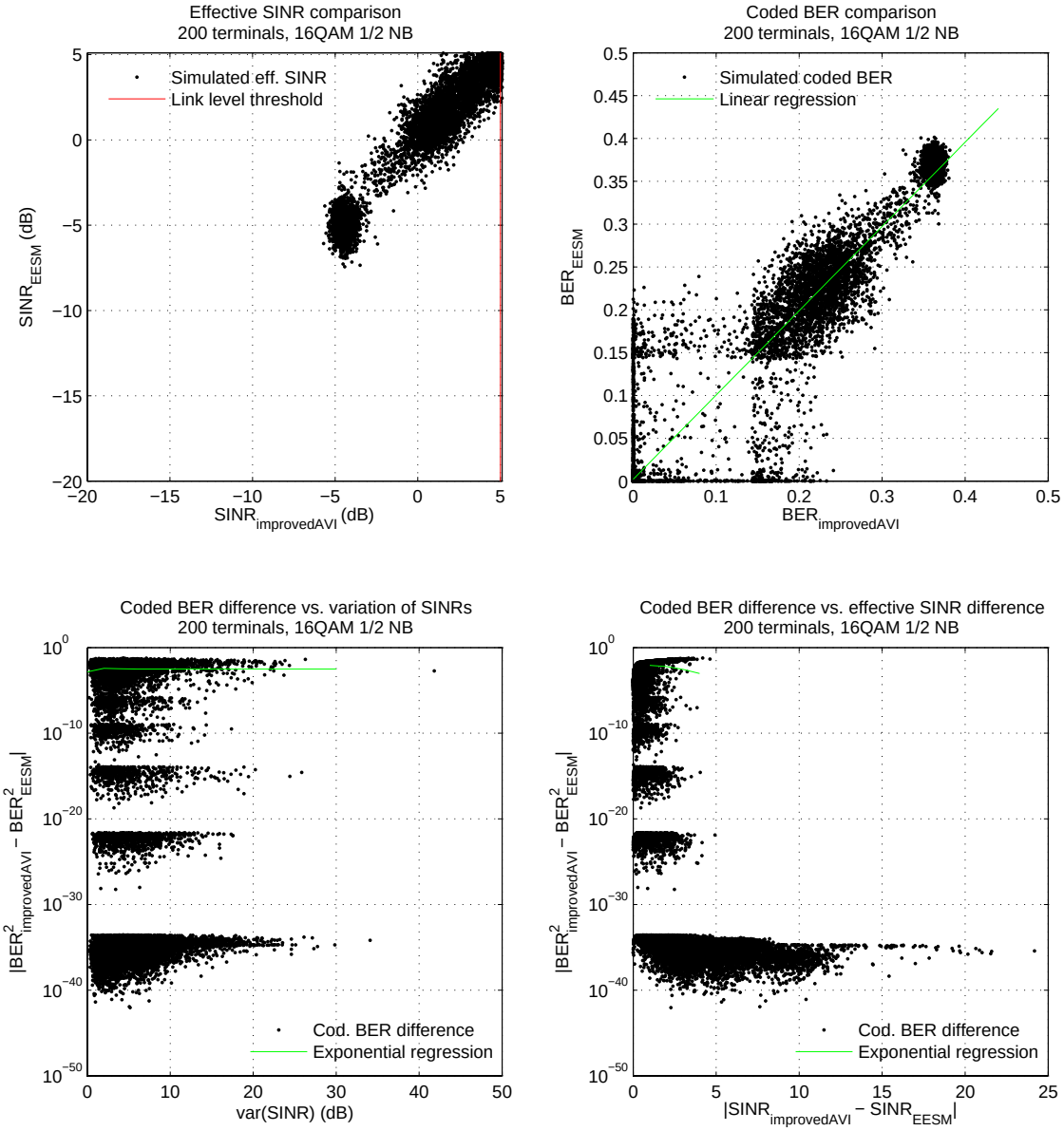

Figure C.11: Comparison of collected effective SINR and coded BER values obtained using the improved AVI and the EESM approaches in 4G system level simulations for 16QAM$\frac{1}{2}$.

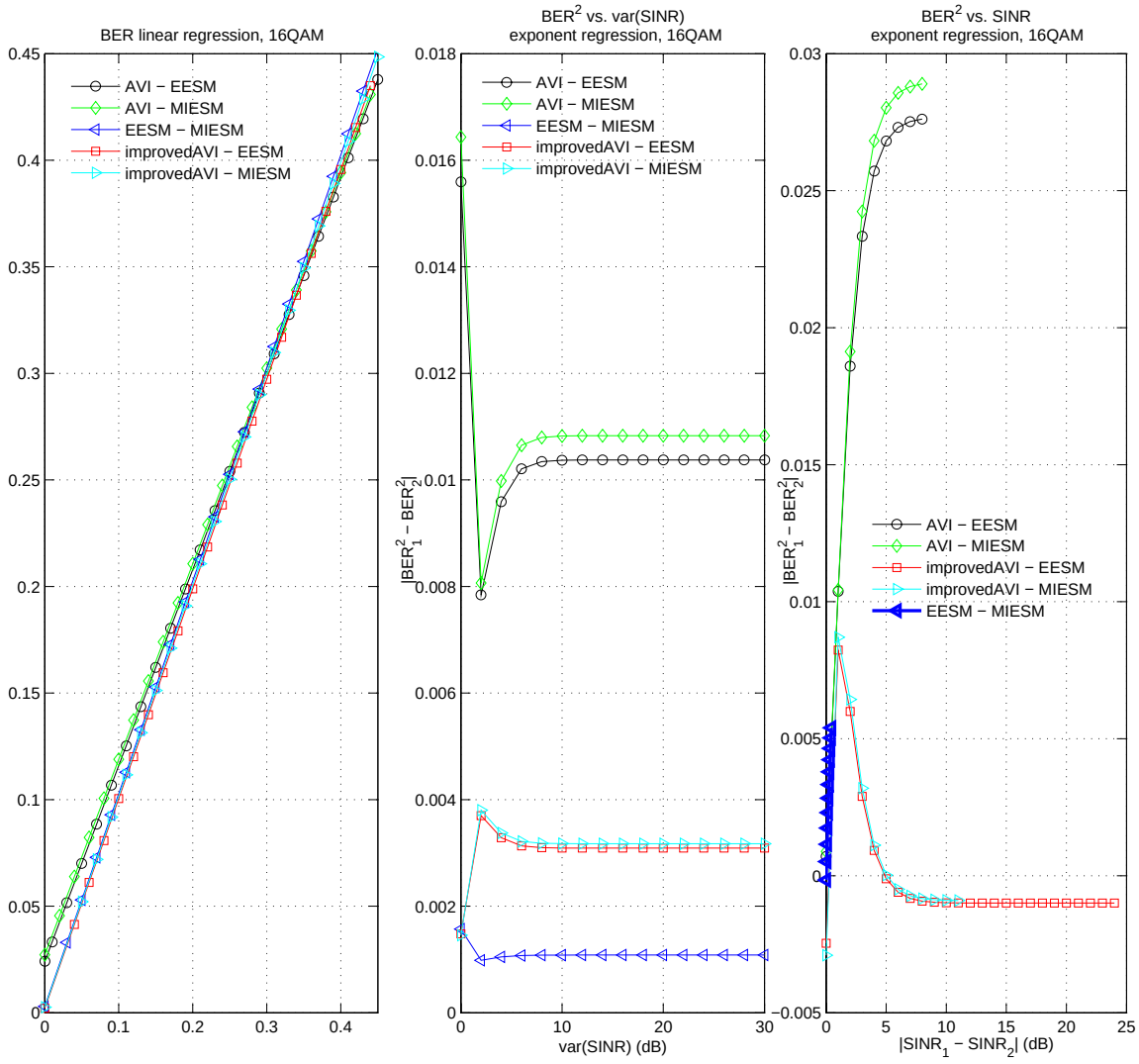

Figure C.12: Linear and exponential regressions based on collected effective SINR and coded BER values obtained using the AVI, the improved AVI, the EESM and the MI–ESM approaches in 4G system level simulations for 16QAM$\frac{1}{2}$.

Appendix D

Simulation Results

In the following Figures results obtained with 4G system level simulator are presented. 4G SLS set with parameters given in chapters 7.1 and 8.3. The simulation running time was chosen as 10 millions time steps.

In the Figures probability density function (PDF) and cumulative density function (CDF) of effective SINR values, failed and received packets, user throughput and packet delays obtained through explored L2S interface mapping approaches are depicted.

We should emphasize that the data are collected with OFDM symbol resolution. Note, the affect of maximum SNR in the case of the MI–ESM and the improved AVI (peaks) is produced by upper bounding.

Table D.1: Statistics of quality of service measures obtained through system level simulations for various L2S interface approaches.

	QPSK$\frac{1}{2}$				
	User Throughput		Packet Delay		% of Failed Packets
	Mean Mb/s	Dev Mb/s	Mean sec	Dev sec	%
AVI	1.218	1.582	14.16	14.82	0.00726
improved AVI	1.035	1.323	14.13	14.03	0.00806
EESM	0.975	1.185	14.19	14.18	0.00971
MI–ESM	0.937	1.202	14.06	14.16	0.01022
	16QAM$\frac{1}{2}$				
	User Throughput		Packet Delay		% of Failed Packets
	Mean Mb/s	Dev Mb/s	Mean sec	Dev sec	%
AVI	4.108	4.764	13.71	26.42	2.855
improved AVI	3.316	4.545	13.77	26.74	3.775
EESM	3.21	4.224	13.77	26.96	4.243
MI–ESM	3.208	4.236	13.03	26.92	4.247

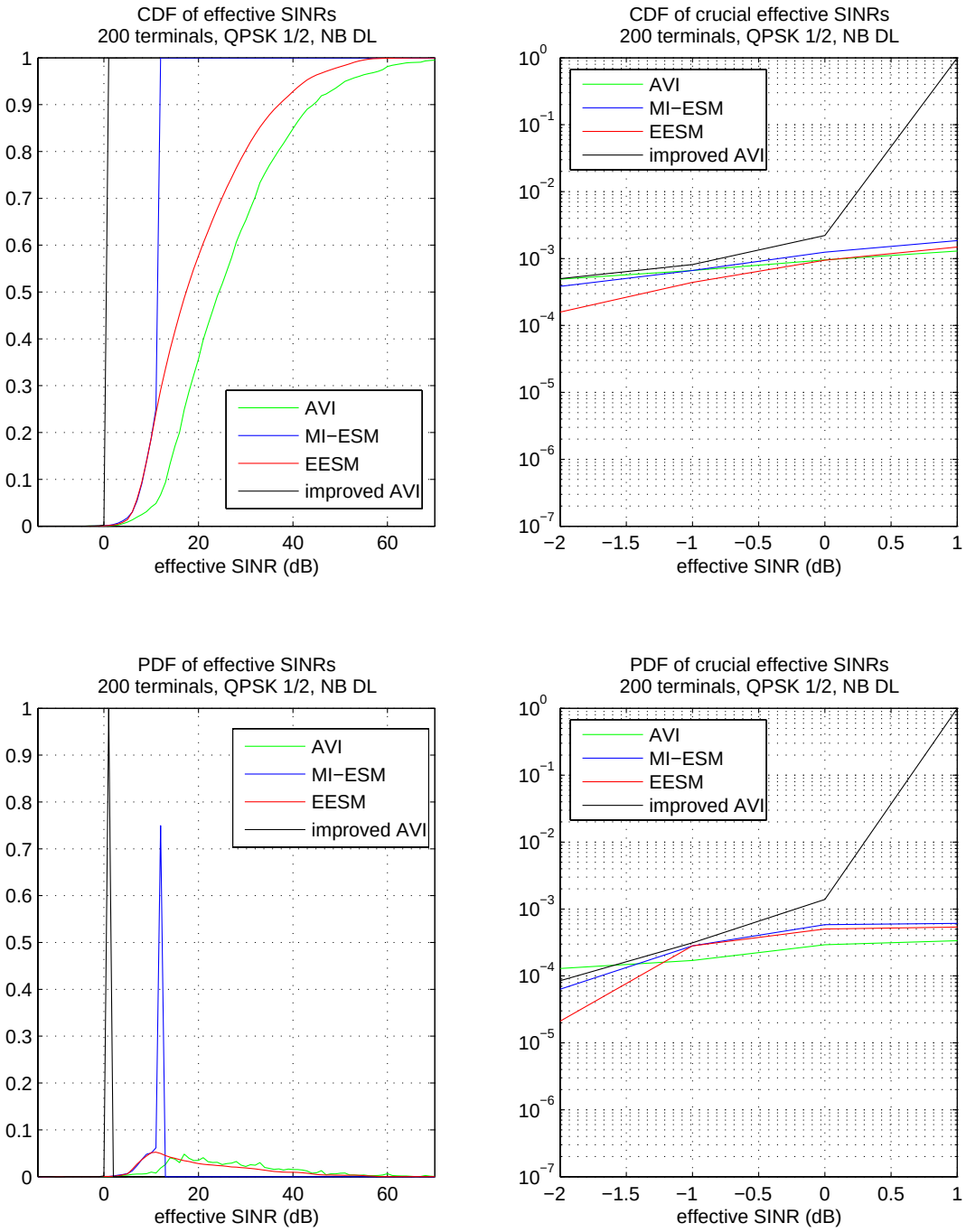

Figure D.1: PDF and CDF of effective SINR of effective SINR values obtained in 4G system level simulations for QPSK$\frac{1}{2}$.

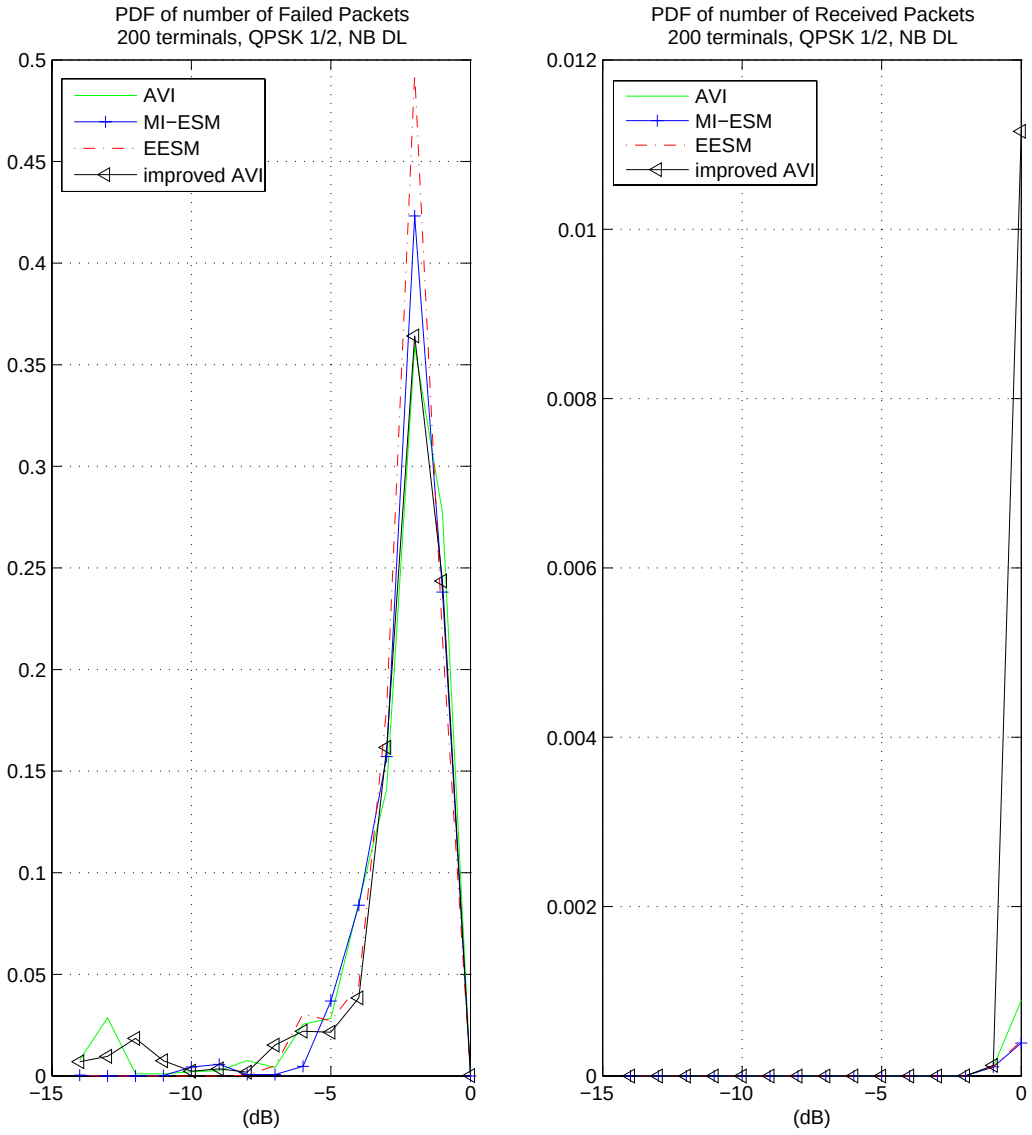

Figure D.2: PDF of number of failed and correctly received packets depending on effective SINR value. Results are obtained in 4G system level simulations for QPSK$\frac{1}{2}$.

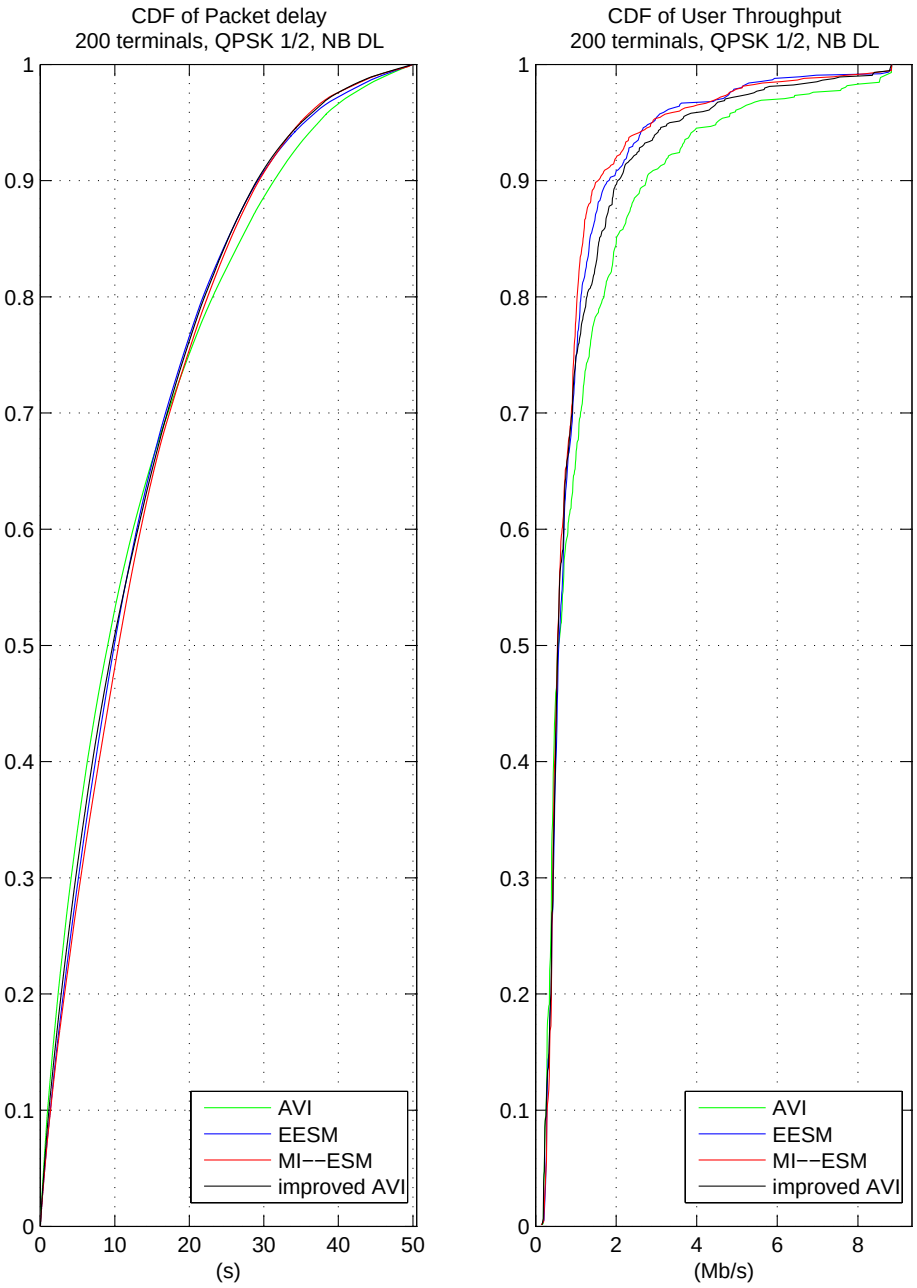

Figure D.3: CDF of user throughput and packet delay obtained in 4G system level simulations for QPSK$\frac{1}{2}$.

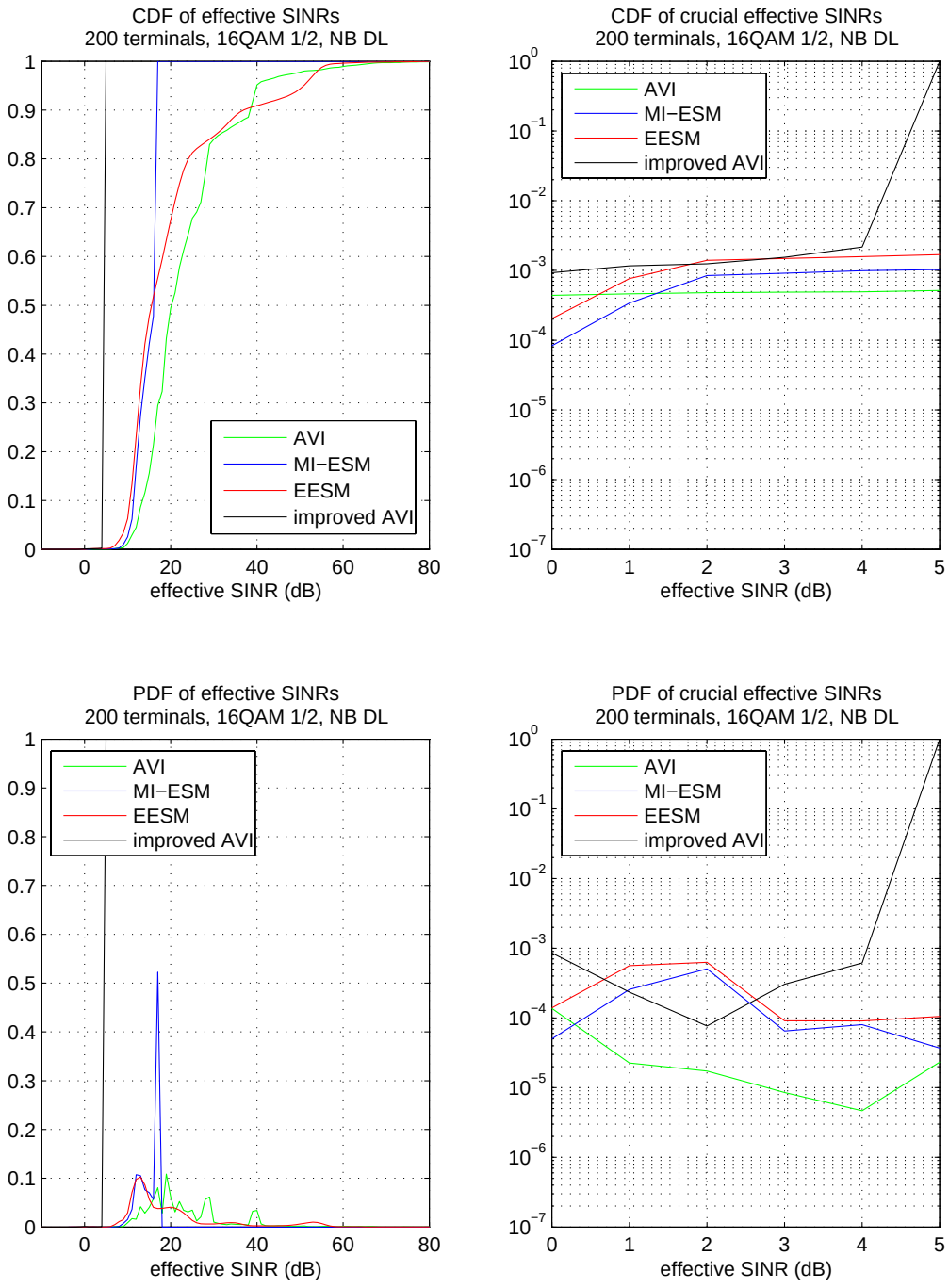

Figure D.4: PDF and CDF of effective SINR values obtained in 4G system level simulations for 16QAM$\frac{1}{2}$.

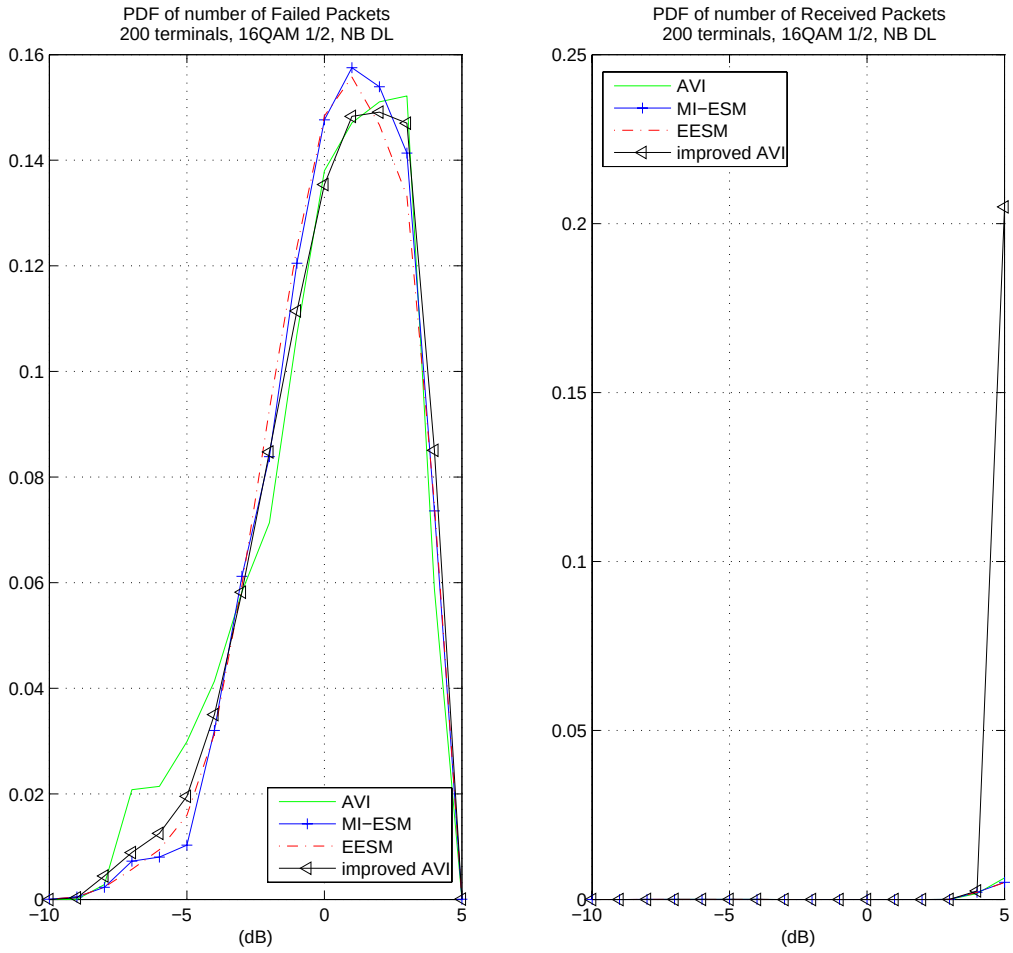

Figure D.5: PDF of number of failed and correctly received packets depending on effective SINR value. Results are obtained in 4G system level simulations for 16QAM$\frac{1}{2}$.

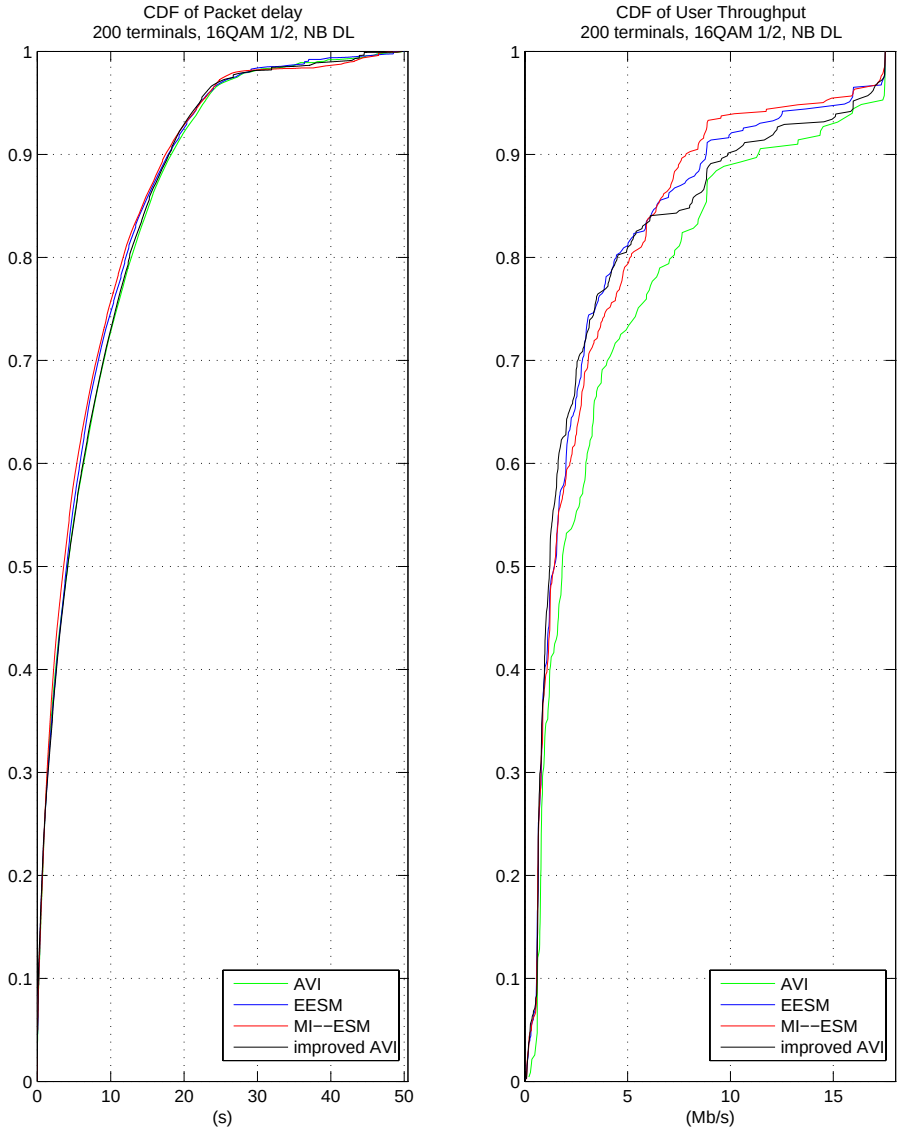

Figure D.6: CDF of user throughput and packet delay obtained in 4G system level simulations for 16QAM$\frac{1}{2}$.

Bibliography

3rd Generation Partnership Project (June, 2001). Radio access network; digital cellular communications system (phase 2+); radio transmission and reception. *3GPP TS 05.05 V8.10.0*, issue 1999.

3rd Generation Partnership Project (March, 2004). Feasibility study for OFDM for UTRAN enhancement. *3GPP TR 25.892 V1.1.0*, issue 6.0.

Alexiou, A., Astély, D., Brüninghaus, K., Coronel, P., Döttling, M., Fuchs, M., Giese, J., Haardt, M., Hennhöfer, M., Jiang, T., Jorswieck, E., Kapur, A., Li, Z., Medles, A., Mousley, T., Olsson, M., Roberts, K., Rouquette-Léveil, S., Schott, W., Sezgin, A., Skillermark, P., Stankovic, V., Svedman, P., Visuri, S., Wang, D., Wild, T., and Zimmermann, E. (February 28, 2005). Assessment of advanced beamforming and MIMO technologies. *WINNER IST–2003–507581*, D2.7, issue 1.0:1–191.

Bracewell, R. N. (1999). *The Fourier Transform and Its Applications*. McGraw-Hill Science/Engineering/Math, New York, USA.

Calhoun, G. (1988). *Digital Cellular Radio*. Artech House, Inc., Norwood, MA, USA.

Cover, T. M. and Thomas, J. A. (1991). *Elements of Information Theory*. John Wiley & Sons, Inc., New York, USA.

Debbah, M. (2002). Short introduction to OFDM. *Tutorial*.

Foschini, G. J. (1996). Layered space–time architecture for wireless communications. *Bell Labs Technical Journal*, issue 1.0:41–59.

Gesbert, D., shan Shiu, D., Smith, P. J., and Naguib, A. (2003). From theory to practice: An overview of MIMO space–time coded wireless systems. *IEEE Journal on Selected Areas in Communications*, 21, issue 3.0:281–302.

Gudmundson, M. (1991). Correlation model for shadow fading in mobile radio systems. *Electronics Letters*, 27, issue 23.0:2145–2146.

Medro, J. (January 29, 1998). Radio wave propagation characteristics at 5 GHz with modeling suggestions for HIPERLAN/2. *ETSI EP BRAN document 3ERI074A*.

Paulraj, A. J., Gore, D. A., Nabar, R. U., and Bolskei, H. (2004). An overview of MIMO communications — a key to gigabit wireless. *Proceedings of the IEEE*, 92, issue 2.0:198–218.

Rappaport, T. S. (2002). *Wireless Communications: Principles and Practice.* 2:nd edition, Prentice Hall, Inc., New York, USA.

Romero, J., Halonen, T., and Melero, J. (2002). *GSM, GPRS and EDGE PERFORMANCE.* John Wiley & Sons, Inc., New York, USA.

Shanmugan, K. S. and Breipohl, A. M. (1988). *Random Signals: Detection, Estimation and Data Analysis.* John Wiley & Sons, Ltd., New York, USA.

Sklar, B. (1997). Rayleigh fading channels in mobile digital communication systems, part I: Characterization. *IEEE Communications Magazine*, 90–100.

Smith, S. W. (1997). *The Scientist and Engineer's Guide to Digital Signal Processing.* California Technical Publishing, California, USA.

Stueberg, G. L. (2001). *Principles of Mobile Communications.* 2:nd edition, Kluwer Academic Publishers, Norwell, Massachusetts, USA.

Subgroup, W. P. (May 5, 1998). Criteria for comparison. *ETSI EP BRAN9 Sofia Antipolis document 30701F.*

Telatar, I. E. (1995). Capacity of multi–antenna Gaussian channels. *Bell Labs Technical Memorandum.*

Tsai, S. S. and Soong, A. C. (April 29, 2003). Effective–SNR mapping for modeling frame error rates in multiple–state channels. *3rd Generation Partnership Project 2 3GPP2-C30-20030429-010.*

International Telecommunication Union-Radio (June, 2003). Framework and overall objectives of the future development of IMT–2000 and systems beyond IMT–2000. *Recommendation ITU-R M.1645.*

Zheng, Y. L. and Xiao, C. (2002). Improved models for generation of multiple uncorrelated Rayleigh fading waveforms. *IEEE Communications Letters*, issue 6.0:256–258.

Ziemer, R. E. and Tranter, W. H. (2002). *Principles of Communications: Systems, Modulation and Noise.* 5:th edition, Prentice Hall, Inc., New York, USA.